MODAL ANALYSIS OF THE HUMAN BRAIN USING DYNAMIC MODE DECOMPOSITION

A Thesis
Submitted to the Graduate Faculty
of the
North Dakota State University
of Agriculture and Applied Science

By

Jayse Clifton McLean

In Partial Fulfillment of the Requirements
for the Degree of
MASTER OF SCIENCE

Major Department:
Mechanical Engineering

April 2020

Fargo, North Dakota

North Dakota State University

Graduate School

Title

Modal Analysis of the Human Brain Using Dynamic Mode Decomposition

By

Jayse McLean

The Supervisory Committee certifies that this ***disquisition*** complies with North Dakota State University's regulations and meets the accepted standards for the degree of

MASTER OF SCIENCE

SUPERVISORY COMMITTEE:

Dr. Ghodrat Karami

Chair

Dr. Alan Kallmeyer

Dr. Mariusz Ziejewski

Dr. Wenjie Xia

Approved:

04/24/2020 — Date

Dr. Alan Kallmeyer — Department Chair

ABSTRACT

The human brain is the most important organ of the human body. It controls our thoughts, movements and emotions. For that reason, protecting the brain from harm is of the utmost importance but to protect the brain, one must first understand brain injuries. Currently, observations and criteria involving brain injury are focused around acceleration and forces. However, the brain is poorly understood in the frequency domain. This study uses finite element analysis to simulate impact for 5 different impact angles. Then a numerical technique called dynamic mode decomposition is used to extract modal properties for brain tissue in regions near the corpus callosum and brain stem. Three modal frequencies were identified with frequency ranges of (44-68) Hz, (68-155) Hz, and (114-299) Hz. Additionally, it was observed that impact angle, displacement direction, and region of the brain have a significant impact on the modal response of brain tissue during impact.

ACKNOWLEDGEMENTS

I would like to first thank my advisor, Dr. Ghodrat Karami, for all his help, suggestions, and advice throughout the course of my research and writing. Also, I would like to thank my fellow graduate students, specifically Ashkan Eslaminejad, who provided me with constant advice and help as well.

I would also like to recognize my committee members, Dr. Alan Kallmeyer, Dr. Mariusz Ziejewski, and Dr. Wenjie Xia for their time and effort participating in this thesis committee. In addition, I would like to thank all the faculty in the Mechanical Engineering Department. They provided me with the knowledge and resources needed to complete this work.

I would also like to thank former teachers, coaches, and mentors who have helped me along the way. They established a foundation I have been able to successfully build upon and grow.

DEDICATION

I would like to dedicate this to my parents, Mike and Josy Mclean. They have provided me with unparalleled support throughout my entire life. Everything I have achieved as an athlete, student, and most importantly a person, is all because of them. They taught me the value of hard work and a good education and I have strived to exemplify those qualities as best I can. There is no way to thank them enough, so I dedicate this work and the opportunities it may provide me as a small way of showing my gratitude.

TABLE OF CONTENTS

LIST OF TABLES

LIST OF FIGURES

LIST OF ABBREVIATIONS

TBI	Traumatic Brain Injury
MTBI	Mild Traumatic Brain Injury
MRI	Magnetic Resonance Imaging
FEA	Finite Element Analysis
DMD	Dynamic Mode Decomposition
CSF	Cerebrospinal Fluid
DAI	Diffuse Axonal Injury
GCS	Glasgow Coma Scale
AIS	Abbreviated Injury Scale
HIC	Head Injury Criterion
COM	Center of Mass
BTBI	Blast Traumatic Brain Injury
ICP	Intracranial Pressure
NHTSA	National Highway Traffic Safety Administration
NFL	National Football League
STF	Shear Thickening Fluid
CTE	Chronic Traumatic Encephalopathy
NFT	Neurofibrillary Tangles
CTEM	Chronic Traumatic Encephalomyelopathy
ALS	Amyotrophic Lateral Sclerosis
POD	Proper orthogonal Decomposition
BOD	Bi-orthogonal Decomposition

SVD.....Singular Value Decomposition

CT .....Computed Tomography

NIH .....National Institute of Health

DOF.....Degree of Freedom

LIST OF APPENDIX TABLES

LIST OF APPENDIX FIGURES

CHAPTER 1. INTRODUCTION

1.1. Motivation

The brain is perhaps the most complex and important organ in the human body. It controls our thoughts, memory, feelings, movements, and controls how we experience and perceive the world around us. It can analyze and retain incredible amounts of information and is capable of expressing a multitude of emotions. It is responsible for incredible feats of engineering, masterpieces of art, and creative ideas and innovations that shape and change our environment every day. The human brain is immensely powerful and complex; however, it is very fragile and suscepetible to injury. Traumatic brain injuries (TBI) are an alteration to brain function due to an external force. Not all TBIs are the same; their severity depends on the level of trauma and the injury mechanism associated with them. Severe TBI can lead to death but less severe forms of TBI can be just as dangerous. This paper focuses on the more common and frequent, mild traumatic brain injury (MTBI). MTBIs, more commonly known as concussions, are an epidemic in American sports, especially football. The short-term effects of concussions are dangerous but with the recent advancement of diagnostic methods and technology, clinicians have discovered that the repetitive and long-term effects can prove to be even more detrimental. Consequently, striving to understand the brain's injury mechanisms and how to protect the brain has become a primary concern for the science and engineering fields.

The human head is often referred to as a "black box." In other words, what goes on inside the human skull during impact is difficult to observe or quantitatively measure without compromising *in vivo* conditions. Cadavers are often used to simulate impact to the human brain, but they do not truly represent *in vivo* conditions because of dehydration and lack of blood flow changes the mechanical properties and behavior of components inside the skull. Technology

such as magnetic resonance imaging (MRI) can also be used to see inside the skull but is limited in application because of the device's large size and lack of mobility. Instead, the primary and most effective way to examine impact to the human head is to use finite element analysis (FEA). FEA discretizes the brain and other components into tiny elements. By assigning proper material properties and boundary conditions to these elements, FEA can determine displacement, forces, stresses, strains, etc. This technology makes it possible to study the brain as a dynamic system in ways that are impossible with experimental methods. When the human brain experiences impact, waves of vibration are sent throughout the brain. These waves propagate and attenuate at different rates within the brain depending on the magnitude and direction of loading. When the human brain is subjected to vibration, like any dynamic system, it exhibits natural frequencies and natural modes of vibration. At natural frequencies, input vibration amplitudes are amplified within the brain causing an increase in displacement and strain; this is called resonance. This increase in strain causes excessive stretching of brain tissue and can lead to MTBI. By conducting modal analysis and identifying these resonant frequencies, safety measures could be implemented to reduce or possibly even eliminate vibrations in these frequency ranges. Thus, reducing strain experienced in the brain and lowering the chance of MTBI.

1.2. Problem Statement

The human brain is still poorly understood in the frequency domain. In an impact event, the primary concern for nearly any injury criteria is acceleration. Yet, impact events are highly transient dynamic events that generate extensive vibration. The variation of these vibrational frequencies could potentially have a varying effect on the strain experienced by the brain depending on natural frequencies. The challenge is that direct methods of modal analysis require a material with linear material properties, but the human brain is nonlinear. In addition, as

discussed earlier, it is difficult to gather experimental data that truly represents *in vivo* conditions for impact. For these reasons, a method heavily reliant on numerical simulation and numerical analysis must be used.

1.3. Aims and Objectives of this Study

This research seeks to use FEA in combination with numerical techniques to conduct modal analysis on the human brain to identify the brain's resonant frequencies. Using the finite element software LS-DYNA, brain nodal displacement will be collected from a human head model and subjected to Dynamic Mode Decomposition (DMD) using a code created in MATLAB. DMD can extract the dynamic characteristics of a system without having to define the underlying system itself which lends it to be very useful for both numerical and experimental data. Resonant frequencies will be examined for various impact directions and compared regionally throughout the brain. This study aims to identify a frequency range in which the brain is more susceptible to vibration with the end goal of better understanding the brain in the frequency domain and preventing future TBIs.

The remainder of this thesis is divided into four separate chapters. Chapter 2 contains literature reviews focusing on the biomechanics of the human skull, traumatic brain injury, modeling the human brain, and modal analysis techniques. Chapter 3 details the setup of the numerical model within LS-DYNA and the application of DMD. Chapter 4 presents the results generated from the numerical model and discusses the corresponding data analysis. Chapter 5 focuses on conclusions that can be drawn from the data and results and suggests ways to improve upon this current work and makes recommendations for future work.

CHAPTER 2. RESEARCH BACKGROUND

2.1. Anatomy of the Human Head

2.1.1. Components of the Human Skull

The human skull is the primary mechanism of protection for components of the human head. Its outer surface is completely covered by the scalp which consists of layers of dermal skin and soft subcutaneous connective tissue. The skull itself is comprised of 22 bones that are separated into two different categories; the facial and cranial bones. There are 14 facial bones that make up our facial features and provide structure for openings meant for air and food, but they do little to provide protection for the brain and other components inside the skull. Instead, protection is provided by the 8 cranial bones. Shown in Figure 2-1, the 8 cranial bones are the two temporal, two parietal, occipital, frontal, sphenoid, and ethmoid bones. The separate bones are joined together by rigid sutures. The sutures are immobile and rigid and for that reason in most analyses, the human skull is considered as one single structure instead of 8 separate bones.

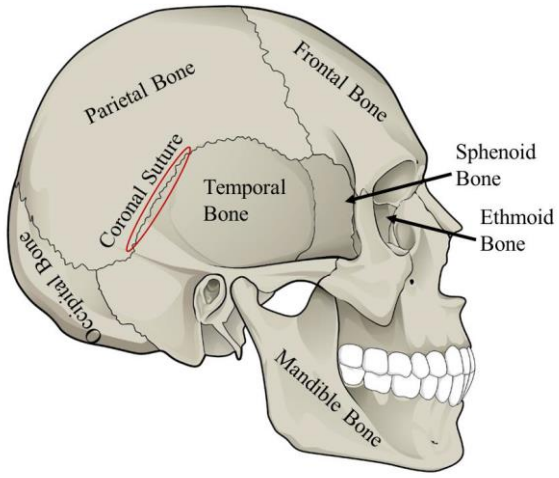

Figure 2-1: Schematic depicting the mandible and 8 cranial bones [1].

Within its confines, the skull contains the brain, protective meninges, and cerebrospinal fluid (CSF). Over 200 years ago, Alexander Monro applied principles of physics, and hypothesized that the sum of the volumes of brain tissue, CSF, and intracranial blood must

remain constant. Later, experiments performed by George Kellie supported this hypothesis and determined that a healthy human cranium consists of 80% brain tissue, 10% CSF, and 10% intracranial blood. This became known as the Monro-Kellie doctrine [2].

2.1.2. Meninges

The skull is separated from the brain by several layers of membranous tissue called meninges. These meninges provide protection and encase the brain. In 2012, Gu et al. [3] used FEA to show that in blast loading, the presence of meninges reduced maximum shear stress experienced in the brain by nearly 50%. The meninges are divided into three main layers known as the pia, arachnoid, and dura mater. Figure 2-2 shows how these layers are ordered. The pia mater is a very thin layer that separates the brain from the arachnoid and dura mater. The space between them, known as the subarachnoid space, is filled with CSF which cushions and nourishes brain tissues [4]. Additionally, a deep fold of the dura mater, called the falx cerebri membrane, separates the two hemispheres of the brain and aids in preventing rotation of the brain inside the skull.

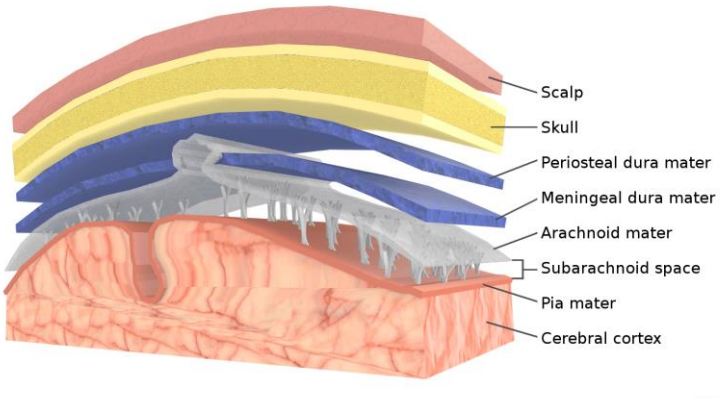

Figure 2-2: Exploded view of the different meningeal layers that reside between the brain and skull [5].

2.1.3. The Human Brain

The average human brain is about three pounds and is divided into three main components: the cerebrum, cerebellum, and brain stem. These components are shown in Figure 2-3. The cerebellum resides underneath the cerebrum and serves to control muscle movements and maintain posture and balance. The brain stem's main function is to relay information from the cerebrum and cerebellum to the spinal cord and subsequently to the rest of the body. It also controls and regulates many autonomous functions of the body such as breathing, body temperature, heart rate, and sleeping patterns. The cerebrum is the largest part of the brain and is responsible for many higher order functions such as our senses, reasoning, and fine control of movement [6].

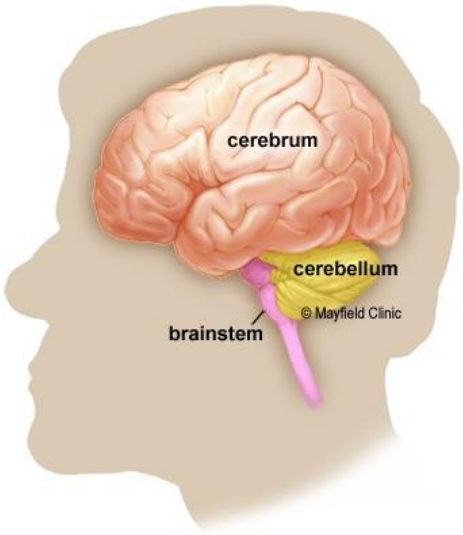

Figure 2-3: Schematic of the three principle components of the human brain: cerebrum, cerebellum, brain stem [6].

The cerebrum is divided into two hemispheres that are connected by a bundle of fibers known as the corpus callosum. The corpus callosum serves as the bridge that connects the two hemispheres and allows them to communicate with one another. The corpus callosum also serves an important role in the propagation of vibrations through the brain. The membrane-like behavior of the corpus callosum acts as a barrier to the propagation of vibrations and because of this,

vibrations are obstructed and tend to concentrate near the corpus callosum and cause increased strain in this area [7].

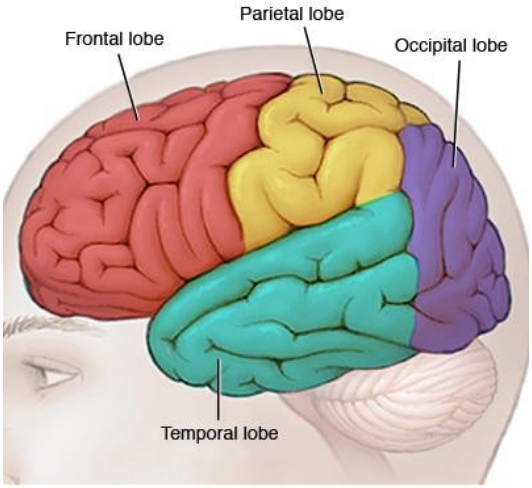

Figure 2-4: Depiction of the four lobes that subdivide each hemisphere of the cerebrum [8].

Furthermore, each of the two hemispheres of the cerebrum are divided into four lobes. The frontal, parietal, occipital, and temporal lobes are shown in Figure 2-4. The frontal lobes are the largest of the lobes and are responsible for important cognitive functions such as our behavior, problem solving, and emotions but it also controls voluntary body movement [9,10]. Next, the parietal lobes are responsible for human's spatial awareness and navigation. They are also responsible for the sense of touch, pain, temperature, and spatial and visual awareness [11]. Another important function of the parietal lobe is that it provides a memory system for episodic memory, or conscious memories for everyday events [12]. The occipital lobes, which reside in the rear of the skull, are the smallest of the four pairs of lobes. The occipital lobes contain a majority of the visual cortex and are primarily responsible for interpreting vision and the corresponding colors and lighting. The temporal lobes are adjacent to the parietal lobes and are tasked with interpretation and storage of the sensory information gathered by the parietal lobes. The temporal lobes contain the hippocampi, which play a critical role in memory and if damaged

can lead to memory loss and amnesia. The hippocampus is particularly responsible for spatial memory; helping humans remember directions to navigate their surroundings. The temporal lobes are also primarily responsible for language comprehension.

2.1.4. Cerebrospinal Fluid

Cerebrospinal fluid (CSF) is a clear and colorless liquid that can be found in the skull and spinal cord. Each day around 500 mL of CSF is produced by the chloroid plexuses found within the ventricles of the brain [13]. However, this CSF is constantly being reabsorbed so only about 125-150 mL of CSF is present at any one time [14]. After production, CSF migrates through the ventricular system and reaches the exterior of the brain where it then occupies the subarachnoid space between the arachnoid and pia mater. The pia mater is directly attached to the brain while the arachnoid and dura maters are directly attached to the skull. Consequently, the CSF occupying the space between them creates a liquid boundary layer that separates the two structures. This allows for relative motion between the brain and skull and introduces linear and rotational inertial loading as an injury mechanism. CSF also provides several other functions within the skull. First, CSF is slightly denser than the brain so it provides natural buoyancy for the brain to prevent it from loading due to its own weight which could potentially cut off the circulation of blood. With this buoyancy, the brain's weight is reduced from its true weight of about three pounds to a net weight of only 1-2 ounces [14,15]. Also, as discussed earlier, the CSF within the subarachnoid space transports nutrients to the brain and transports waste from the brain to the bloodstream. Finally, although CSF introduces additional inertial loading to the brain, it does provide a hydromechanical protective buffer that cushions the brain under impact.

2.2. Injury to the Brain

2.2.1. Traumatic Brain Injury

Each year in the United States, traumatic brain injury (TBI) accounts for 50,000 deaths [16]. Nonfatal TBI is responsible for another 230,000 hospitalizations, with 80,000 of those cases resulting in a permanent disability [16,17]. As stated in the introduction, TBI is an alteration of brain function due to an external force. Forces could be impact, blast, inertial loading due to rapid acceleration or deceleration, or penetration. Alterations are typically divided into three categories: physical, cognitive, and behavioral. Physical alterations are typically the most noticed because the symptoms are often very visual or painful. Examples include loss of balance or coordination, fatigue, headaches, and impaired speech. Cognitive alterations primarily affect the human brain's ability to process and retain information. Symptoms include memory loss, impaired judgement and problem-solving skills, and a shortened attention span or lack of concentration. Behavioral alterations, often referred to as emotional alterations, commonly go unnoticed which can make them particularly dangerous. What a person is thinking or feeling on the inside is not always portrayed to the people around them. Humans have the innate ability to mask their emotions and hide what they are truly thinking or feeling, especially if those thoughts are unfavorable or negative. TBI can lead to depression, anxiety, anger, impulsivity, and just general emotional instability. In some cases, undiagnosed behavioral alterations can lead to impulsive decisions by a person that results in them severely hurting themselves or the people around them. It is important to note that the duration or effect of any TBI symptom varies from case to case. For this reason, criteria have been developed to help determine and differentiate the severity of TBIs.

There are different injuries responsible for TBI and they are typically dependent on the type and severity of loading. Brain injuries are typically divided into focal injuries, or injuries that occur in a specific location, and diffuse injuries, which are spread throughout the brain. An example of a focal injury is a contusion, often referred to as a bruise. Usually a result of impact, a contusion is a form of mild bleeding caused by the brain contacting the inside of the skull. In some cases, if the force is high enough, this contact can lead to another form of focal injury called a brain laceration, which is a tear in the meningeal layers of the brain. This level of force is difficult to achieve so lacerations are more common in penetration injuries and skull fracture. Another form of focal injury is a hemorrhage, or excessive bleeding. Hemorrhages can occur at different locations within the skull and are named accordingly as epidural, subdural, intracerebral, and intraventricular depending on their location [18]. Epidural hemorrhages occur between the dura mater and skull, subdural hemorrhages are between the dura mater and brain, while intracerebral and intraventricular hemorrhages occur within the brain and ventricles, respectively. Additionally, focal injuries can be divided into coup and contrecoup. Depicted in Figure 2-5, coup indicates the injury occurred on the same side as the impact while contrecoup indicates the injury occurred on the opposite side of the brain. In severe cases, due to the oscillatory motion of the brain, injury can occur on both sides of the brain during a single impact. Initially, the brain contacts the impact side of the skull (coup), but then due to the elastic impact, the brain is reflected in the opposite direction and contacts the opposite side of the skull (contrecoup). This is known as coup-contrecoup injury. In 2004, Drew et al. [19] showed that because CSF is denser than the brain, in cases of rapid deceleration the CSF is driven forward, pushing the brain back in the contrecoup direction. In this case, the brain contacts the contrecoup side of the skull first and then contacts the coup side of the skull second. This is known as a

contrecoup-coup injury. This injury mechanism helps explain the counterintuitive phenomenon where in certain impacts contrecoup brain injuries are more severe compared to the corresponding coup brain injury.

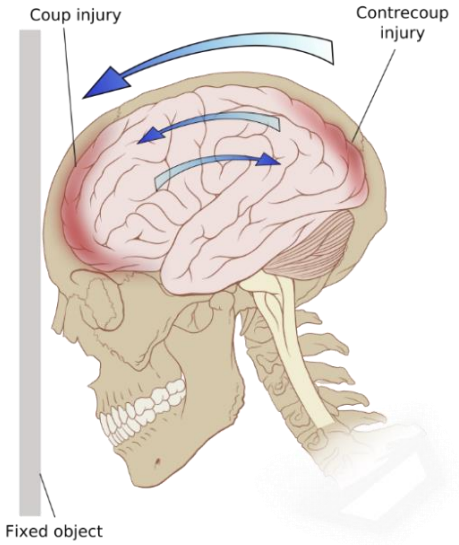

Figure 2-5: Schematic depicting the locations of coup and contrecoup injuries. These can also occur during the same impact event and are known as coup-contrecoup and contrecoup-coup [20].

Although related to focal injuries, coup-contrecoup injuries are responsible for diffuse injuries as well; most notably, diffuse axonal injury (DAI). The oscillatory nature of coup-contrecoup injuries leads to substantial shear waves and as these shear waves propagate through the brain, they create localized strains that cause excessive stretching and shearing of axons within the brain. This axonal damage leads to the impairment of axonal transport and eventual axonal swelling [21,22]. DAI is believed to be the primary cause of concussions and MTBI [23, 24].

2.2.2. Severity of Traumatic Brain Injury

TBIs are divided into three main categories: severe, moderate, and mild. It is important to note that, although they are categorized into three different categories, all TBIs are dangerous

and can lead to serious and life altering problems. The severity of a TBI is established by determining the amount of disruption to the brain's physiology or structure. The boundaries between these categories can be hard to distinguish and for that reason moderate to severe TBI are often grouped together. To help determine the severity of a TBI, researchers have developed different criteria to evaluate TBI. One of the most popular criteria is the Glasgow Coma Scale (GCS), which evaluates eye, verbal, and motor responses to calculate the severity of a TBI. The GCS scoring is summarized in Table 2-1 below.

Table 2-1: Glasgow Coma Scale

Behavior	Response	Score
Eye Opening Response	Spontaneously	4
	To speech	3
	To pain	2
	No response	1
Best Verbal Response	Oriented to time, place, and person	5
	Confused	4
	Inappropriate words	3
	Incomprehensible sounds	2
	No response	1
Best Motor Response	Obeys commands	6
	Moves to localized pain	5
	Flexion withdrawal from pain	4
	Abnormal flexion (decorticate)	3
	Abnormal extension (decerebrate)	2
	No response	1

Another popular injury metric is the Abbreviated Injury Scale (AIS). AIS uses a 7-digit number to identify the location, type, and severity of the injury. The first digit of the number identifies the location of the injury. For example, head injury is identified by a first digit of 1.

The next two numbers identify the type of anatomical structure affected, such as skeletal structures, organs, or the nervous system. The third and fourth numbers further specify the exact anatomical structure affected but in the case of head injury it indicates the level of consciousness. The fifth and sixth numbers are used for specific injuries such as lacerations or fractures. The final number represents the severity of the injury ranging from 1 being a minor injury, to 6 being lethal. The final number does not give details of the severity of the injury but rather is a representation of the threat to life, as shown in Table 2-2 [25].

Table 2-2: AIS severity codes

AIS-Code	Injury	% Probability of Death
1	Minor	0
2	Moderate	1-2
3	Serious	8-10
4	Severe	5-50
5	Critical	5-50
6	Maximum	100

The two methods described above are qualitative methods based on injuries observed after a person experiences a head injury. These methods are useful for first responders and clinicians when trying to understand the extent of a brain injury but are not very useful for experimental or numerical data. Test dummies and numerical models do not provide qualitative measures to be used in conjunction with GCS or AIS, but they do provide extensive quantitative values such as force, velocity, and acceleration. For this reason, the Head Injury Criterion (HIC) was developed to provide a quantitative measure for head injuries. The HIC uses the acceleration of the center of mass (COM) of the head to determine the likelihood of injury after impact to the head. For crash test dummies, accelerometers can be placed internally to measure the

acceleration at the COM. In the cases of numerical models and FEA, acceleration at the COM is calculated during simulation and can be easily retrieved in post processing. The HIC is determined using,

$$HIC = max_{t_1,t_2}\{[\frac{1}{t_2 - t_1}\int_{t_1}^{t_2} a(t)dt]^{2.5}(t_2 - t_1) \quad (2.1)$$

where t_1 and t_2 are the initial and final times in seconds chosen to maximize HIC, and $a(t)$ is the acceleration in g's ($9.81\ \frac{m}{s^2}$) as a function of time. The time bounds are chosen to provide the maximum value for HIC but in 1972, Hodgson et al. [26] examined concussion level impact to the head and determined a maximum interval of 15 milliseconds for accurate results. This is commonly referred to as the HIC_{15}. Using the HIC_{15} and a Hybrid III crash test dummy, Mertz et al. [27] developed injury risk curves to predict skull fracture and brain injuries with AIS≥4. According to Mertz, a HIC_{15} of 1000 corresponds to a 16% chance of skull fracture and a 17% chance of brain injury. The HIC_{15} for MTBI is less well defined and often varies throughout literature. In a study spanning six years from 2005-2011, Beckwith et al. [28] fitted 1,208 collegiate and high school football players with instrumented football helmets to monitor acceleration and determined a mean HIC_{15} of 321.5 for concussive impacts. However, other studies conducted by entities such as the NFL have determined mean HIC_{15} values ranging from 249-557 [29-31]. This variance is partially due to sample size and age but is also a result of the varying effect different loading mechanisms and directions have on acceleration experienced in the brain. Unfortunately, HIC_{15} has a major limitation. It only considers linear acceleration and for that reason can be inaccurate for rotationally dominated loadings.

2.2.3. Mechanisms of Traumatic Brain Injury

The four primary mechanisms of TBI are penetration, blast, direct impact, and sudden or rapid acceleration and deceleration. Penetration TBI occurs when an object penetrates the skull and dura mater. Penetration injuries are the least common form of TBI, but they are the most dangerous. In a penetration injury, the skull and protective meninges are completely compromised which leaves the brain open to direct damage from foreign objects or bone fragments of the skull. It takes a tremendous amount of force to penetrate the skull so penetration TBI is typically associated with high velocity impact and sharp objects. Examples include gunshot wounds, impact from knives, or high velocity car crashes. In 1991, Vinas et al. [32] examined 314 patients who had suffered a penetrating brain injury due to a gunshot wound. They found that 73% of victims died at the scene of the injury and another 19% died later from complications due to their injuries. In total, this leads to a mortality rate of 92%. Non-gunshot penetration TBIs have lower mortality rates but are still very high. Demetriades et al. [33,34] studied 7764 patients and found a mortality rate of 42% for non-gunshot penetration injuries compared to only 9% for closed injuries [35].

Blast-related TBI (BTBI) is frequently seen in military settings where exposure to explosives is common. Soldiers today are frequently exposed to blast because of the increased use of IED's by terrorists and insurgents. For that reason, understanding BTBI is of the utmost importance to help protect soldiers abroad. When a bomb or IED detonates, the explosion sends a shockwave propagating through the air. Shown in Figure 2-6, a shockwave is a sharp change in air pressure that creates a wave front of over pressurized air followed by a pressure drop to below atmospheric pressure. Shockwaves travel faster than the speed of sound and can cover great distances, but their energy and speed dissipate relatively quickly. When the wave front

contacts a solid object, the large pressure gradient can impose a substantial force on the object and turn it into a flying projectile. The wave also sends vibrations through the solid object as the wave is transferred from one medium to another. Due to these forces and vibrations, BTBI is divided into three different categories; primary, secondary, and tertiary.

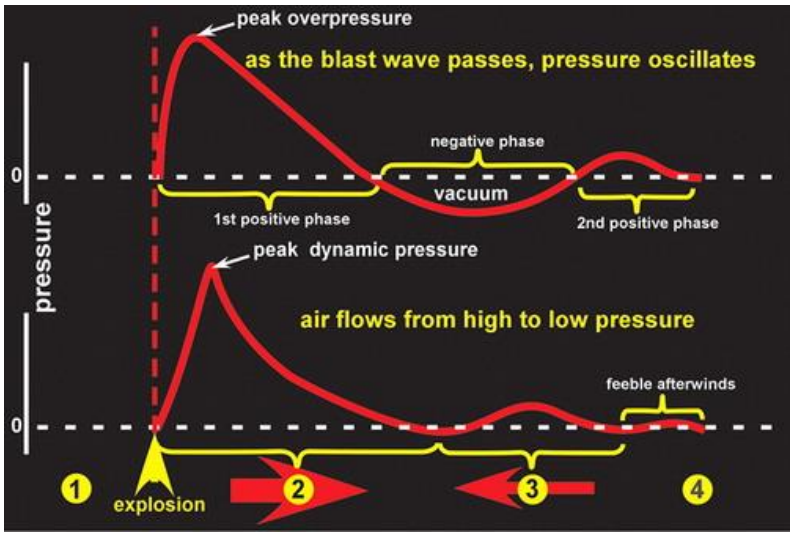

Figure 2-6: Changes in atmospheric pressure following an explosion. (1) The pressure is normal right before detonation. (2) Air pressure drastically increases immediately after detonation creating the over pressurized wave front. (3) The wave front is followed by a pressure drop to below atmospheric levels. (4) The shockwave quickly dissipates, and pressures return to normal atmospheric levels [36].

Primary BTBI is associated with injuries directly caused by the propagating wave front and the corresponding induced vibrations. Secondary BTBI is the result of surrounding objects being put in motion by the wave front and turning them into projectiles. These projectiles then contact the head and replicate ballistic impact. This could be flying debris or a structure collapsing and falling on a person. Tertiary BTBI is due the person being thrown into solid structures or onto the ground. Secondary and tertiary BTBI are very widely accepted because they are essentially forms of ballistic impact and rapid acceleration or deceleration. What differentiates them is simply that the ballistic projectiles or acceleration, were blast induced. Conversely, the biomechanics of primary BTBI and its effects are less understood. One of the

challenges with primary BTBI is trying to find cases where only primary MTBI occurs. Typically blast injuries are a combination of the various types and it can be difficult to differentiate what is responsible for the subsequent injuries. For ethical reasons, experimental data for blast injuries in humans is limited but using mouse models, McKee et al. [37] determined that the blast wind produces forces comparable to those experienced during severe concussive impacts. As the blast wind passes the head, the brain rapidly expands and contracts several times. Thus, the brain tissue and blood vessels are rapidly and excessively stretched and in severe cases this can lead to edemas and subarachnoid hemorrhages [38-40]. The excessive stretching also leads to axonal damage and subsequent DAI.

To further examine BTBI in an ethical manner, researchers have turned to FEA which can simulate ideal blast scenarios safely and efficiently. Using FEA, Rezaei et al. [41] examined the effects of primary blast on intracranial pressure (ICP) and shear stresses within the brain. Considering blast in confined, semi-confined and open spaces, they found significant differences for each case but concluded that in each setting blast had a profound impact on ICP and shear stresses. Each case showed similar initial spikes in shear stresses but in the confined and semi-confined cases there were additional spikes due to the initial blast reflecting off the walls and hitting the head from a different direction. Examining the shear stresses regionally they found the highest shear stresses were located near the brain stem. Additionally, Eslaminejad et al. [42] examined primary blast using three different material models for the brain: hyper elastic, viscoelastic, and hyper viscoelastic. They found significant shear stresses present in each model with the highest and lowest stresses being in the viscoelastic and hyper viscoelastic models, respectively. In a separate study, Rezai et al. [43] examined blast in a confined space and observed that shear stresses can be increased by up to 135% when the head is in the proximity of

a wall, especially a corner. They also observed that due to the presence of CSF, a 4-6 MPa pressure experienced by the skull is reduced to about 150-250 kPa when it reaches the brain. This reduction in pressure demonstrates the effectiveness of CSF in mitigating head trauma and TBI.

Direct impact is a common injury mechanism of TBI and can be simply described as a foreign object contacting the human head and applying a mechanical load. The effects of direct impact are highly dependent on the magnitude and duration of the impact as well as the location and direction of the impact. Impacts are divided into perpendicular impacts and oblique impacts. A perpendicular impact occurs when the impact force is directed solely in the radial direction, towards the COM of the head and generates primarily linear acceleration within the head. Oblique impacts are applied at an angle to the COM and have both radial and tangential components. Thus, oblique impacts generate linear and rotational accelerations. Pure perpendicular impact is very rare and according to motorcycle accident statistics from Europe, the most common accident situation results in an oblique impact of $30 - 40^{\circ}$ [44]. Figure 2-7 depicts the differences between linear and oblique impacts and shows the corresponding effects on skull stress and strain in the brain.

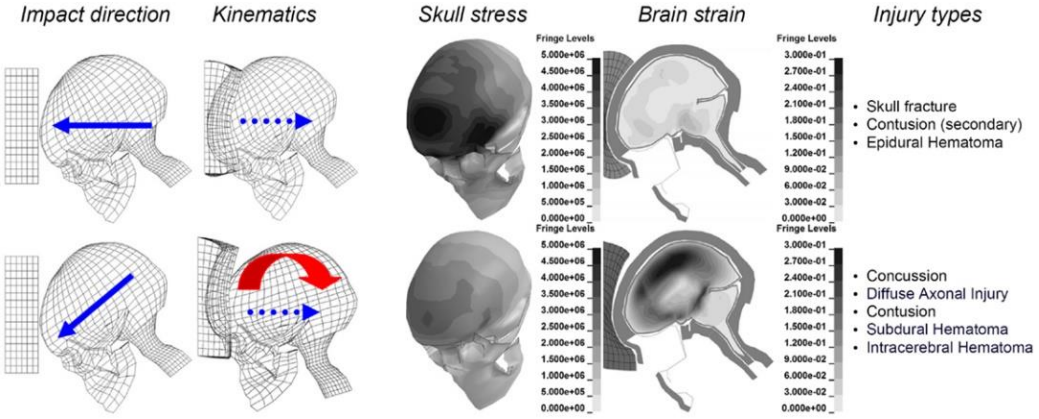

Figure 2-7: Illustration of biomechanics related to linear and oblique impact [45].

Using FEA, Kleiven et al. [45] examined von Mises stresses of the skull and principal strains within the brain. They examined two separate loading cases, one with purely perpendicular impact and another with an oblique impact at a 45° angle. From Figure 2-7, perpendicular and oblique impacts with the same magnitude have very different results for skull stress and brain strain. Perpendicular impact results in high skull stresses but relatively low principle strains in the brain. Conversely, oblique impact results in lower skull stresses but much higher brain strain. This relationship supports the work of Holbourn [46], who using 2-D gel models, claimed that rotational and not linear acceleration is the primary cause of a majority of TBIs. Furthermore, McElhaney et al. [47] determined that the brains bulk modulus is 5-6 orders of magnitudes larger than the shear modulus. Hence, the brain is much more sensitive to rotational acceleration and the brain primarily deforms in shear.

These cases described above involve the head contacting a solid and rigid structure such as a wall or the ground, but ballistic impact is also an important form of direct impact. Ballistic impact involves small objects with relatively low mass traveling at high speeds. Kinetic energy is defined as,

$$K_e = \frac{1}{2}mv^2, \tag{2.2}$$

where m is the mass of the object and v is the velocity. Due to the high velocity and its quadratic relationship with energy, the low mass ballistic projectile can still apply substantial energy to the human head despite its low mass. Ballistic projectiles could be small debris, bullets, or athletic equipment such as baseballs or golf balls. Ballistic impact can often cause skull fracture and penetration injuries, but this section is concerned with ballistic impact resulting in closed head injuries. Farid et al. [48] examined frontal and lateral golf ball impact for adults and children using FEA. Through their work, in the adult case they determined slightly greater shear strain for

lateral impact compared to frontal impact. However, for the child subjected to lateral impact, shear strains were nearly twice as high as their frontal impact counterparts. Additionally, Zhang et al. [49] examined frontal and lateral impact and determined the corresponding skull deformation, ICP, and shear stress and strain in the brain. Lateral impact resulted in higher values for all measured criterion and maximum shear stresses and strains were found highest near the brain stem and corpus callosum. These works suggest that along with rotational acceleration, the brain is also more sensitive to lateral impact.

TBI due to rapid or sudden acceleration and deceleration is often called “whiplash” and is very similar to other injury mechanisms except for no external force is applied to the head. Instead, any forces imparted on the brain are purely a consequence of inertial loading between the brain and inside of the skull. As discussed earlier, the brain is suspended in CSF and is not directly attached to the skull and because of this it can move separately from the skull. Newton’s first law of motion states that an object at rest will stay at rest and an object in motion will stay in motion unless acted upon by an external force. When the head is rapidly accelerated from rest, the brain wants to stay in place and is only put into motion when it contacts the skull. Similarly, rapid deceleration or change of direction can lead to the same inertial loading and subsequent TBI. The brain tends to maintain its original path and velocity until it contacts the skull; thus, changing its direction due to inertial forces. The force between the skull and brain is a function of acceleration and if the magnitude of acceleration is high enough the force can cause contusions and DAI. Zhang et al. [50] used FEA in conjunction with injury data collected by the National Highway Traffic Safety Administration (NHTSA) to examine the role of linear and rotational acceleration on principle strain experienced in the brain. They considered three cases of acceleration-based loading and determined that rotational acceleration is primarily responsible

for strain experienced in the brain (Table 2-3). This further confirms that the brain is more susceptible to rotational acceleration and loading.

Table 2-3: Maximum principle strain due to acceleration loading [50]. BrainLeft, BrainRight, and BrainBot correlate to the left, right, and bottom sides of the cerebrum, respectively. ByFalx indicates the region of the cerebrum near the falx membrane.

Case #	Acceleration Loading	Maximum Principle Strain			
		BrainLeft	BrainRight	BrainBot	ByFalx
1	Linear + Rotational	13.9%	15.7%	9.7%	9.0%
2	Linear	1.6%	1.6%	1.2%	0.6%
3	Rotational	13.9%	15.1%	11.7%	9.4%

In addition, Chu et al. [51] used FEA to investigate DAI caused by rotational acceleration. They determined initial strains to be concentrated near the corpus callosum and found a substantial contrecoup effect in both the corpus callosum and frontal lobe. A maximum strain of 1.26 was found in the corpus callosum during the contrecoup phase. According to Adams et al. [52], this correlates to a Grade 2 DAI, or focal lesion and damage to brain tissue.

2.2.4. Traumatic Brain Injury and American Football

American football is the most popular sport in the United States and 1.1 million high school athletes, and 70,000 collegiate athletes participate each year. In some states, children start tackle football at the age of 5. Over the course of the next 16 plus years of football, players endure hundreds or thousands of impacts to the head. It seems unreasonable to most, but to a football player it's worth it because that's what it takes to reach the National Football League (NFL). The NFL is a 63-billion-dollar industry and in 2017, NFL football games had an average viewership of 14.9 million people [53,54]. However, in recent years, interest in football has been slowly declining because of the increase in knowledge about the short-term and long-term effects of concussions. Football players are constantly making helmet to helmet contact with other players and frequently hitting their head on the ground. The NFL has attempted to institute rules

to limit these impact events, but it is impossible to eliminate them without completely changing the game. In the past two years, NFL superstars Rob Gronkowski and Luke Kuechly have retired at ages 29 and 28, respectively. Both players cited concussions as the reason for their early departure from the NFL. Youth football has also seen a decline in popularity because parents are seeking safer sports for their children's future. For the NFL, this loss of interest presents a very large financial concern. If athletes retire earlier and less young athletes pursue football, the quality of the NFL will decline and subsequently so will viewership and revenue. In 2016, in an effort to combat the declining popularity of football and to improve the health and safety of players, the NFL established a 100-million-dollar health initiative. Sixty million dollars was allocated towards technological advances related to football safety and another forty million dollars was to be put towards medical research specifically related to brain injuries [55].

Football helmets have been drastically improved over the years, but the overall basic design has remained the same. Football helmets are very successful at preventing skull fracture and other focal injuries such as contusions, lacerations, and hemorrhages. The outer shell of a helmet is made of hard plastic with a low coefficient of friction to help deflect blows and allow helmets to slide past one another. Additionally, the inside of the helmet is lined with padding to help reduce the force experienced during impact. The basic function of the padding is to increase the duration of the impact event; thus, reducing the linear acceleration experienced by the head. Unfortunately, traditional football helmets are relatively ineffective at protecting against rotational acceleration. The head is attached to the body via the neck which allows the head to rotate in three directions. Although, the helmet protects the brain from direct impact it cannot prevent the head from rotating because helmets do not restrict the motion of the neck in any direction. As discussed earlier, the brain is very susceptible to rotational acceleration and for that

reason concussions still occur frequently in football. VICIS, a Seattle based company, proposed a new helmet design to reduce rotational acceleration experienced by the brain. Their design utilized a layer of columns that attached the outer shell of the helmet to the inner padding layer. As the outer shell rotates, the columns are deformed which helps dissipate energy so the head experiences less rotational acceleration. In 2012, Subhash et al. [56] proposed using shear thickening fluids (STF) as a method to dissipate energy. His design allowed the outer shell and padding to move separately by utilizing a STF layer between the outer shell of the helmet and the inner padding. As the outer shell rotates, it generates shear stress within the STF. This shear stress forms hydro clusters within the STF and increases viscosity. The impedance to fluid flow dissipates energy so that the head experiences less rotational acceleration than the outer shell. In summation, if the neck is able to move freely, football players will always be susceptible to concussions. Safety measures can be implemented to help reduce the frequency and severity of concussions but will never truly be able to solve this inherent problem.

2.2.5. Chronic Traumatic Encephalopathy

The initial effects of MTBI are typically not life threatening and quickly subside. However, the effects of repetitive MTBI accumulate and can lead to the development of dangerous long-term effects. Chronic traumatic encephalopathy (CTE) is a long-term neurodegenerative disease resulting from repetitive concussive and subconcussive blows to the brain [57]. CTE is commonly seen in soldiers who are frequently exposed to blast, boxers, and NFL football players. CTE is a form of tauopathy and is very similar to Alzheimer's disease. Tauopathies are characterized by an abnormal buildup of hyperphosphorylated tau proteins within the brain. These proteins clump together and form neurofibrillary tangles (NFT) that

cause neuron loss in the brain [58]. CTE is also associated with enlarged ventricles and general atrophy of the brain (Figure 2-8), specifically the frontal and temporal lobes [59].

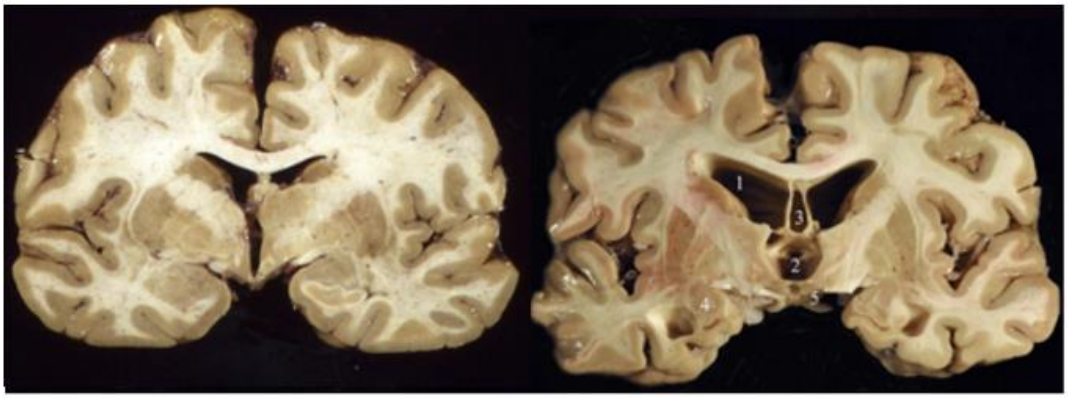

Figure 2-8: Coronal sections of a healthy human brain (left) and the brain of a retired football player with advanced CTE (right). Enlarged ventricles (1,2), septum cavity (3), atrophy of the temporal lobe (4), shrinkage of mammillary bodies (5) [59].

The damage to the brain caused by CTE leads to physical, cognitive, and behavioral problems. Chronic traumatic encephalomyelopathy (CTEM) is a specific type of CTE associated with the development of TDP-43 protein inclusions in the motor cortex. It develops into a motor neuron disease similar to amyotrophic lateral sclerosis (ALS) and is characterized by profound weakness, muscular atrophy, spasticity, fasciculations [60]. Cognitively, CTE can lead to memory impairment and problems with planning and organizing thoughts. Yet, CTE seems to have its biggest effect on the mood and behavior of a person. CTE can lead to insomnia, paranoia, and chronic depression [61]. Unfortunately, sometimes this chronic depression can lead to suicidal thoughts and if untreated these thoughts can lead to suicide. In addition, CTE can lead to lack of impulse control and increased aggression [59]. Paired together, impulsivity and aggression often lead to violence and physical altercations. These symptoms also make people with CTE more prone to addictive behavior and substance abuse. In 2008, Omalu et al. [62] examined 3 former NFL football players who died before the age of 50. In each case, the person had a substantial NFL career with the shortest career lasting 8 years and the longest 17 years.

Based on their premortem behavior and cause of death, these people were believed to suffer from CTE. An autopsy was performed on each brain and CTE was found in all of them. Prior to death, each subject showed evidence of headaches, memory impairment, poor decision making, paranoia, insomnia, major depression, drug abuse, and violent behavior. In two of these cases the cause of death was suicide and in 2010 this led Omalu et al. [63] to further investigate the alarming rate of suicides among retired football players. Studying 5 suicide cases of former NFL players, they found that in these cases the only common risk factor was CTE and the corresponding chronic depression. They also concluded that without extensive neuropathological tissue analysis, the presence of CTE might have gone unnoticed. None of the cases showed evidence of previous TBI and there was no significant atrophy of brain tissue; initially the brains appeared very normal. Furthermore, Goldstein et al. [64] analyzed a series of postmortem human brains from U.S military veterans who had experienced repetitive blast exposure and compared them to athletes of comparable age who had a history of concussive injuries. Evidence of CTE and NFTs were found in each military veteran. From their observations, they determined the blast associated CTE neuropathology was indistinguishable from the CTE neuropathology assoicated with repetitive impact experienced in athletics.

2.3. Constitutive Models for the Human Brain

In most FEA simulations involving TBI, the primary concern is stress and strain within the brain. Consequently, brain material properties are a critical factor in generating accurate and reliable results. It is widely accepted in academia that the brain exhibits hyper elastic and viscoelastic properties; thus, the hyper viscoelastic constitutive model has become the primary choice for brain tissue. Methods for determining material parameters vary across literature but

the fundamental mathematics remain the same. The following sections will discuss the formulation of a hyper viscoelastic model and implementation in literature.

A hyper elastic material is a special case of elastic material that can undergo large strains and displacement with relatively little change in volume. Two popular hyper elastic models are the Ogden and Mooney-Rivlin models. The Ogden model uses the principle stretches in polynomial form to determine the strain energy function as,

$$W = \frac{2\mu}{\alpha^2}(\lambda_1^\alpha + \lambda_2^\alpha + \lambda_3^\alpha - 3), \tag{2.3}$$

where W is the strain energy, μ is the undeformed shear modulus, $\lambda_{1,2,3}$ are the principle stretches, and α is a material parameter. Using the Ogden model and a convolution integral, Miller et al. [65] then proposed the following hyper viscoelastic model,

$$W = \frac{2}{\alpha^2}\int_0^t [\mu(t-\tau)\frac{d}{d\tau}(\lambda_1^\alpha + \lambda_2^\alpha + \lambda_3^\alpha - 3)d\tau. \tag{2.4}$$

The relaxation shear modulus μ is described as,

$$\mu = \mu_0[1 - \sum_{i=1}^{n} g_i(1 - e^{-\frac{t}{\tau_i}})], \tag{2.5}$$

where μ_0 is the instantaneous shear modulus, g_i is the relaxation coefficient, and τ_i is the characteristic time. Similarly, the Mooney-Rivlin model also utilizes the strain energy function but it is defined as,

$$W = C_{10}(J_1 - 3) + C_{01}(J_2 - 3) + \frac{1}{D_1}(J_{el} - 1)^2, \tag{2.6}$$

where C_{10}, C_{01} and D_1 are temperature-dependent material constants, J_{el} is the elastic volume ratio, and $J_{1,2}$ are the first and second invariants of the deviatoric strains. The corresponding Cauchy stress is determined by,

$$\sigma_{ij} = JF_{ik}^{T} \cdot S_{km} \cdot F_{mj}, \tag{2.8}$$

where σ_{ij} is the Cauchy stress, F is the deformation gradient tensor, and J is the Jacobian transformation. Furthermore, the second Piola-Kirchoff stress is determined using a convolution integral of the linear viscoelasticity as,

$$S_{ij} = \int_0^t G_{ijkl}(t-\tau)\frac{\partial E_{kl}}{\partial \tau}\, d\tau, \tag{2.7}$$

where S_{ij} is the second Piola-Kirchoff stress, E_{kl} is the Green's strain tensor, $G_{ijkl}(t-\tau)$ is the relaxation modulus. The relaxation modulus for the Mooney-Rivlin model can be described in terms of a Prony series as,

$$G(t) = G_0 + \sum_{i=1}^{n} G_i e^{-\beta_i t}, \tag{2.9}$$

where G_0 is the instantaneous shear modulus, G_i is the relaxation modulus, and β_i is the decay constant. Viscoelastic materials share properties of purely elastic materials and purely viscous fluids. This combination results in a material with a time-dependent strain response. The relaxation test is the most common way to characterize this time-dependency. During a relaxation test, stress in the brain is recorded while it is subjected to a constant strain. Over time, the stress value decreases exponentially. In other words, the shear modulus decreases exponentially as seen in Equations 2.5 & 2.9. The Ogden and Mooney-Rivlin models have both been successfully implemented in FEA applications with various methods of determining material parameters. Chafi et al. [66] successfully implemented a Mooney-Rivlin hyper viscoelastic model to monitor ICP and brain shear stresses during blast loading. Moreover, Chafi et al. [67] compared the stress and strain response of a brain subjected to blast loading using a Ogden hyperelastic model and a Mooney-Rivlin hyper viscoelastic model. They found the shear stresses to be to much higher in the Mooney-Rivlin hyper viscoelastic model compared to the

Ogden hyperelastic model; conversely, they found the principle strain to be much higher in the Ogden hyperelastic model compared to the Mooney-Rivlin hyper viscoelastic model (Figure 2-9).

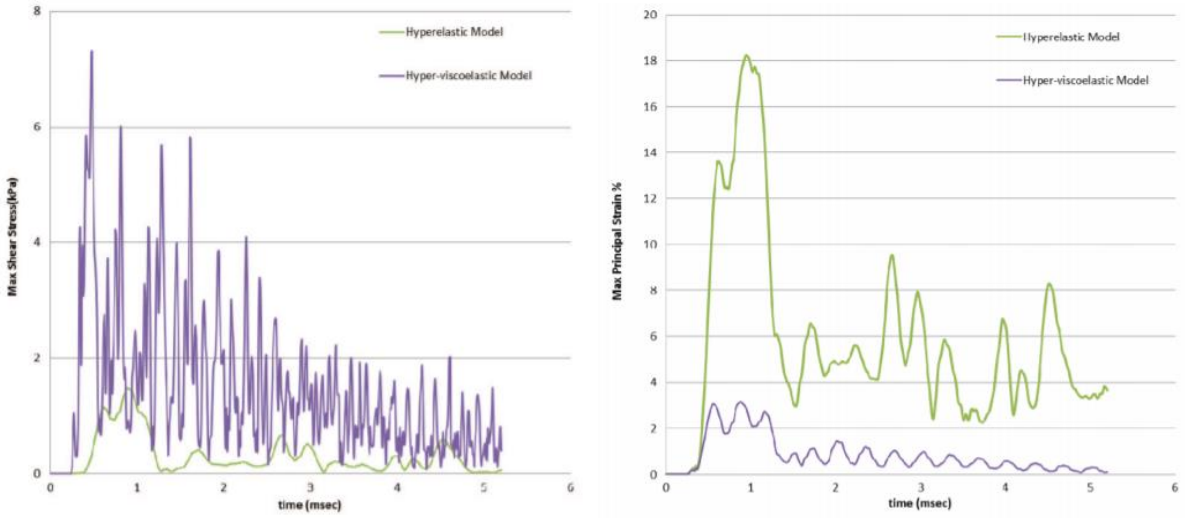

Figure 2-9: Maximum shear stresses and maximum prinicple strains of a human brain subjected to blast loading using an Ogden hyperelastic and Mooney-Rivlin hyper viscoelastic model [67].

Farid et al. [68] developed an Ogden hyper viscoelastic model for human brain tissue subjected to high strain rates. Using various strain rates, they applied unconfined compression to cylindrical samples of bovine brain tissue. Afterwards, the unconfined compression test was replicated using the FEA software ABAQUS. The simulation was not only able to accurately replicate stress-strain curves for the experimental strain rates but it also reasonably predicted stress-strain curves for other strain rates within the range (Figure 2-10).

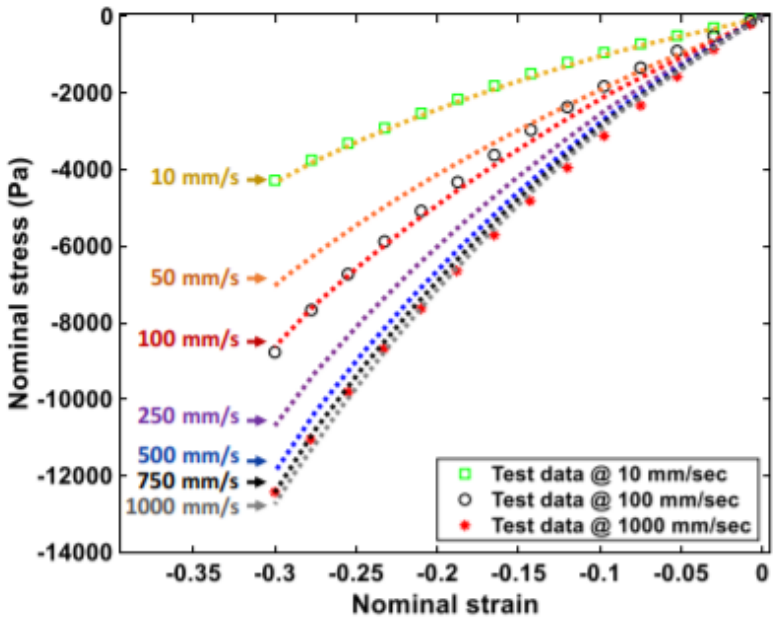

Figure 2-10: Predicted nominal stress-strain curves for bovine brain tissue subjected to unconfined compression using an Ogden hyper viscoelastic model [68].

2.4. Modal Analysis and Dynamic Mode Decomposition

Modal analysis is the study of the dynamic properties of a system to determine the resonant frequencies, also called natural frequencies. When a structure experiences vibration at one of these resonant frequencies, it exhibits resonance. Resonance is caused by the interaction between the inertial and elastic properties of materials within a structure [69]. When a structure resonates, the vibration experienced by the structure is amplified to an excessive and often dangerous amplitude. This is particularly important in mechanical design. Vibration comes from many sources; it can be induced by wind blowing across a building or transmitted from an engine through a vehicle to critical electrical components. In each case, resonance leads to excessive deformation and damage that compromises the functionality of the system. Regarding the brain, this excessive deformation correlates to an increase in strain and subsequently the stretching of axons and axonal injuries which lead to concussions.

In mathematical terms, modal analysis is described by an eigenvalue problem. For direct methods of modal analysis, a non-damped linear system must be considered. Equation 2.10 shows the equation of motion for this dynamical system,

$$[M]\{\ddot{u}\} + [K]\{u\} = 0, \tag{2.10}$$

where $[M]$ is the equivalent mass matrix, $[K]$ is the equivalent stiffness matrix, $\{u\}$ is displacement, and $\{\ddot{u}\}$ is acceleration. By assuming harmonic motion, a solution can be assumed such that,

$$u(t) = Ae^{i\omega t}, \tag{2.11}$$

$$\frac{d^2u(t)}{dt^2} = -\omega^2 Ae^{i\omega t}, \tag{2.12}$$

where t is time and ω is the natural frequency. By substituting Equations 2.11 & 2.12 into Equation 2.1, the system becomes,

$$-\omega^2[M]Ae^{i\omega t} + [K]Ae^{i\omega t} = 0. \tag{2.13}$$

Collecting terms and rearranging, the system takes the form of a standard eigenvalue problem,

$$([K] - [M]\omega^2)Ae^{i\omega t} = 0. \tag{2.14}$$

The system has a non-trivial solution, $A \neq 0$, if and only if,

$$|[K] - [M]\omega^2| = 0. \tag{2.15}$$

Solving this equation will result in n natural frequencies for an n-DOF system. The corresponding n mode shapes, ϕ_i, can be determined by,

$$\phi_i = ([K] - [M]\omega_i^2)A_n, \tag{2.16}$$

where A_n is the normalized A matrix. Unfortunately, the brain cannot be analyzed using direct methods because it is a nonlinear material. Instead, numerical techniques must be implemented to approximate natural frequencies and the corresponding mode shapes.

DMD was first formulized by P.J. Schmid in 2009, seeking to develop a method of modal analysis that was equally applicable for both experimental and numerical data [70]. Schmid aimed to create a 'matrix-free' formulation that relied on gathered data and did not depend on any information regarding the underlying system matrix. Schmid concentrated on a data-based approach rather than a model-based approach. DMD is completely unique and is quite similar to other numerical techniques, such as proper orthogonal decomposition (POD) and bi-orthogonal decomposition (BOD). POD employs energy ranking to compare orthogonal structures gathered from snapshots of flow vectors. The POD modes are gathered from singular value decomposition as,

$$V_1^{N-1} = U\Sigma W^H, \tag{2.17}$$

where V_1^{N-1} is the snapshot matrix, U contains the spatial modes, W contains the temporal modes, and the diagonal values of Σ represent the energy ranks. POD has been successfully used for fluid flow by Berkooz et al. [71] but it has two main limitations. First, sometimes energy is not the proper parameter to rank modes and secondly, POD uses second order statistics, so phase information is lost. BOD is very similar to POD and determines the eigenvectors for both the spatial and temporal matrices. Yet again, BOD uses second order statistics and loses valuable transient information. DMD does not lose this phase information and is superior to POD in highly transient events, such as head impact. DMD is better equipped to capture the intrinsic nonlinearities present in the human brain [70].

To understand DMD, first consider brain nodal displacement collected as a series of snapshots in time. Each snapshot is separated by a constant time interval Δt. This sequence of N snapshots is collected as a series of column vectors given by the matrix V_1^N,

$$V_1^N = \{v_1, v_2, v_3, \dots, v_{N-1}, v_N\}, \tag{2.18}$$

where v_i represents the i^{th} snapshot of nodal displacement data. V_1^N is an *M* x *N* matrix consisting of *M* nodal displacements separated into *N* snapshots in time. Furthermore, this study assumes the presence of a linear mapping coefficient *A* that connects the flow field v_i to the subsequent flow field v_{i+1}, such that,

$$v_{i+1} = Av_i, \tag{2.19}$$

and *A* is assumed to remain constant throughout the sequence. In the case of a nonlinear system such as the brain, this amounts to a linear tangent approximation between snapshots. Thus, in combination with Equation 2.2, Equation 2.1 can be rewritten as,

$$V_1^N = \{v_1, Av_1, A^2v_1, \dots, A^{N-2}v_1, A^{N-1}v_1\}. \tag{2.20}$$

The goal of DMD is then to extract the dynamical characteristics of *A* based on the data described by V_1^N. In a complex dynamical system like the human brain with thousands or millions of nodes, constructing the matrix *A* can be computationally expensive and inefficient. Therefore, to avoid constructing the matrix *A*, this study utilizes singular value decomposition to construct a much smaller matrix $\tilde{S}$. The matrix $\tilde{S}$ is related to *A* through a similarity transform, thus, the dynamic characteristics of $\tilde{S}$ are the same as *A*. To construct $\tilde{S}$, first separate the snapshot matrix V_1^N into two submatrices V_1^{N-1} and V_2^N such that,

$$V_1^{N-1} = \{v_1, v_2, v_3, \dots, v_{N-2}, v_{N-1}\}, \tag{2.21}$$

$$V_2^N = \{v_2, v_3, v_4, \dots, v_{N-1}, v_N\}, \tag{2.22}$$

$$V_2^N = AV_1^{N-1}. \tag{2.23}$$

Using singular value decomposition (SVD), V_1^{N-1} is decomposed into matrices $U, \Sigma,$ and W by,

$$V_1^{N-1} = U\Sigma W^H. \tag{2.24}$$

By inserting $U\Sigma W^H$ into Equation 2.6 and reorganizing the matrices, $\tilde{S}$ can be determined by,

$$U^H A U = U^H V_2^N W \Sigma^{-1} \equiv \tilde{S}. \tag{2.25}$$

As discussed before, $\tilde{S}$ is related to *A* through a similarity transformation. Looking back at POD, in Equation 2.17 the matrix *U* contains the spatial modes of the system and from Equation 2.19 it is known that matrix *A* represents a linear mapping coefficient one step forward in time. So, it can be seen from Equation 2.25 that $\tilde{S}$ better describes the transient properties of the system. Additionally, the eigenvalues of $\tilde{S}$ are the eigenvalues of *A* and the eigenvectors of *A* can be determined from the eigenvectors of $\tilde{S}$ as such,

$$\phi_i = U y_i, \tag{2.26}$$

where y_i is the i^{th} eigenvector of $\tilde{S}$ and ϕ_i is the i^{th} eigenvector of *A*. The future state of each eigenvector, or mode shape, can be predicted for all time in the future by using the Koopman operator [72]. The Koopman operator is linear with respect to time and can be described as,

$$\omega_k = \frac{\ln(\mu_i)}{\Delta t}, \tag{2.27}$$

where μ_i is the i^{th} eigenvalue of $\tilde{S}$ and Δt is the time step interval.

Then the approximate solution for all future times, $x_f(t)$, can be described by,

$$x_f(t) = b_k \theta_i e^{\omega_k t}. \tag{2.28}$$

Schmid et al. [73] successfully employed DMD to extract the dynamic modes from fluid flow produced by a helium jet. Figure 2-11 shows Schlieren snapshots of the fluid flow collected experimentally and Figure 2-12 shows the corresponding dynamic modes generated by DMD. The two sets of figures show significant similarities. First, the dynamic modes generated by DMD show the same slanted waveform shape seen in the experimental images. Also, the dynamic modes show density gradients near the outer edges of the wave front and a breakdown

of the wave front as the wave gets further downstream from the jet. This phenomenon is also seen in the Schlieren images of the fluid flow and aligns with physical intuition. These similarities show that DMD can successfully extract the spatial and temporal characteristics of fluid flow.

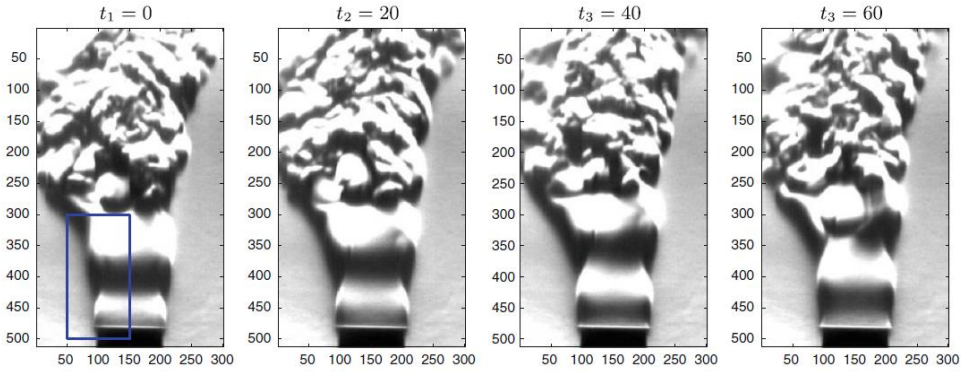

Figure 2-11: Schlieren photos of fluid flow created by a helium jet [73].

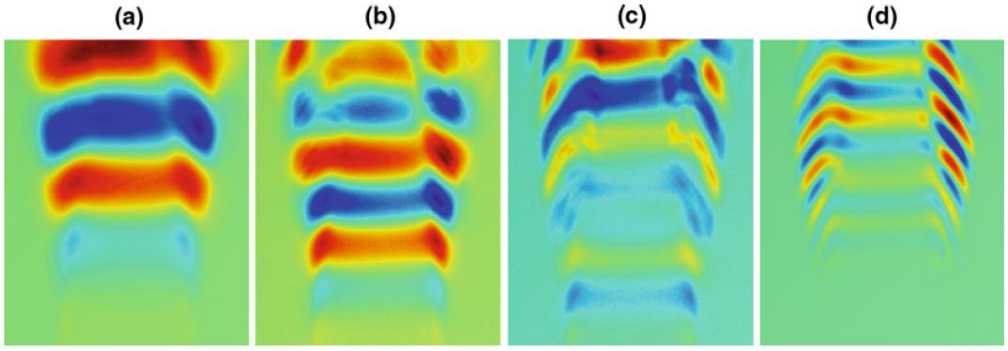

Figure 2-12: Dynamic modes of helium jet flow generated by DMD [73].

Additionally, Mann et al. [72] implemented DMD to develop financial trading strategies based on the speed and precision of numerical techniques. Using the Koopman operator in conjunction with DMD, they predicted the growth and decay of markets for portfolios of financial data. DMD does not need to understand the governing equations of the market strategy. Thus, the time period that the data is collected for can be truncated for various time periods and provide extensive information quickly. Trading algorithms account for over a third of financial decisions made in the stock market and DMD presents a robust, model free, numerical approach [72].

Finally, Laksari et al. [74] implemented DMD to examine the spatiotemporal characteristics of brain deformation in football players. Kinematic data was collected for 31 football players using custom-built mouthguards that were instrumented with a triaxial accelerometer and triaxial gyroscope. In total, 537 impact events were recorded, and 187 impacts were randomly chosen to replicate using FEA. These impacts contained both linear and rotational components of acceleration. In their study, they identified amplified strain values at a frequency around 28 Hz. They were also able to successfully correlate modal amplitude to the Fourier modes of displacement traces for single nodes (Figure 2-13). Thus, they concluded that deformation in the brain is highly dependent on frequency and the brain is most susceptible to frequencies in the range of 20-40 Hz.

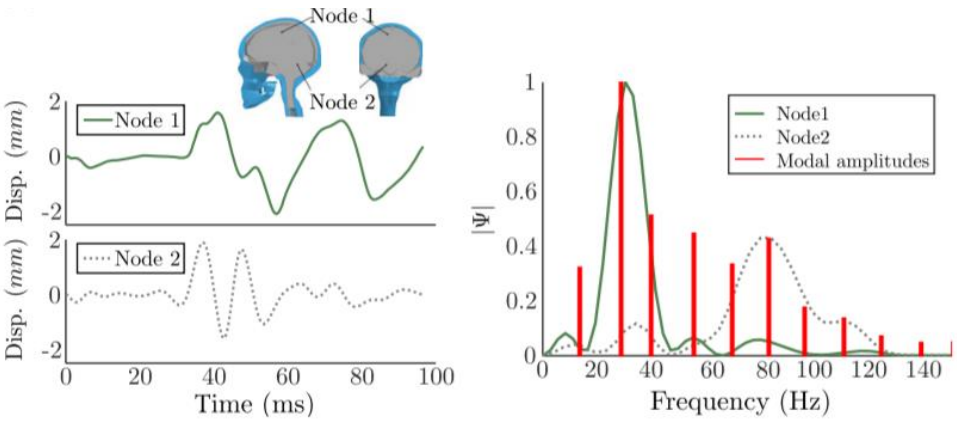

Figure 2-13: Modal amplitudes generated using DMD superimposed on the Fourier modes of two singular nodes in the brain [74].

CHAPTER 3. NUMERICAL SETUP, PROCEDURE, AND ANALYSIS

3.1. Finite Element Head Model and Material Properties

The 3-dimensional finite element head model used in this study was developed in 2003 by Horgan and Gilchrist and later modified by Chafi and Karami in 2010 [75]. The geometry of this model was generated using computed tomography (CT) scans from the National Institute of Health (NIH). The model was validated by simulating impact tests conducted by Nahum et al. [76] and then directly comparing predicted ICP time histories against values obtained experimentally. This head-neck system, shown in Figure 3-1, models all major components of the human head using 23,361 eight-noded brick elements and 5344 four-noded shell elements. The facial bone, scalp, and skull were modeled using eight-noded brick elements with one, two, and four layers respectively. The brain, neck, and CSF were also modeled with eight-noded brick elements. Additionally, the system is fixed in place by applying a rigid support boundary constraint to the bottom layer of the neck. Thus, the linear and rotational movement of the head depend on the neck as well.

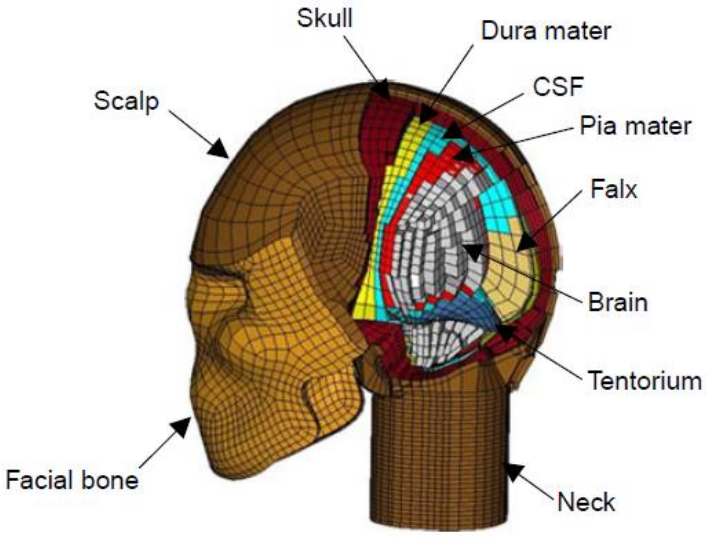

Figure 3-1: Identification of the main components of the Horgan-Gilchrist Model [75].

The membranes of the human head such as the dura mater, pia mater, falx and tentorium were modeled using four-noded shell elements. The scalp, skull, neck, dura mater, pia mater, and tentorium were all modeled as linear elastic materials. Meanwhile, the CSF was modeled using an elastic fluid so that it does not bear shear stress but is able to carry the hydrostatic stress. The brain itself was modeled using a Mooney-Rivlin hyper viscoelastic model developed by Mendis et al. [77]. These mechanical properties are summarized in Table 3-1 and Table 3-2.

Table 3-1: Material properties for main head components

Component Name	**Constitutive Model**	**Finite Element Model**	**Density** $(\frac{kg}{m^3})$	**Young's Modulus** E **(MPa)**	**Poisson's Ratio**		
Tentorium	Linear Elastic	Shell Element	1133	31.5	0.45		
Dura Mater	Linear Elastic	Shell Element	1133	31.5	0.45		
Pia Mater	Linear Elastic	Shell Element	1130	11.5	0.45		
Falx	Linear Elastic	Shell Element	1133	31.5	0.45		
Skull	Linear Elastic	Solid Element	1935	4097	0.22		
Neck-Bone	Linear Elastic	Solid Element	1300	1000	0.24		
Neck-M	Linear Elastic	Solid Element	1130	0.1	0.45		
Face-Bone	Linear Elastic	Solid Element	1935	4097	0.22		
Face-Skin	Linear Elastic	Solid Element	1200	16.7	0.42		
Scalp	Linear Elastic	Solid Element	1200	16.7	0.42		
Spinal	Viscoelastic	Solid Element	1040	-	-		
CSF	Linear Elastic Fluid	Solid Element	1040	14.89	Poisson's Ratio	Bulk Modulus K	Viscosity
					0.489	2190	0.2

Table 3-2: Material parameters for the Mooney-Rivlin hyper viscoelastic brain model [77].

Material Model	**Density** $(\frac{kg}{m^3})$	**Mechanical Properties**						
Hyper Viscoelastic	1040	Elastic Bulk Modulus (MPa)	C_{10} (Pa)	C_{01} (Pa)	G_1 (kPa)	G_2 (GPa)	$\beta - 1$ (s^{-1})	$\beta - 2$ (s^{-1})
		2190	3102.5	3447.2	40.744	23.285	125	6.67

3.2. Impact Simulation

One of the main focuses of this study is to observe how varying the direction of impact affects the dynamic modes within the skull. Subsequently, using the COM of the head as the center of rotation and designating the anterior direction as 0°, impact was simulated in 45° increments within the sagittal plane for a range varying from $0° - 180°$ (Figure 3-2).

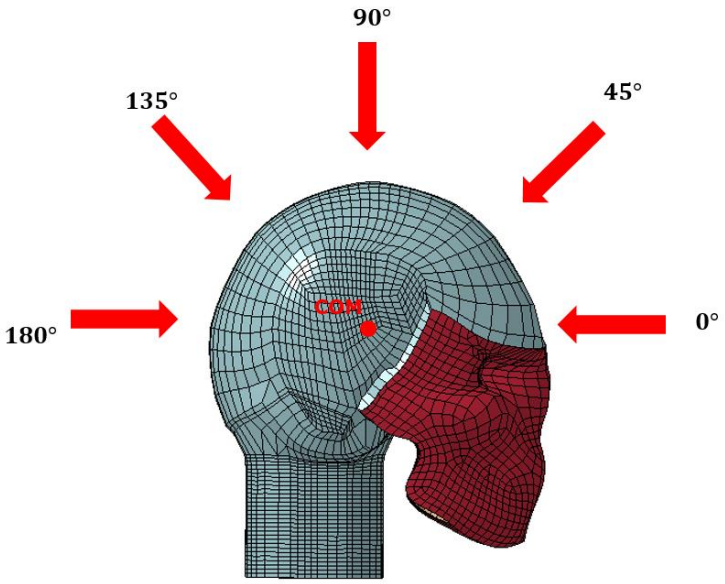

Figure 3-2: Depiction of the varying angles of impact within the sagittal plane and the location of the COM of the head.

Direct impacts were generated using a 5.58 kg steel cylinder. The cylinder was positioned so that its COM was coincident with the given impact angle. However, the human head is not a perfect sphere so the radial and tangential directions are not separated by 90°. Thus, to promote flush and even contact, the cylinder was slightly rotated about its COM so that the axial axis of the cylinder formed a 90° angle with the tangential direction of the contact plane. The cylinder was then given an initial velocity in the direction of the impact angle. Therefore, the velocity vector and cylinder axis are not collinear, and the velocity vector is not normal to the contact plane. An example of these directions and adjustments are detailed for the 0° impact angle in Figures 3-3 & 3-4.

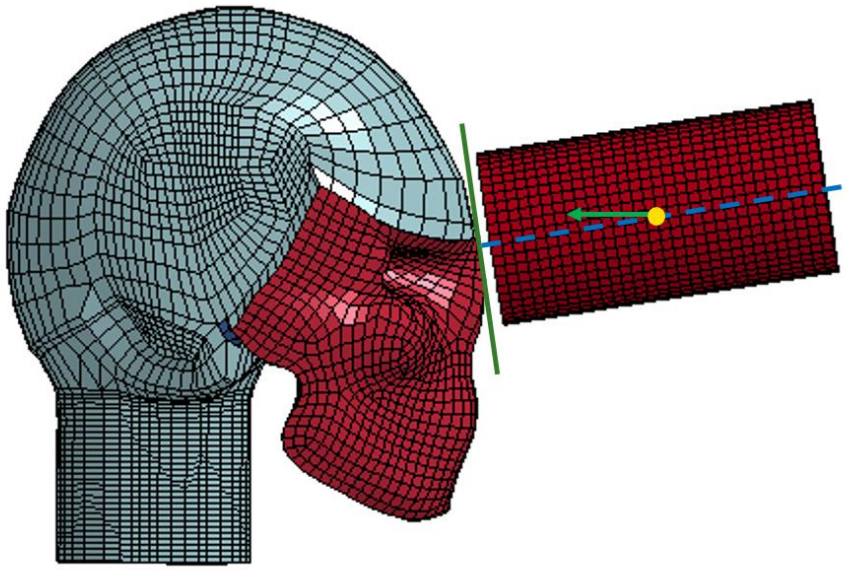

Figure 3-3: Schematic depicting the overall setup of direct impact using a steel cylinder.

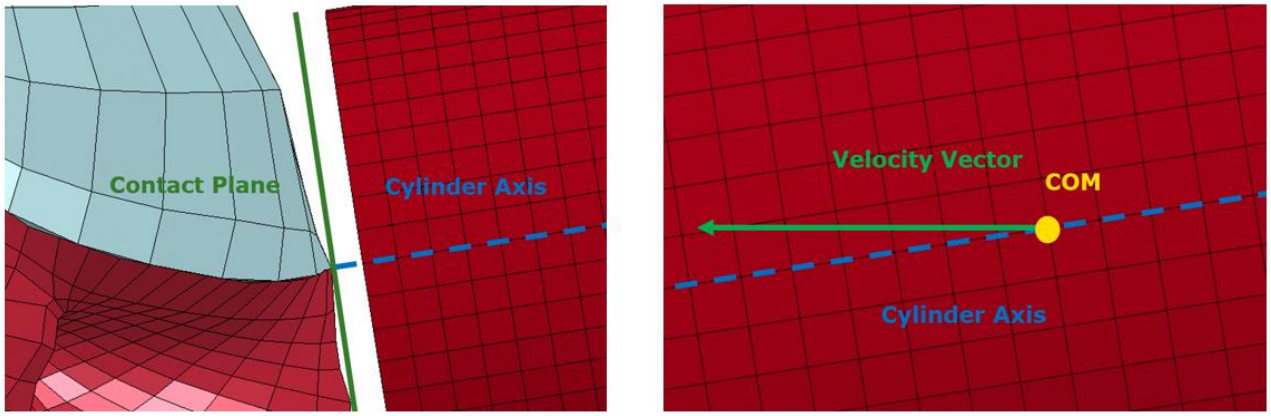

Figure 3-4: Detailed schematic of direct impact setup at the contact plane (left) and the COM of the steel cylinder (right). It is important to note that the cylinder axis is normal to the contact plane and the velocity vector is not collinear with the cylinder axis.

Initial velocities varied across impact angles and were dependent on the generated HIC_{15}. As discussed earlier, HIC_{15} values for concussive level impacts vary greatly across literature [29-31]. However, an extensive study by Beckwith et al. [28] determined a mean HIC_{15} of 321.5 for concussive impacts. So, to conservatively ensure that generated impacts were concussive level, this study aimed to generate HIC_{15} values in the range of 350-450. Using educated trial and error, initial velocities were adjusted for each impact angle until the HIC_{15} fell within the desired range. To determine the HIC_{15}, the acceleration for the COM of the head was evaluated for the entire 15ms simulation time and then converted to g's. Using this data, the HIC_{15} was determined using Equation 2.1. The corresponding initial velocity and HIC_{15} for each impact angle is tabulated in Table 3-3.

Table 3-3: Initial velocities and HIC_{15} for different impact angles.

Impact Angle	0°	45°	90°	135°	180°	Average
Initial Velocity (m/s)	5.00	4.53	3.60	4.53	5.00	4.53
HIC_{15}	395.35	398.35	355.41	398.83	407.22	391.03

Next, the complete rigid body motion of the head does not describe the vibrations within the brain. To extract the brain displacement due to vibration, the rigid body motion must be subtracted from the system. This was done using a Follow command within LS-DYNA. Using the skull as a reference body, a follow plane was constructed by selecting 3 nodes of the skull. This follow plane establishes a new coordinate system that follows the rigid body motion of the skull. This essentially eliminates any rigid body motion of the brain in all 6 of the cartesian degrees of freedom (DOF). Now the relative nodal brain displacements are described in this new coordinate system and are entirely due to vibration. Finally, for each impact direction, two groups of nodes were selected. The first group of nodes was selected in the cerebrum and near the corpus callosum. The second group was selected in the occipital lobe near the brain stem. These areas were selected because studies have shown that shear waves and the resulting strains, concentrate near the corpus callosum and brain stem [7,49]. The locations of these selections are shown in Figure 3-5.

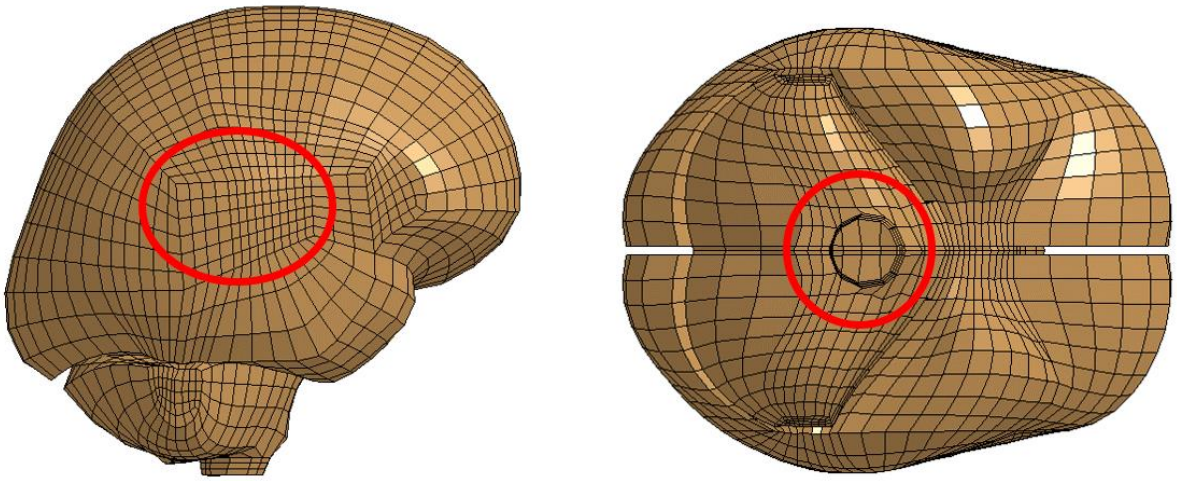

Figure 3-5: Region of nodes in the cerebrum near the corpus callosum (left). Region of nodes in the cerebellum near the brain stem (right).

To extract the dynamic modes of vibration, these selected nodes were then entered into the DMD code detailed in the Appendix. This DMD code was verified using a sinusoidal waveform previously studied by Laksari et al. [74]. By creating and implementing a novel MATLAB code and comparing the generated solutions, this study was able to verify the functionality and accuracy of the DMD code. The sinusoidal signal, $u(t)$, was in the following form:

$$u(t) = \sin(k_1 x + \omega_1 t)\, e^{-\lambda_1 t} + \sin\,(k_2 x + \omega_2 t) e^{-\lambda_2 t} \tag{3.1}$$

where $k_1 = 10, k_2 = 30, \omega_1 = 20, \omega_2 = 60, \lambda_1 = -3$, and $\lambda_2 = -5$. This signal is a combination of two distinct linear spatiotemporal substructures that are decaying overtime. The plotted sinusoidal function can be seen in Figure 3-6.

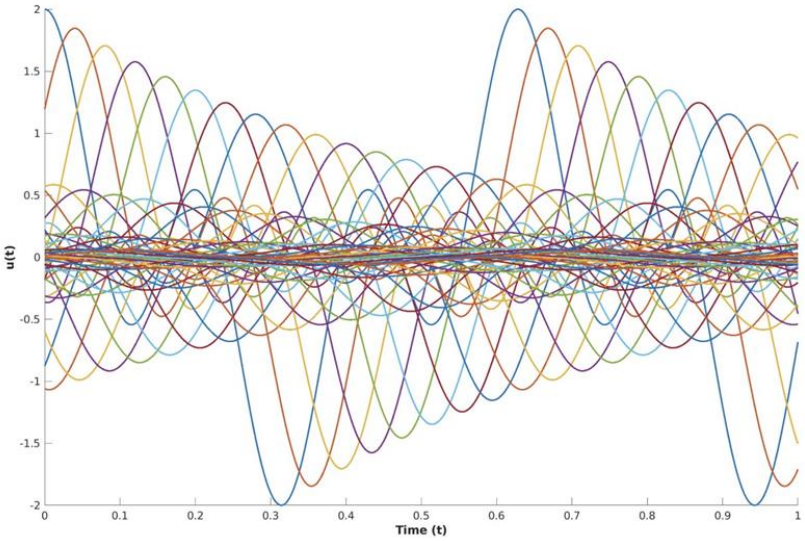

Figure 3-6: Laksari sinusoidal function used to verify the novel DMD code.

As discussed earlier, data can be truncated for the DMD method to reduce computational cost. The singular matrix, Σ, provides scaling for the modal amplitudes of dynamic modes. This matrix is determined during SVD. By plotting the diagonal values of Σ (Figure 3-7), it can be seen that modal amplitudes become negligible after five modes. Thus, the three matrices

determined using SVD are truncated into three 5×5 matrices, greatly reducing the overall computational cost.

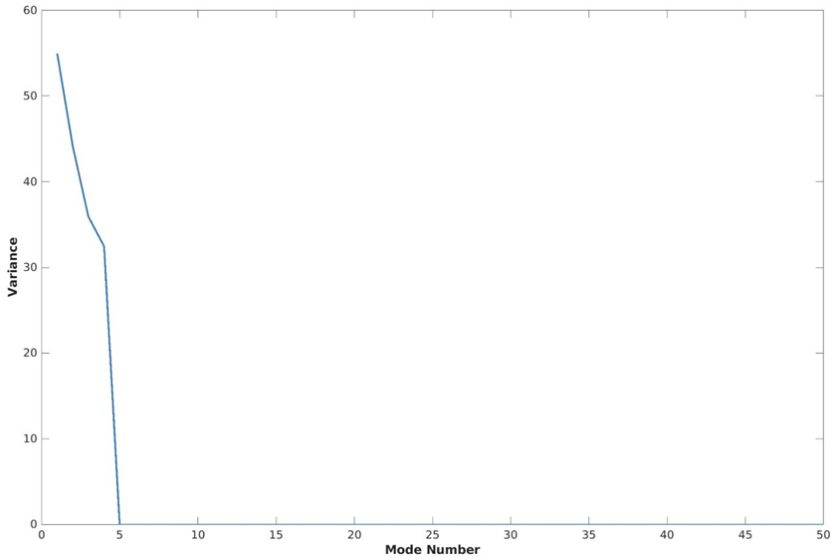

Figure 3-7: Diagonal values of the singular matrix determined from SVD.

Using DMD, the first and third modes were extracted from the system are plotted in Figure 3-8. Then, the frequencies and decay rates of each mode were determined using the Koopman operator. The Koopman operator is a complex number where the real part represents the mode frequency and the imaginary part represents the decay rate. The first mode had a frequency of 3 and a decay rate of 19.9916 and the third mode had a frequency of 5 and a decay rate of 59.9573. These values do not have units because in this sample no units were established for time or amplitude, so frequency and decay rates are dimensionless. It is important to note that the second mode was skipped because it represents the complex conjugate of the first mode. The second mode has the same decay rate as the first mode, but its frequency is negative. Furthermore, using Equation 2.28, the future states of the first and third modes were predicted as they decay over time (Figure 3-9). The frequencies, decay rates, and future state predictions determined using this DMD code are identical to those determined by Laksari. This verified the

functionality of the novel DMD code and its ability to be applied to modal analysis of the human brain.

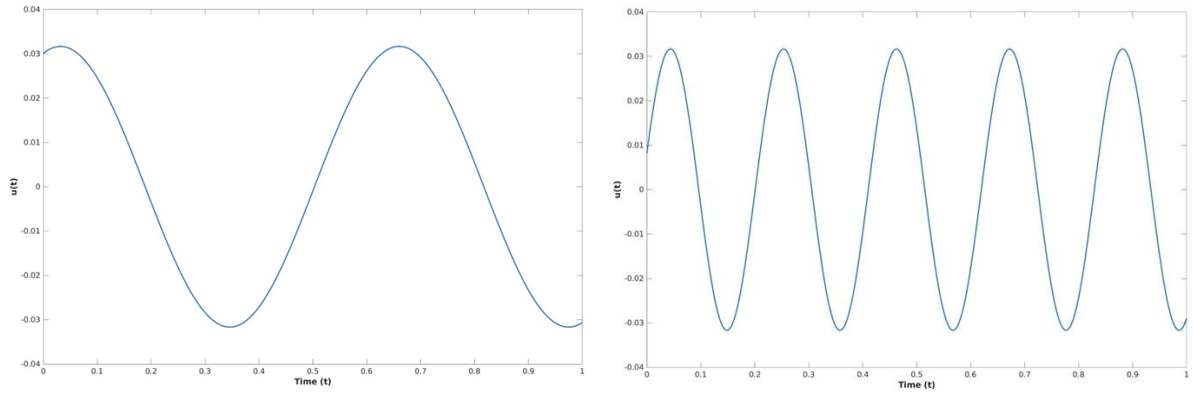

Figure 3-8: The first mode of vibration at a frequency of 3 (left). The third mode of vibration at a frequency of 5 (right).

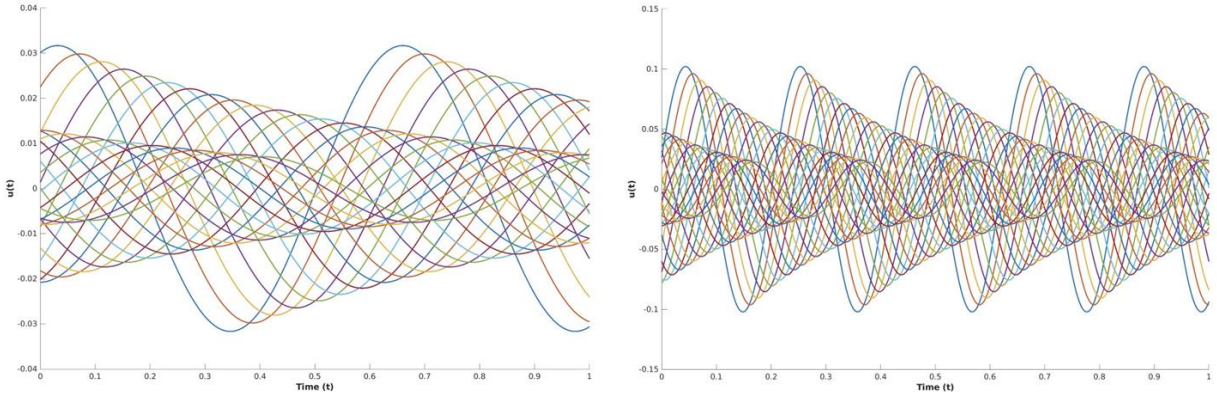

Figure 3-9: The first mode decaying at a rate of 19.9916 (left). The third mode decaying at a rate of 59.9573 (right).

CHAPTER 4. RESULTS AND DISCUSSION

4.1. Relative Displacements

To monitor displacement, 3 axes were established to create a 3D coordinate system. The coronal, sagittal, and axial directions are defined as the normal directions to the coronal, sagittal, and axial planes, respectively. A group of nodes were selected within the cerebrum near the corpus callosum. For each impact direction, their total relative displacements, along with displacements in the sagittal, coronal, and axial directions were monitored for 15 milliseconds and are plotted in Figures (4-1) - (4-5). This process was repeated for a group of nodes within the cerebellum near the brain stem and those displacements are plotted in Figures (4-6) - (4-10).

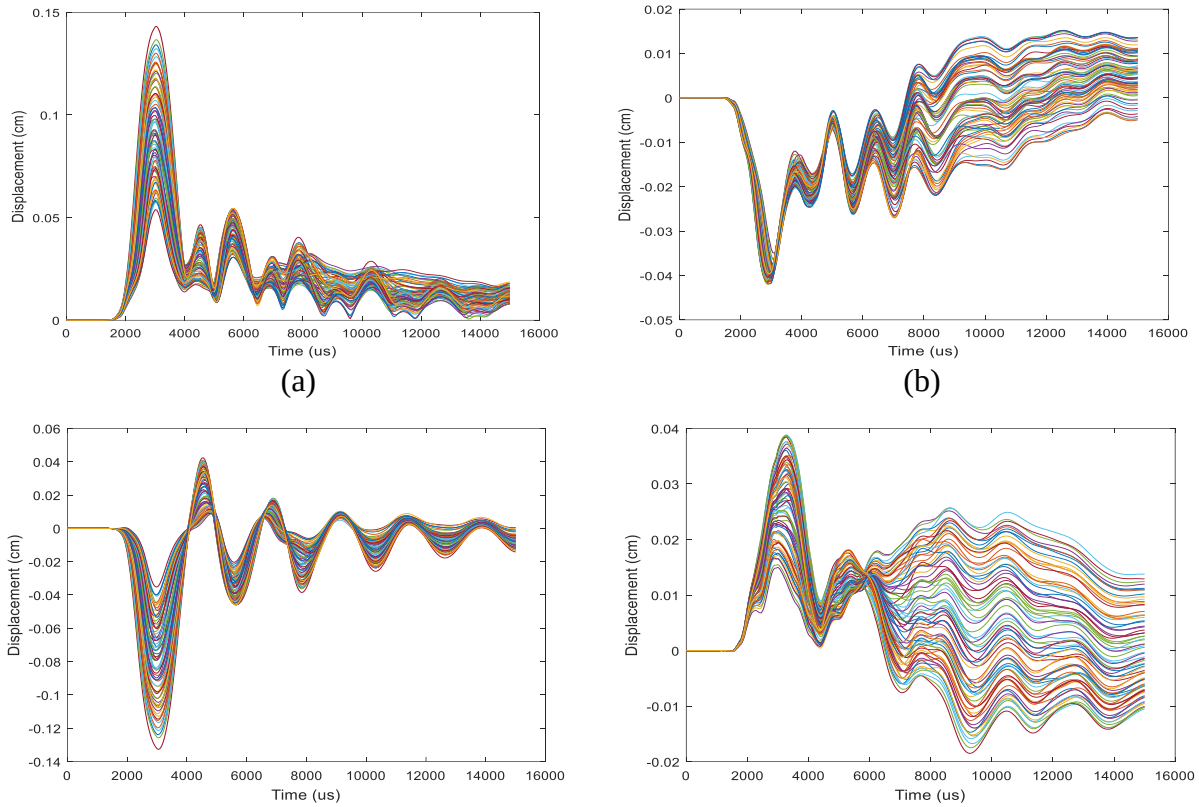

Figure 4-1: (a) Total relative displacement of nodes near the corpus callosum for 0° impact angle. (b) Relative displacement for 0° impact angle in coronal direction. (c) Relative displacement for 0° impact angle in the sagittal direction. (d) Relative displacement for 0° impact angle in the axial direction.

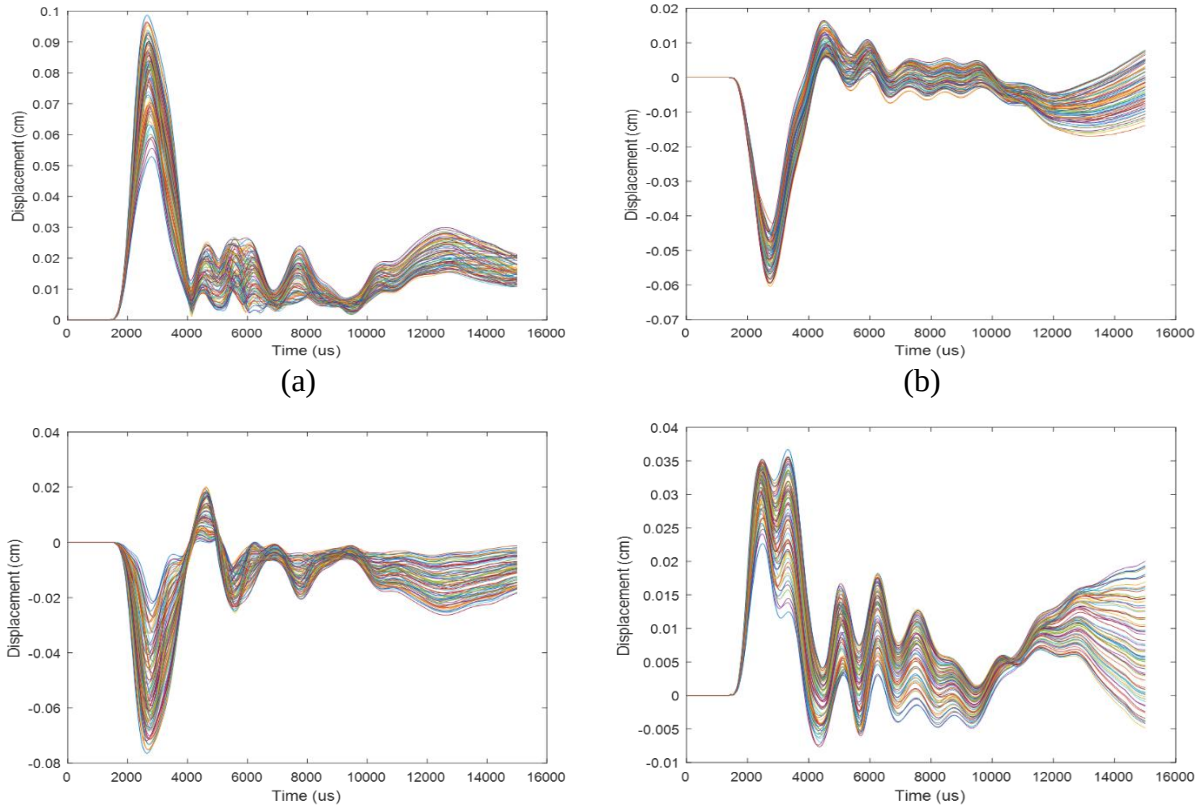

Figure 4-2: (a) Total relative displacement of nodes near the corpus callosum for 45° impact angle. (b) Relative displacement for 45° impact angle in coronal direction. (c) Relative displacement for 45° impact angle in the sagittal direction. (d) Relative displacement for 45° impact angle in the axial direction.

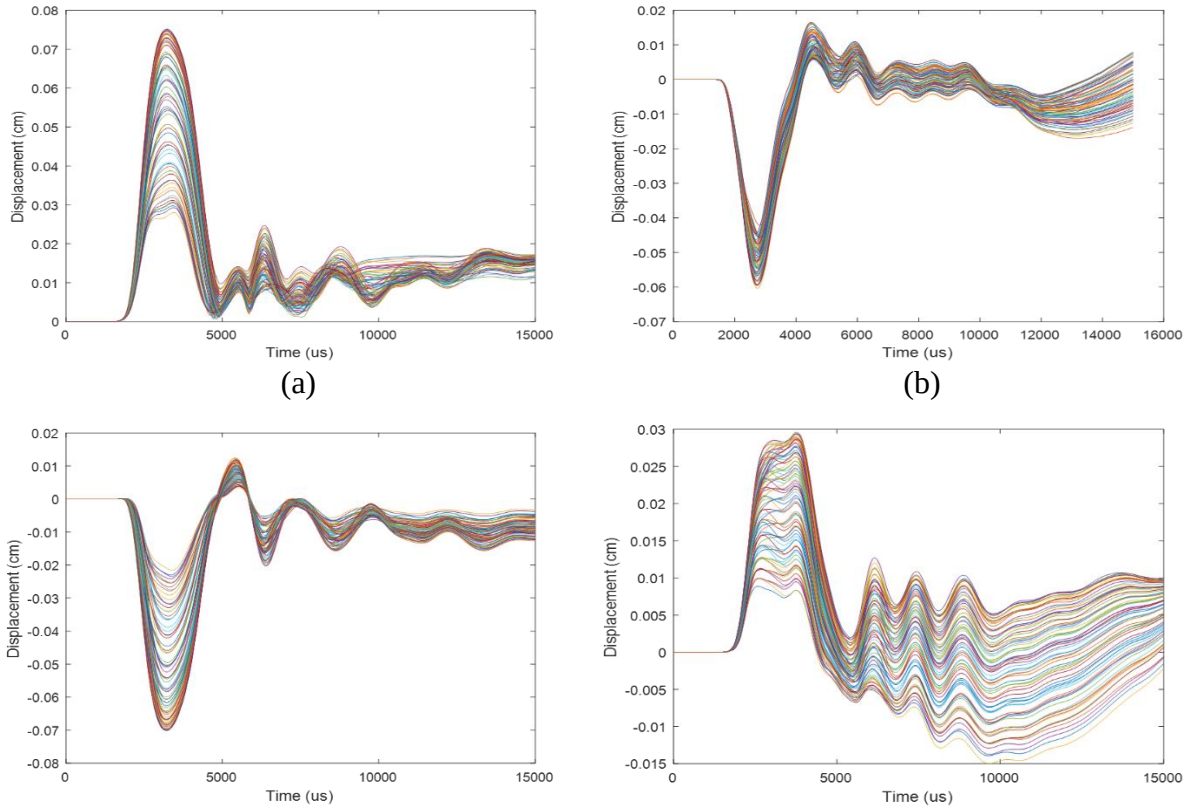

Figure 4-3: (a) Total relative displacement of nodes near the corpus callosum for 90° impact angle. (b) Relative displacement for 90° impact angle in coronal direction. (c) Relative displacement for 90° impact angle in the sagittal direction. (d) Relative displacement for 90° impact angle in the axial direction.

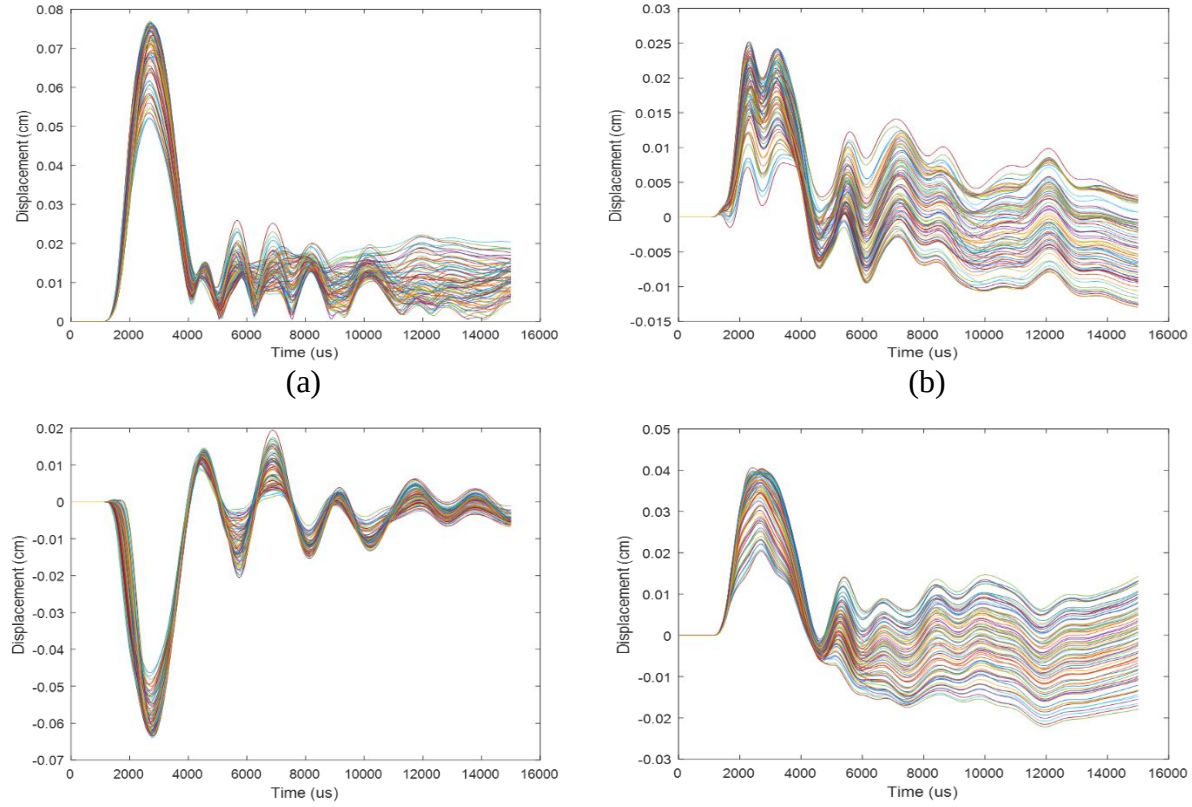

Figure 4-4: (a) Total relative displacement of nodes near the corpus callosum for 135° impact angle. (b) Relative displacement for 135° impact angle in coronal direction. (c) Relative displacement for 135° impact angle in the sagittal direction. (d) Relative displacement for 135° impact angle in the axial direction.

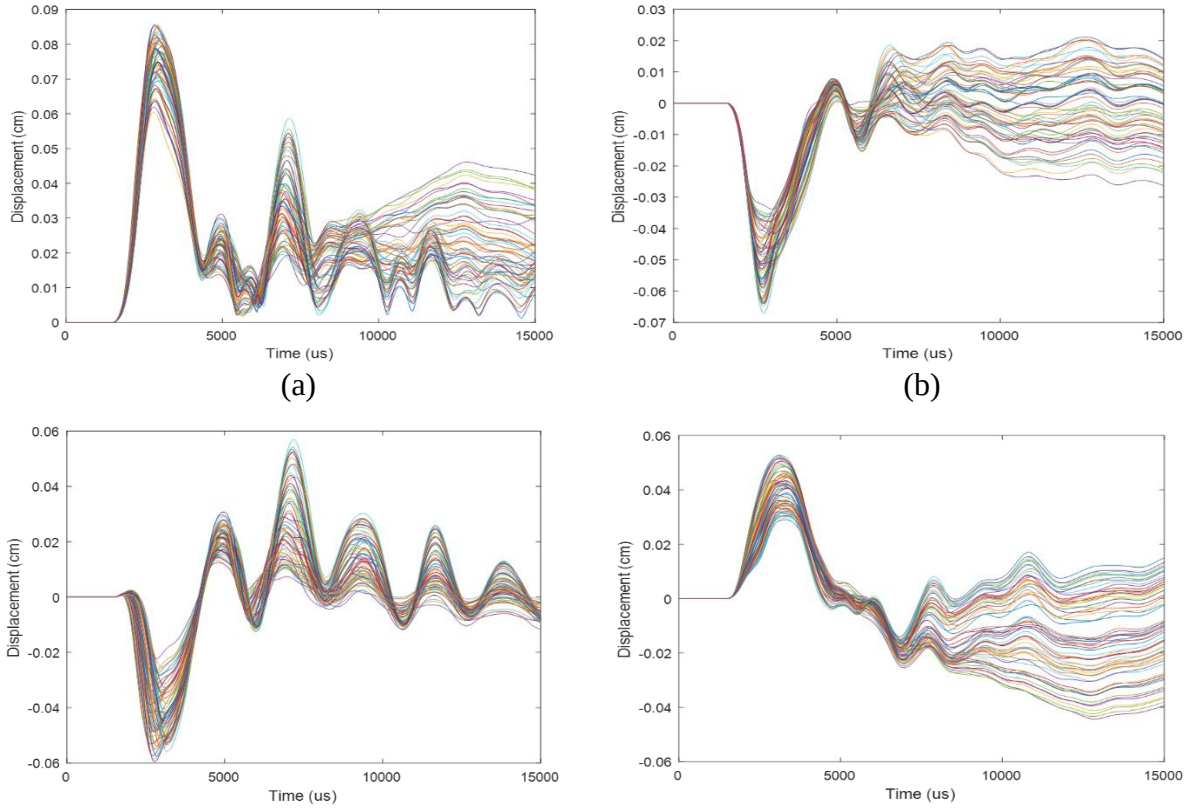

Figure 4-5: (a) Total relative displacement of nodes near the corpus callosum for 180° impact angle. (b) Relative displacement for 180° impact angle in coronal direction. (c) Relative displacement for 180° impact angle in the sagittal direction. (d) Relative displacement for 180° impact angle in the axial direction.

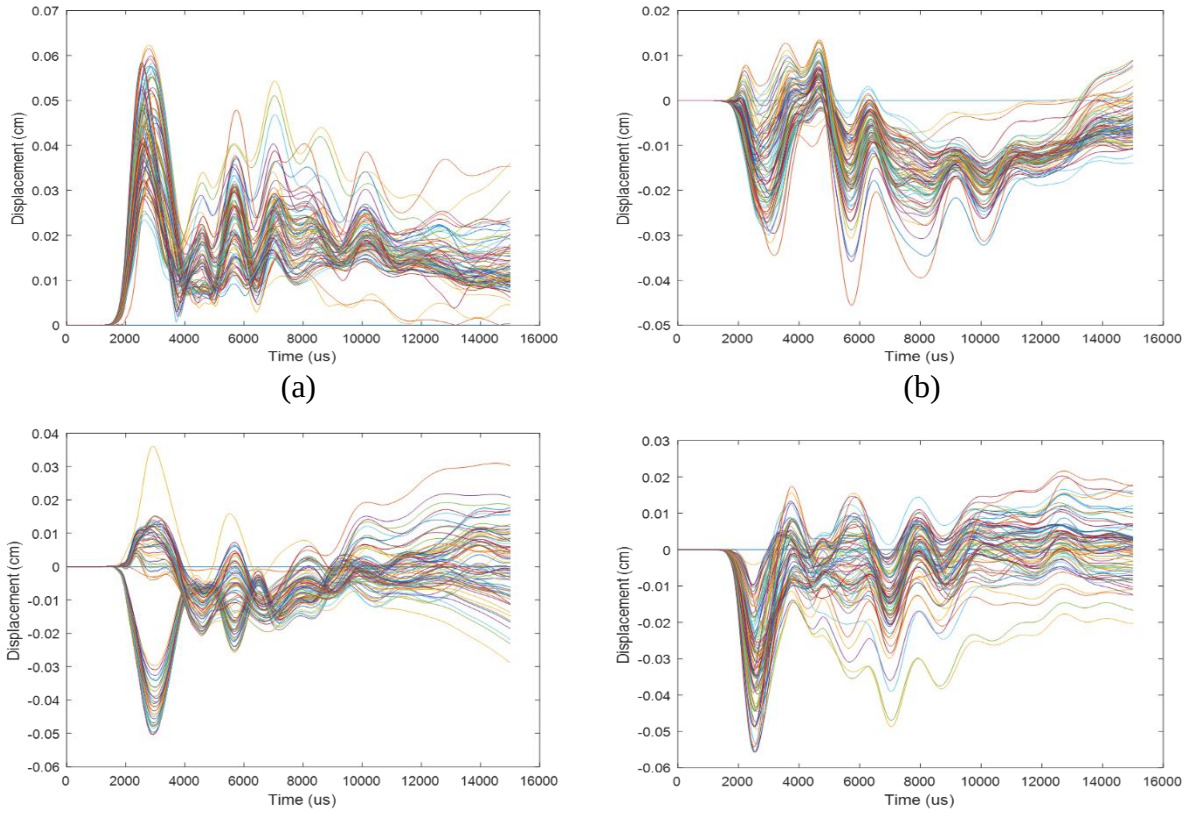

Figure 4-6: (a) Total relative displacement of nodes near the brain stem for 0° impact angle. (b) Relative displacement for 0° impact angle in coronal direction. (c) Relative displacement for 0° impact angle in the sagittal direction. (d) Relative displacement for 0° impact angle in the axial direction.

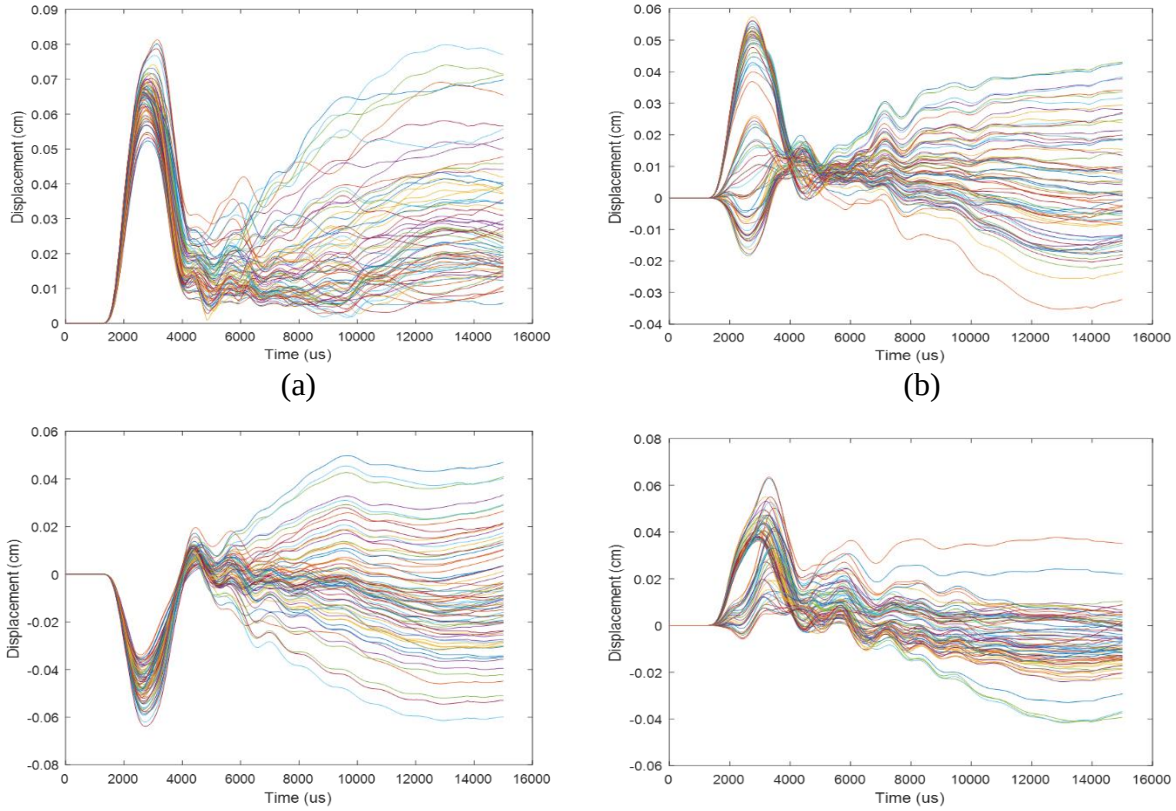

Figure 4-7: (a) Total relative displacement of nodes near the brain stem for 45° impact angle. (b) Relative displacement for 45° impact angle in coronal direction. (c) Relative displacement for 45° impact angle in the sagittal direction. (d) Relative displacement for 45° impact angle in the axial direction.

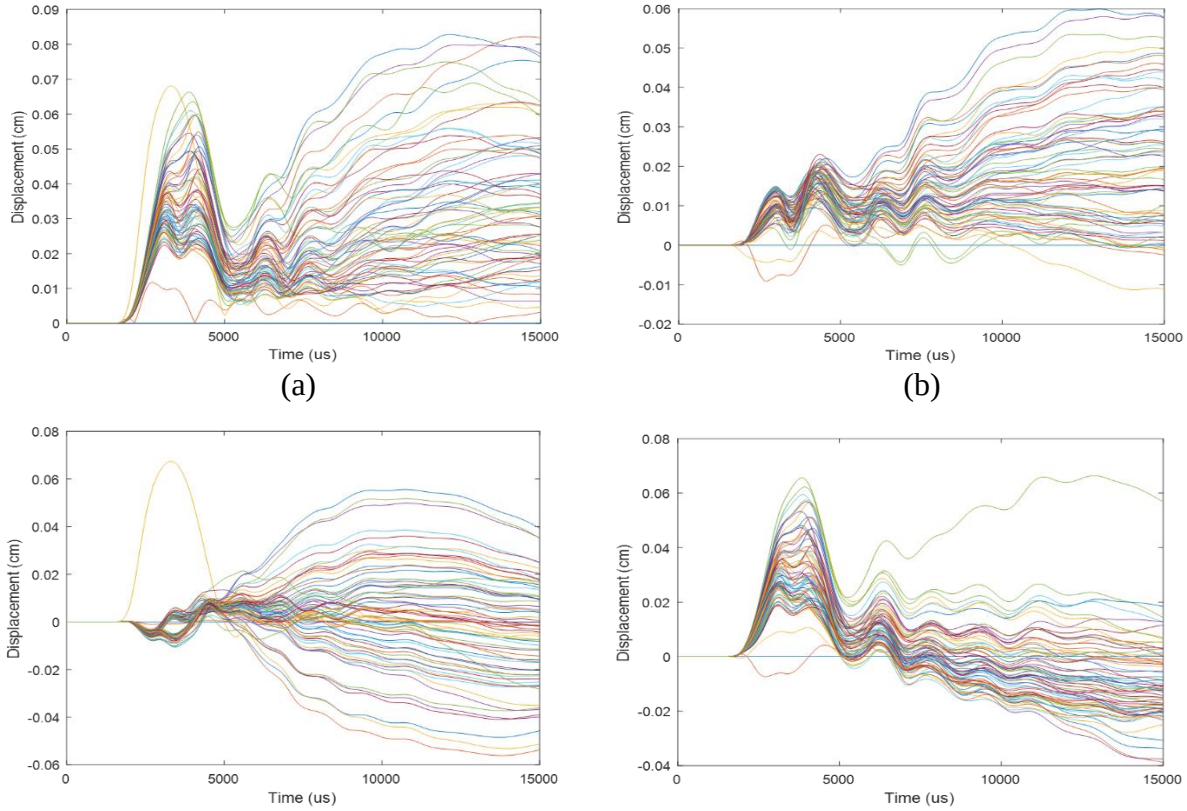

Figure 4-8: (a) Total relative displacement of nodes near the brain stem for 90° impact angle. (b) Relative displacement for 90° impact angle in coronal direction. (c) Relative displacement for 90° impact angle in the sagittal direction. (d) Relative displacement for 90° impact angle in the axial direction.

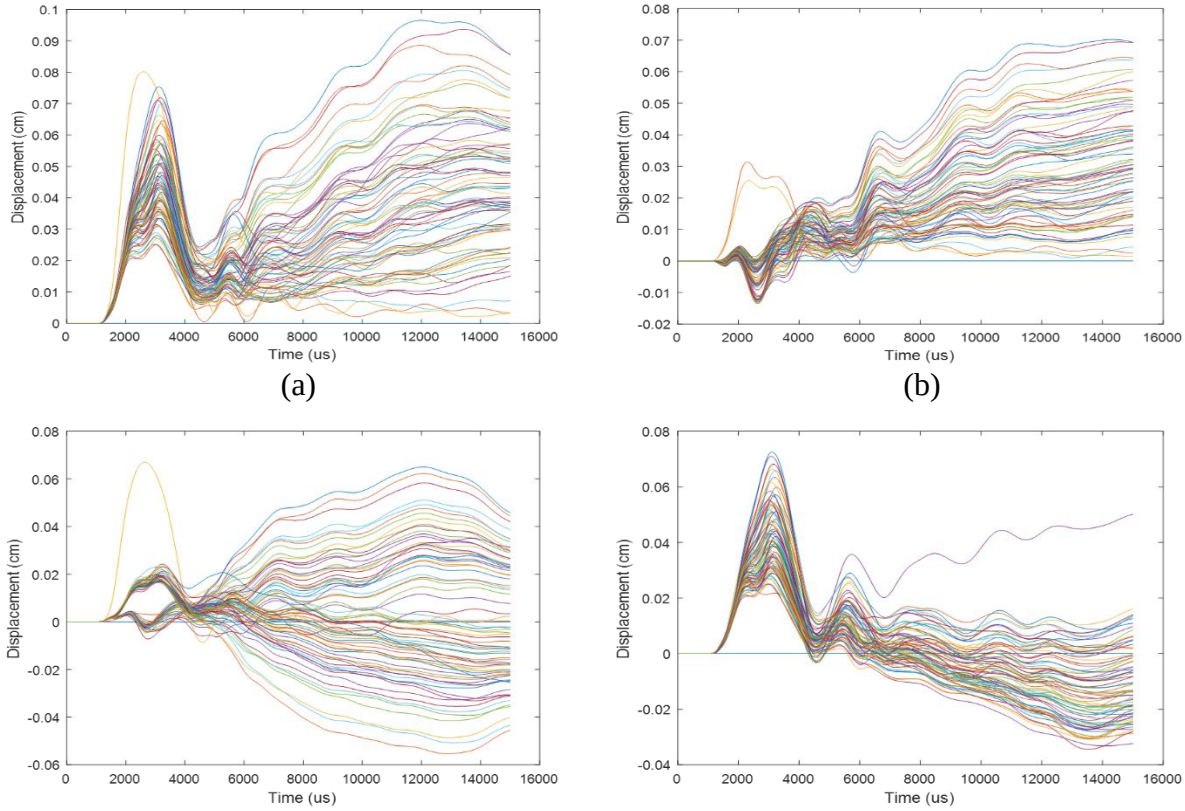

Figure 4-9: (a) Total relative displacement of nodes near the brain stem for 135° impact angle. (b) Relative displacement for 135° impact angle in coronal direction. (c) Relative displacement for 135° impact angle in the sagittal direction. (d) Relative displacement for 135° impact angle in the axial direction.

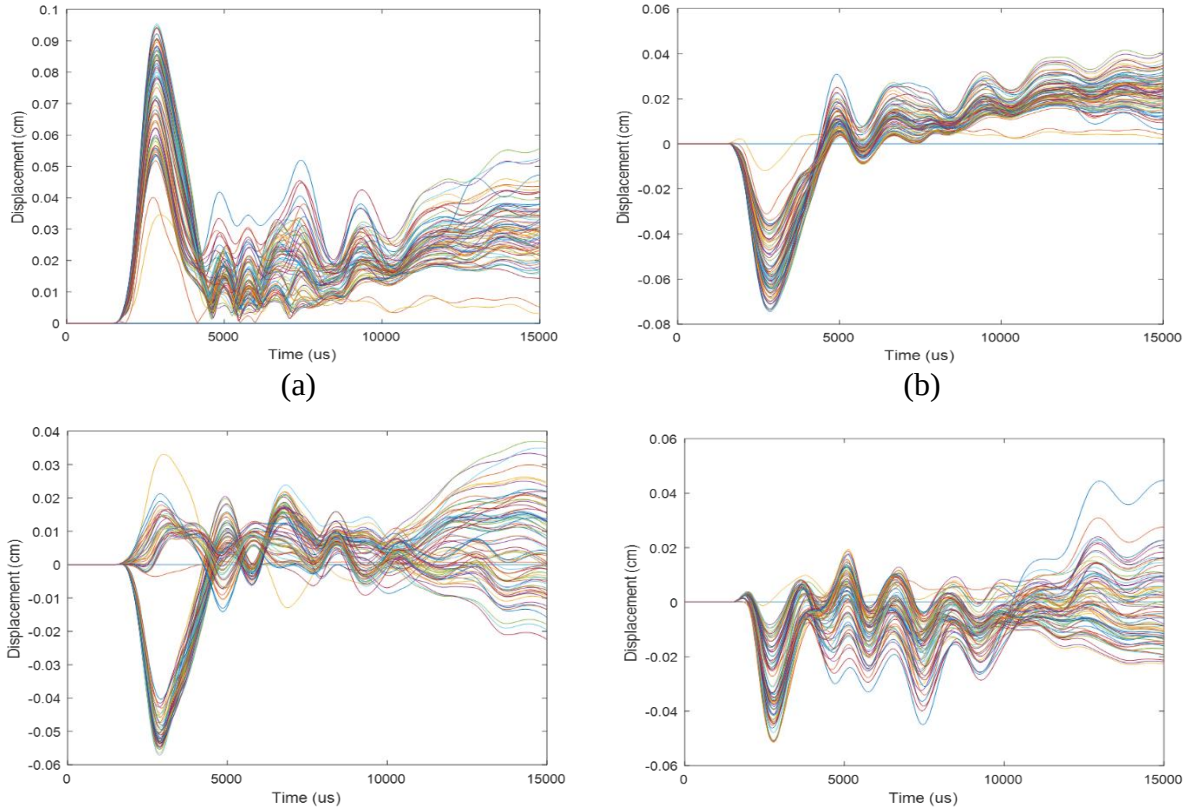

Figure 4-10: (a) Total relative displacement of nodes near the brain stem for 180° impact angle. (b) Relative displacement for 180° impact angle in coronal direction. (c) Relative displacement for 180° impact angle in the sagittal direction. (d) Relative displacement for 180° impact angle in the axial direction.

Each impact angle shows some level of sinusoidal behavior, but it varies across impact angles and displacement directions. Even though the rigid body motion of the skull was subtracted from the total displacement, the coronal and axial directions still show some remnants of rigid body motion. The sagittal direction shows the best sinusoidal behavior because it has the least amount of rigid body motion and a majority of the displacement is due purely to vibration. Additionally, the nodes near the brain stem show poor sinusoidal behavior because of the rigid support boundary condition applied to the bottom surface of the neck. This boundary condition prevents the spine from moving in the inferior axial direction. This causes the spine to push on

the brain stem in the superior axial direction and introduces additional rigid body motion that is not accounted for by the motion of the skull.

4.2. Data Truncation

Next, the truncation point of the system was determined by looking at the diagonal values of the singular matrix determined from SVD. The trace of this singular matrix represents the total variance of the mathematical system and mathematical variance can be equated to the physical energy of the system. Thus, dividing each diagonal element of the singular matrix by its trace determines the percent of energy contribution for each mode. Using the total displacements of nodes near the corpus callosum and brain stem, the variances for each impact angle are plotted in Figures 4-11 & 4-12. From the plots, each impact angle shows a dominant mode accounting for about 70-80% of the variance of the system. Also, each impact angle, nearly all the energy of the system is consumed within the first 6 modes. Thus, the systems were truncated to only consider 6 modes. This correlates to 3 physical modes because as discussed before, the modes are complex conjugate pairs. This truncation significantly reduces the computational cost while still accurately describing the system.

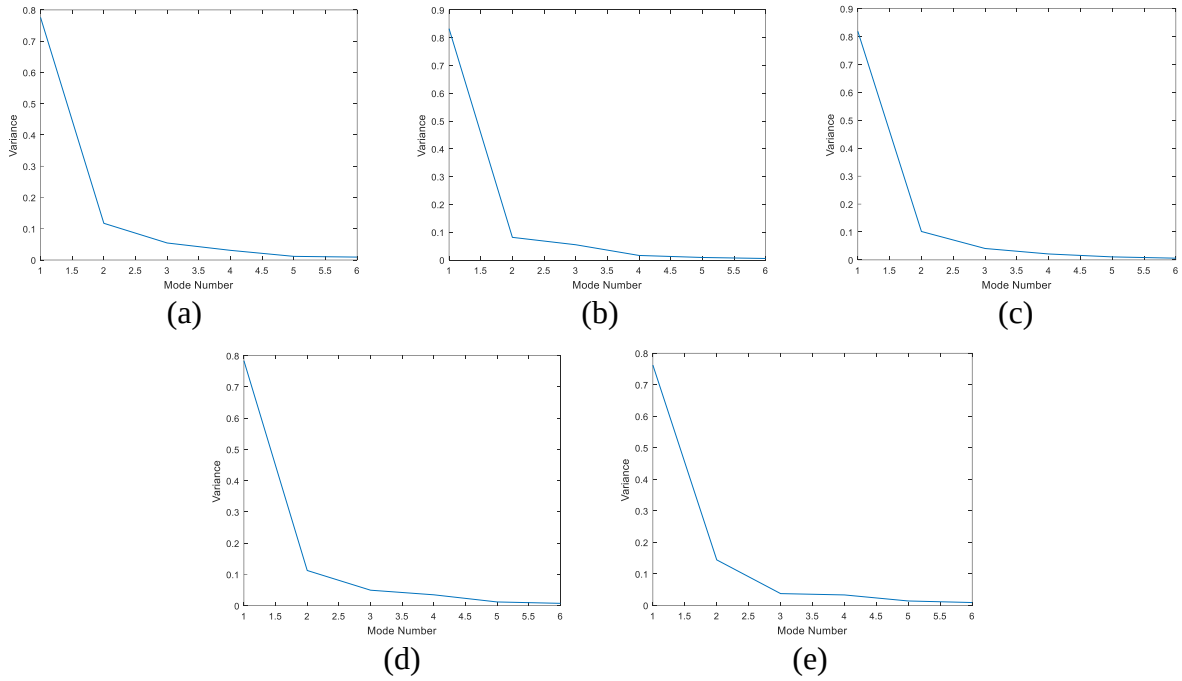

Figure 4-11: (a) Variance of nodes near corpus callosum for 0° impact angle. (b) Variance of nodes near corpus callosum for 45° impact angle. (c) Variance of nodes near corpus callosum for 90° impact angle. (d) Variance of nodes near corpus callosum for 135° impact angle. (e) Variance of nodes near corpus callosum for 180° impact angle.

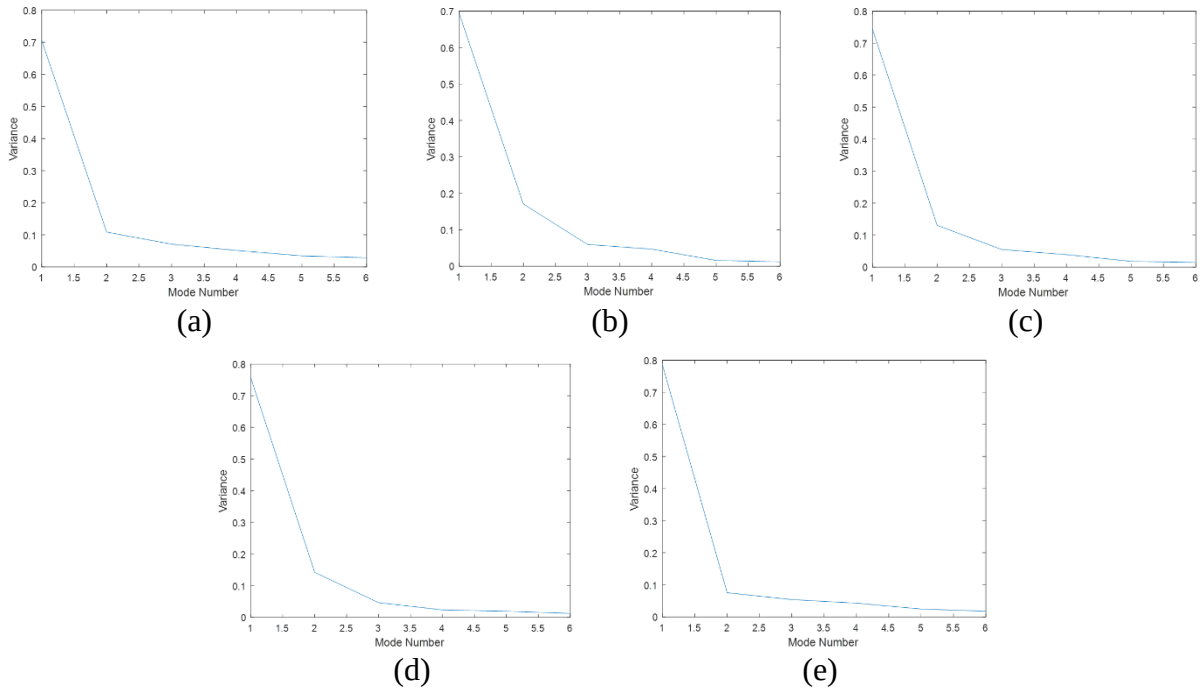

Figure 4-12: (a) Variance of nodes near brain stem for 0° impact angle. (b) Variance of nodes near brain stem for 45° impact angle. (c) Variance of nodes near brain stem for 90° impact angle. (d) Variance of nodes near brain stem for 135° impact angle. (e) Variance of nodes near brain stem for 180° impact angle.

4.3. Modal Frequencies

Once the system is truncated, the modal frequencies, modal amplitudes, and decay rates can be determined for each impact angle. Figures (4-13) - (4-16) & (4-17) - (4-20) compare the first 3 modal frequencies for nodes near the corpus callosum and the brain stem, respectively. The modes are ordered with lowest modal frequency correlating to Mode 1 and the highest modal frequency correlating to Mode 3. The modal frequencies for total displacement and displacement in the sagittal, coronal, and axial directions are compared for each of the 5 impact angles.

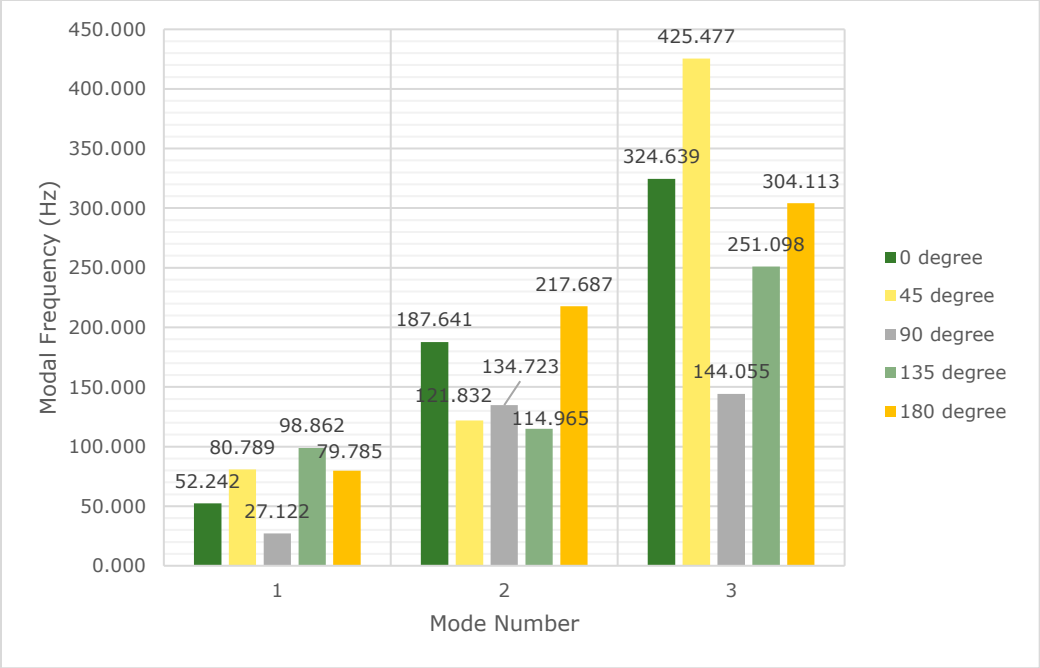

Figure 4-13: Modal frequencies for total displacement of nodes near the corpus callosum.

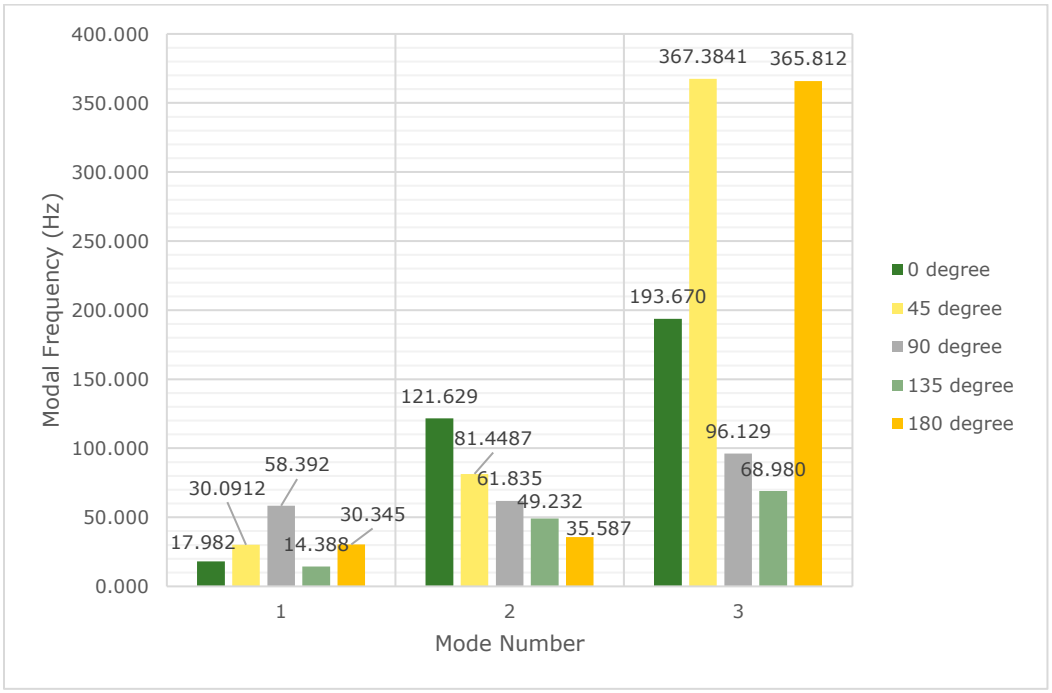

Figure 4-14: Modal frequencies for displacement in the coronal direction of nodes near the corpus callosum.

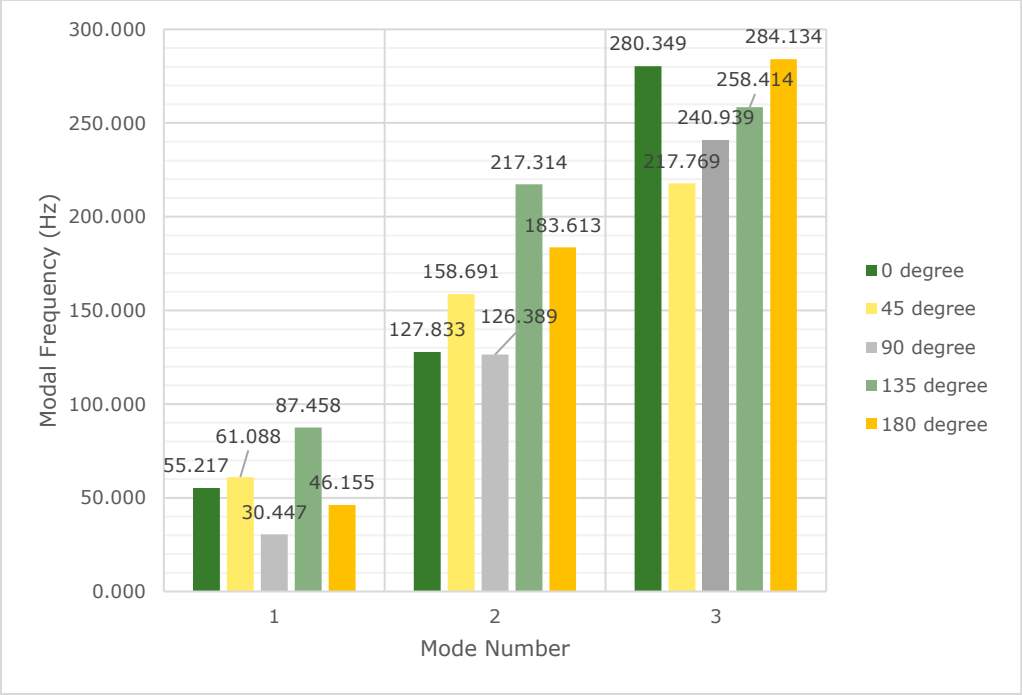

Figure 4-15: Modal frequencies for displacement in the sagittal direction of nodes near the corpus callosum.

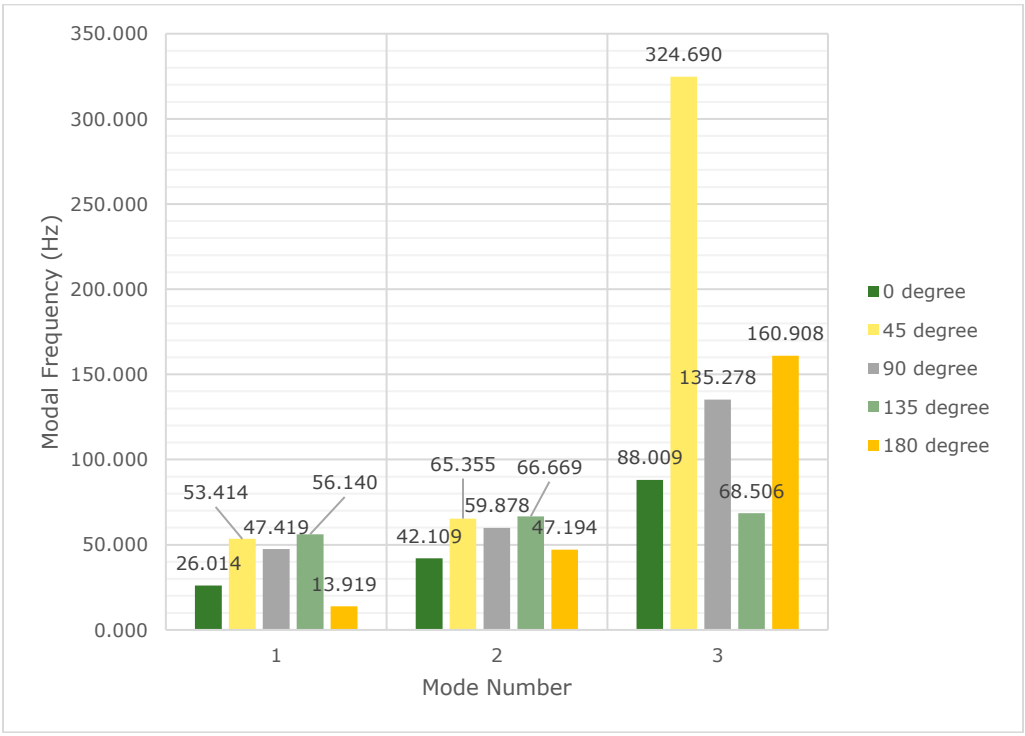

Figure 4-16: Modal frequencies for displacement in the axial direction of nodes near the corpus callosum.

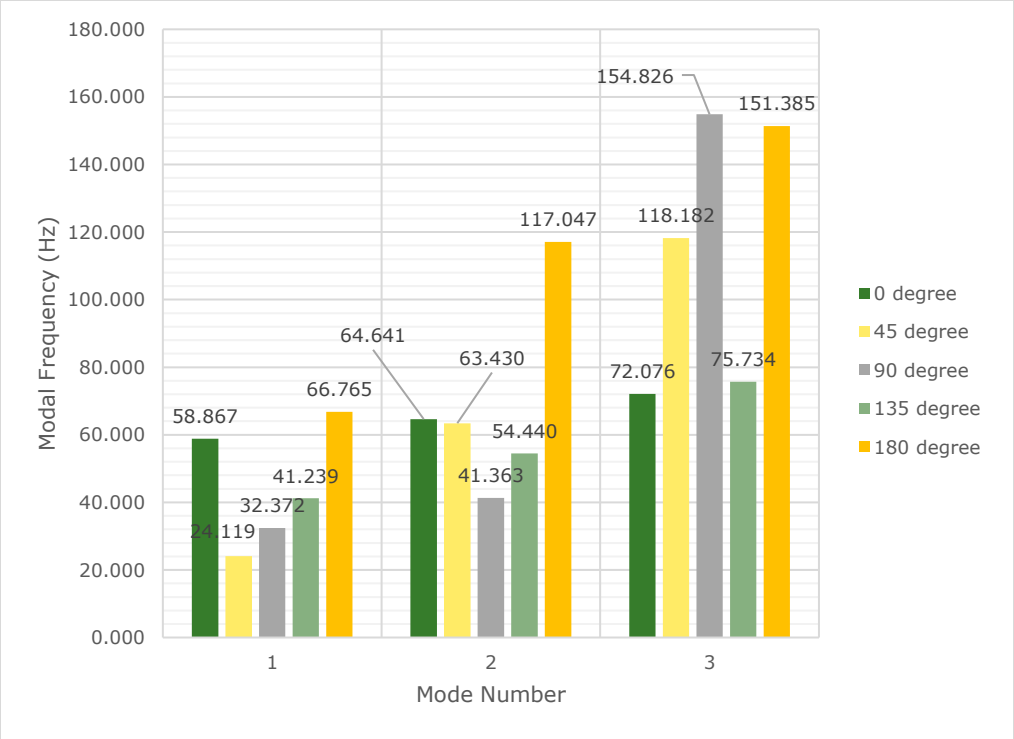

Figure 4-17: Modal frequencies for total displacement of nodes near the brain stem.

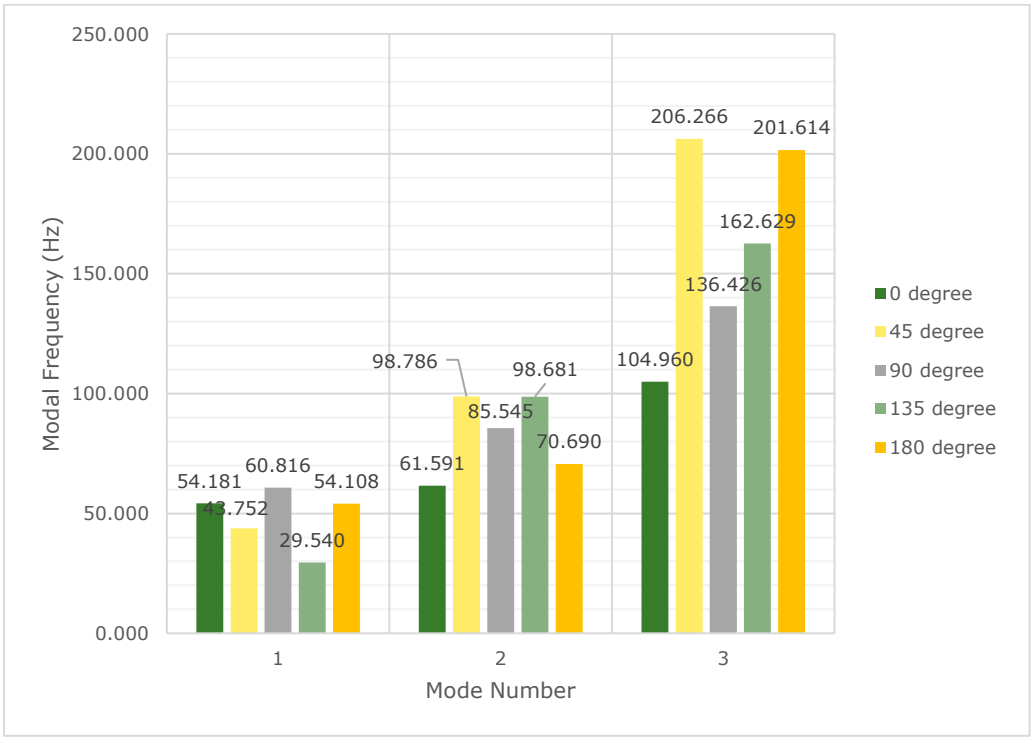

Figure 4-18: Modal frequencies for displacement in the coronal direction of nodes near the brain stem.

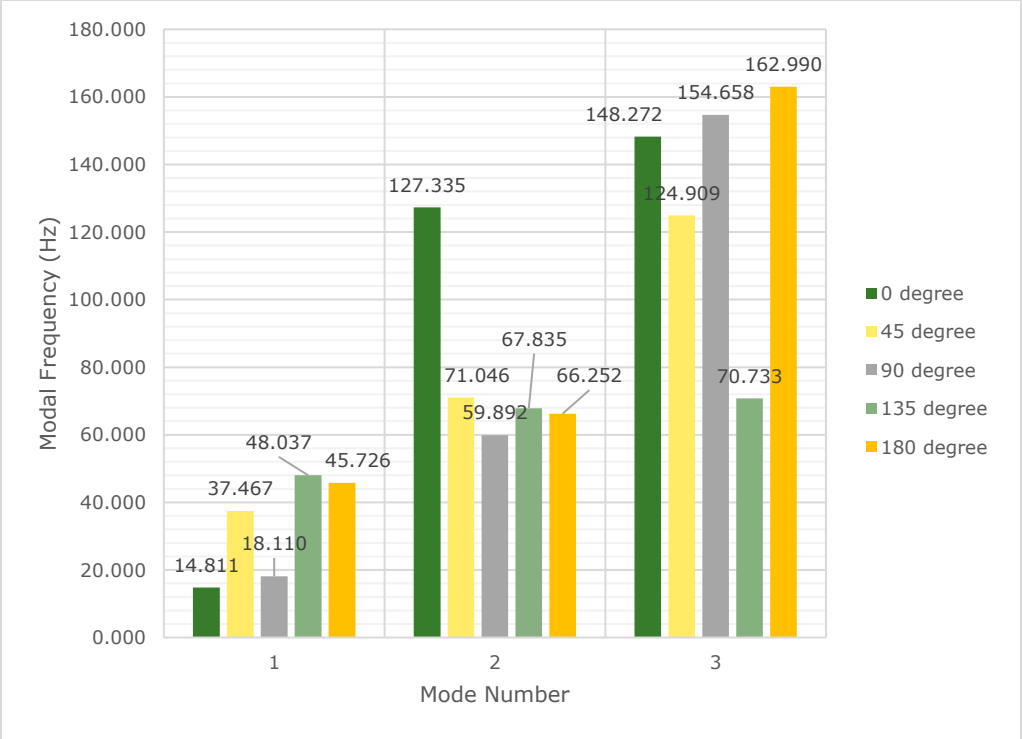

Figure 4-19: Modal frequencies for displacement in the sagittal direction of nodes near the brain stem.

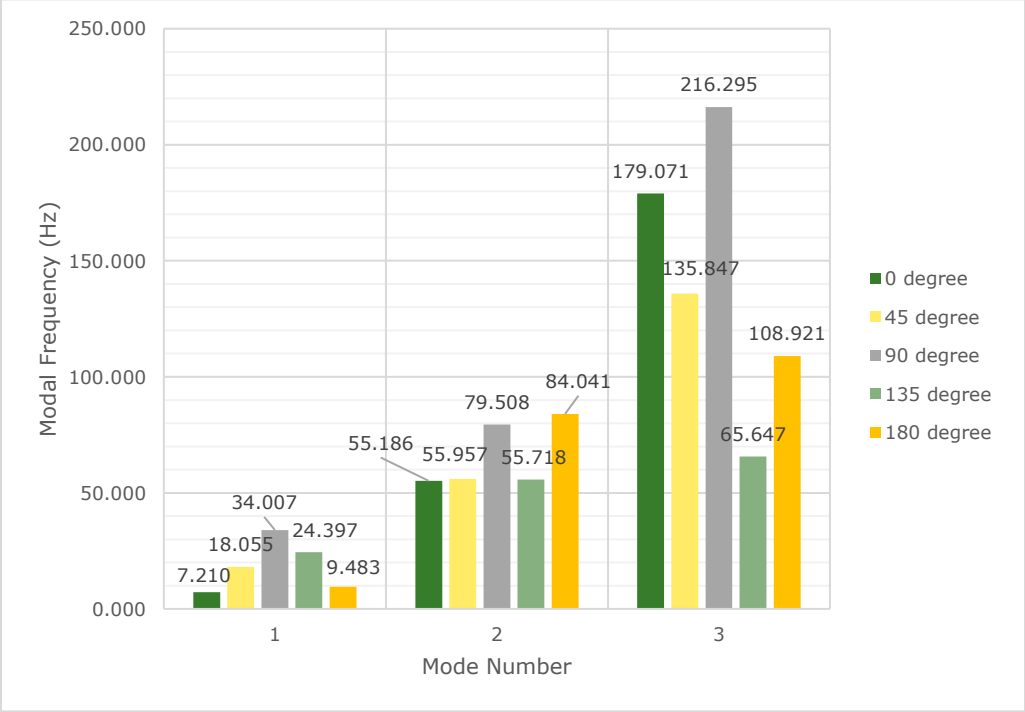

Figure 4-20: Modal frequencies for displacement in the axial direction of nodes near the brain stem.

First, one can see from the graphs that for each location and displacement direction, modal frequencies vary across impact angles. However, even though frequencies vary, each impact angle tends to show three distinct modal frequencies. Additionally, modal frequencies seem to show some level of mirroring over the coronal plane. In other words, the 45° impact angle shows similar modal frequencies compared to the 135° impact angle and the 0° impact angle shows similar modal frequencies compared to the 180° impact angle. The modal frequencies are not identical, but this makes sense because even though the angles are perfectly mirrored over the coronal plane, the head and neck are not. So, the geometry and material constituents at the impact location are very different. Also, the impact location relative to the neck boundary condition is also different which would have a substantial effect on displacement characteristics. So intuitively, this pattern and relationship make sense. Next, for nodes near the corpus callosum, modal frequencies for the sagittal direction show the most distinction between the three modal frequencies. As discussed earlier, the displacement in the sagittal direction showed the best sinusoidal behavior. This improved sinusoidal behavior would suggest that DMD would be able to more accurately differentiate and extract the distinct dynamic modes of vibration. Displacement in the coronal direction also supports this claim because Mode 3 frequencies for the 0° and 180° impact angles show abnormally high modal frequencies. These impact angles would generate the most rigid body motion in the coronal direction and thus would reduce the accuracy of DMD. To better understand these patterns and relationships, Tables 4-1 & 4-2 present the average modal frequencies across the 5 impact angles in each displacement direction for nodes near the corpus callosum and brain stem, respectively. It also provides the coefficient of variance for each mode and displacement direction. The coefficient of variance (CV) is the standard deviation of a mode divided by its average modal frequency. Since, Mode 3

is much higher than Mode 1 it will inherently have a higher standard deviation. The CV eliminates this effect by dividing by the average modal frequency; thus, providing a better comparison between the three modes.

Table 4-1: Average modal frequencies across impact angles and their respective coefficients of variance for nodes near the corpus callosum.

	Average Modal Frequency (Hz)				Coefficient of Variance			
	Total Displacement	**Coronal**	**Sagittal**	**Axial**	**Total Displacement**	**Coronal**	**Sagittal**	**Axial**
Mode 1	67.760	30.240	56.073	39.381	0.415	0.571	0.374	0.469
Mode 2	155.370	69.946	162.768	56.241	0.289	0.478	0.237	0.196
Mode 3	289.876	218.395	256.321	155.478	0.355	0.654	0.108	0.652

Table 4-2: Average modal frequencies across impact angles and their respective coefficients of variance for nodes near the brain stem.

	Average Modal Frequency (Hz)				Coefficient of Variance			
	Total Displacement	**Coronal**	**Sagittal**	**Axial**	**Total Displacement**	**Coronal**	**Sagittal**	**Axial**
Mode 1	44.672	48.479	32.830	18.630	0.399	0.252	0.471	0.590
Mode 2	68.184	83.059	78.472	66.082	0.423	0.200	0.351	0.218
Mode 3	114.441	162.379	132.312	141.156	0.346	0.265	0.281	0.416

For nodes near the corpus callosum, the sagittal direction shows the lowest CV across all three modes, especially Mode 3. This statistically supports what was seen visually in the bar graphs above. In general, the CV values are high. CV value standards vary greatly depending on the data application, but typically the upper extreme is 0.30. Since the modal frequencies are averaged across the different impact angles, the CV represents the variance between different impact angles. The high CV values suggest that the impact angle has a substantial effect on the modal frequencies experienced by the brain during impact. This presents a complicated problem from an engineering standpoint because it means the different impact angles will have to be

considered separately and any safety designs would have to be able to cover a large range of frequencies rather than a smaller frequency range common to several impact angles. To understand the effects of displacement direction, modal frequencies were averaged across displacement direction for each impact angle. Tables 4-3 & 4-4 summarize the average modal frequencies and CVs for nodes near the corpus callosum and brain stem, respectively. Again, CV values are greater than 0.30 for nearly all impact angles in both locations. In fact, the CV values for modal frequencies averaged across displacement directions are higher than those for modal frequencies averaged across impact angles. This shows that the choice displacement direction has an even greater effect on the determined modal frequencies. The choice of displacement direction does not change the loading or displacement of the system but is rather a choice of data selection. The success of any numerical technique is limited by the selection and quality of data. Without the accurate and quality displacement data, DMD is limited in its capabilities to identify modal characteristics of an impact event. Intuitively, the total displacement seems to be the appropriate choice, but this study does not provide any statistical data to determine the appropriate displacement direction.

Table 4-3: Average modal frequencies across displacement directions and their respective coefficients of variance for nodes near the corpus callosum.

	Average Modal Frequency (Hz)					Coefficient of Variance				
	0°	**45°**	**90°**	**135°**	**180°**	**0°**	**45°**	**90°**	**135°**	**180°**
Mode 1	37.864	56.345	40.845	64.212	42.551	0.492	0.371	0.359	0.588	0.66
Mode 2	119.803	106.832	95.706	112.045	121.020	0.498	0.392	0.422	0.673	0.769
Mode 3	221.666	333.830	154.100	161.750	278.742	0.470	0.262	0.399	0.664	0.308

Table 4-4: Average modal frequencies across displacement directions and their respective coefficients of variance for nodes near the brain stem.

	Average Modal Frequency (Hz)					Coefficient of Variance				
	0°	**45°**	**90°**	**135°**	**180°**	**0°**	**45°**	**90°**	**135°**	**180°**
Mode 1	33.767	30.848	36.326	35.803	44.020	0.785	0.383	0.490	0.301	0.558
Mode 2	77.188	72.304	66.577	69.168	84.507	0.436	0.258	0.301	0.297	0.271
Mode 3	126.095	146.301	165.551	93.686	156.228	0.373	0.277	0.210	0.492	0.244

Next, the modal frequencies were compared regionally. Using each displacement direction, modal frequencies for each impact angle were compared between nodes near the corpus callosum and brain stem. To eliminate the variance of impact angles and displacement directions, the modal frequencies were not averaged in any way. There are only two regions to compare so there is not significant data for statistical comparison. Instead, the modal frequencies were compared to one another using bar graphs. The modal frequency comparisons for total displacement are shown in Figures (4-21) - (4-23). Comparisons for the remaining displacement directions can be found in the Appendix.

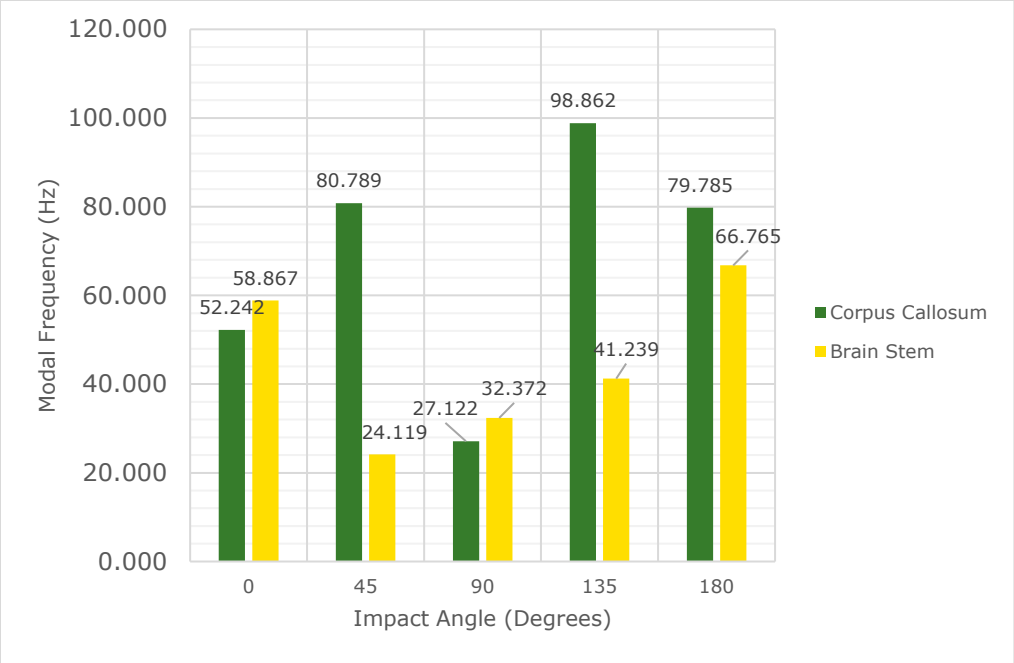

Figure 4-21: Comparison of Mode 1 modal frequencies for each impact angle using total displacement of nodes near the corpus callosum and brain stem.

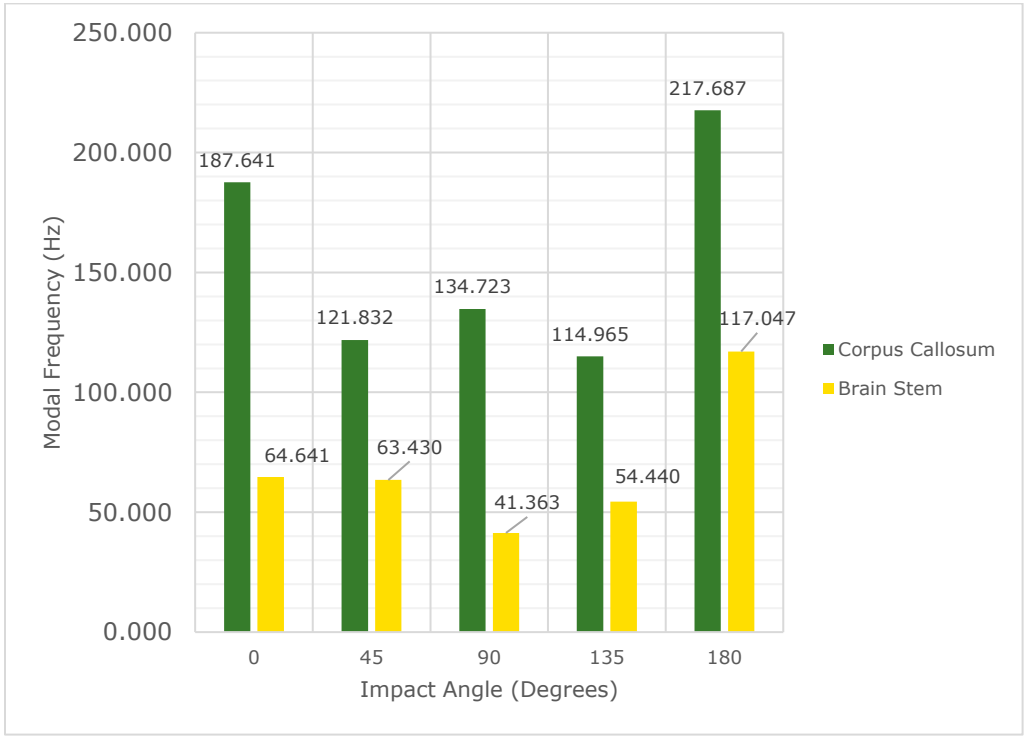

Figure 4-22: Comparison of Mode 2 modal frequencies for each impact angle using total displacement of nodes near the corpus callosum and brain stem.

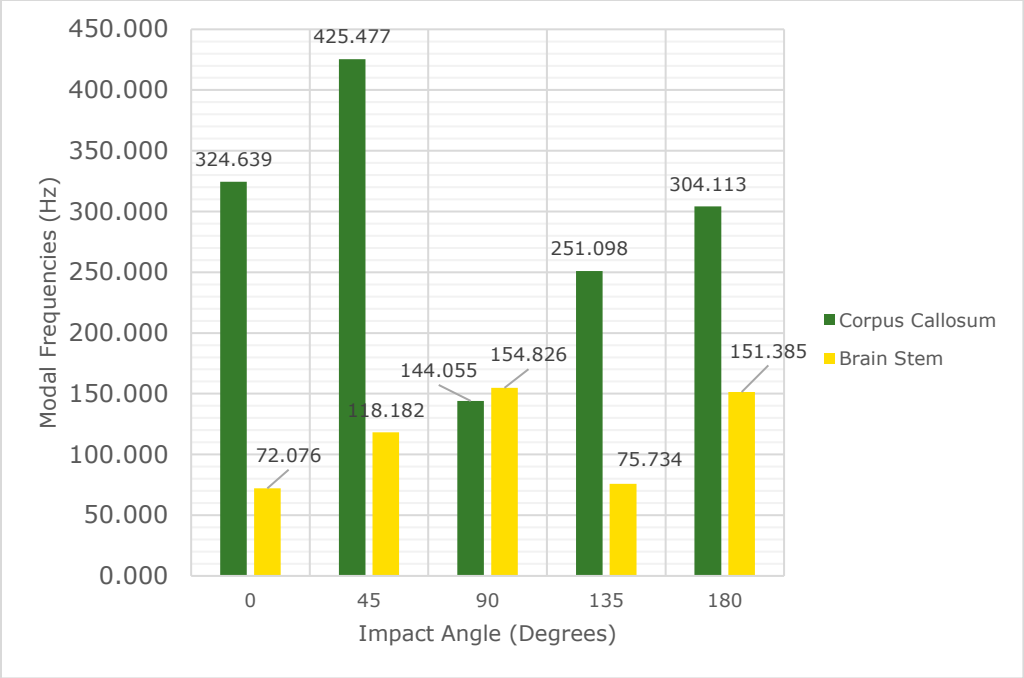

Figure 4-23: Comparison of Mode 3 modal frequencies for each impact angle using total displacement of nodes near the corpus callosum and brain stem.

From the figures, the modal frequencies experienced by the brain near the corpus callosum are very different from those experienced near the brain stem. Except for two impact angles for Mode 1 and one impact angle for Mode 3, the corpus callosum modal frequencies are much higher for each impact angle. A possible reason for this could be the interaction between the brain stem and spine. It has a profound impact on displacement and could potentially shift modal frequencies. This data shows that location has a considerable effect on the modal frequencies experienced during impact.

4.4. Modal Amplitudes and Decay Rates

In addition to frequencies, the modal amplitudes and decay rates were determined for each impact angle, location, and mode. DMD determines the modal amplitude for each node but does not determine a singular representative value for comparison. Within literature there is no consensus on the correct way to compare the magnitude of modes, but two common methods are to simply average modal amplitudes for each node or take the L_2-norm. This study chose to take

the L_2-norm for each set of nodal displacements. The magnitude of Modes 1, 2, and 3 were normalized for each loading case and displacement direction by dividing the L_2-norm of each mode by the maximum L_2 -norm value. The decay rates were determined using the imaginary part of Equation 2.27. The normalized modal amplitudes and decay rates for total displacement of nodes near the corpus callosum are shown for each impact angle in Tables (4-5) – (4-9). The remaining displacement directions are tabulated in the Appendix.

Table 4-5: Modal frequency, amplitude, and decay rates for nodes near the corpus callosum and 0° impact angle. Modal amplitudes were normalized by the maximum modal amplitude to provide a quality comparison.

Modal Frequency (Hz)	Normalized Modal Amplitude	Decay Rate (Hz)
52.242	1.000	94.535
187.641	0.985	1334.842
324.639	0.811	697.619

Table 4-6: Modal frequency, amplitude, and decay rates for nodes near the corpus callosum and 45° impact angle. Modal amplitudes were normalized by the maximum modal amplitude to provide a quality comparison.

Modal Frequency (Hz)	Normalized Modal Amplitude	Decay Rate (Hz)
80.789	0.989	337.736
121.832	1.000	0.000
425.477	0.953	3026.153

Table 4-7: Modal frequency, amplitude, and decay rates for nodes near the corpus callosum and 90° impact angle. Modal amplitudes were normalized by the maximum modal amplitude to provide a quality comparison.

Modal Frequency (Hz)	Normalized Modal Amplitude	Decay Rate (Hz)
27.122	1.000	84.112
134.723	0.993	1400.362
144.055	0.971	483.238

Table 4-8: Modal frequency, amplitude, and decay rates for nodes near the corpus callosum and 135° impact angle. Modal amplitudes were normalized by the maximum modal amplitude to provide a quality comparison.

Modal Frequency (Hz)	Normalized Modal Amplitude	Decay Rate (Hz)
98.862	1.000	0.000
114.965	0.982	713.222
251.098	0.974	1571.536

Table 4-9: Modal frequency, amplitude, and decay rates for nodes near the corpus callosum and 180° impact angle. Modal amplitudes were normalized by the maximum modal amplitude to provide a quality comparison.

Modal Frequency (Hz)	Normalized Modal Amplitude	Decay Rate (Hz)
79.785	1.000	0.000
217.687	0.983	756.033
304.113	0.977	774.457

Overall, the DMD code did not identify dominant modes of vibrations for different impact angles. All the normalized modal amplitudes are close to 1, which means comparatively, the modes represent an equal contribution to the total displacement and the vibrational characteristics of the brain. This makes it nearly impossible to identify a sensitive frequency range for the brain. It is clear that there are 3 distinct modes of vibration, but it is impossible to tell whether Mode 1, 2, or 3 is the dominant mode of vibration. This makes it hard to design a helmet or safety device that protects the brain from resonance because one cannot tell what

frequency range to suppress. Additionally, the decay rates determined by the DMD code are very high and in some cases zero. The very high decay rates indicate very high damping and a short duration of vibration. This contrasts what is widely believed in literature, that vibration in the brain lasts for a significant amount of time, upwards of 100 ms. A decay rate of zero represents a quasi-static wave that does not decrease in amplitude and continues to propagate infinitely. This is a physically impossible phenomenon and is an erroneous solution. This study believes there are three possible reasons for the lack of dominant modes and the presence of high and erroneous decay rates. First, due to computing capability and storage, the simulation time of the system was only 15ms. In the displacement plots, one can see that the vibrations have not dissipated completely in the allotted simulation time. Thus, the entire impact event is not fully observed, and the full dampening effect and decay rate is not described. Secondly, some remnants of rigid body motion were seen in the displacement plots. Particularly, displacements in the coronal and sagittal directions. This rigid body motion dominates the vibrational displacement and interferes with the sinusoidal behavior of the displacements. It also creates increased nodal displacements that could result in the inability to differentiate between the modal amplitudes of separate modes. Improved methods would need to be developed to remove the remnant rigid body motion to obtain displacements purely due to vibration.

The DMD code implemented in this study was able to determine numerical values for the mode shapes of each mode and how they decayed overtime. Unfortunately, due to technological limitations, the numerical values were not applied to form the 3-D mode shapes. The modal displacements for each direction need to be reentered back into the FEA model with the correct node and spatial arrangement. Otherwise, the mode shapes have no physical meaning or correlation to the brain and simply represent a collection of random displacements.

4.5. Comparison of Results to Laksari

Although there were significant differences in methodology, in comparison to the similar work done by Laksari et al., this study provided very different results. First, the modal frequencies identified in this study were higher. As discussed earlier, Laksari et al. identified a dominant modal frequency around 20-40 Hz. For different displacement directions Mode 1 frequencies ranged from 30.240- 67.600 Hz for nodes near the corpus callosum and from 18.630-48.479 Hz for nodes near the brain stem. These are very comparable to the frequencies determined by Laksari et al., but Mode 2 and Mode 3 produced much higher frequencies. With the inability of this study to successfully differentiate between modal amplitudes, it is impossible to determine whether Mode 1, 2, or 3 is the dominant mode of vibration. This makes it difficult to establish a quality comparison of dominant modal frequencies between this study and the work of Laksari et al. Furthermore, the decay rates determined in this study were significantly higher than those determined by Laksari et al. This study determined decay rates in the range of hundreds and sometimes thousands of Hz. Laksari et al. determined decay rates on the order of 18-29 Hz. These low decay rates suggest that impact to the brain is a relatively long temporal event. There are a few possible reasons for the substantial differences in results between the two studies. First, most of the loading implemented by Laksari et al. was rotational while the loading applied in this study was primarily linear. This study expected to observe different results because of the loading applied but not quite to the level that was observed. Instead, this study primarily believes the differences are due to data collection. As discussed earlier, computational capabilities limited the simulation time of this study to 15 ms. Laksari et al. used a 100 ms simulation time and were able to capture the entire transient event. In the span of their simulation time they were able to observe the vibrational displacement completely attenuate and return to

zero. Additionally, this study only simulated 5 impacts whereas Laksari et al. simulated 187. The additional statistical data provided by more impact events could provide further insight into the vibrational behavior of the brain.

CHAPTER 5. CONLCUSIONS AND RECOMMENDATIONS

5.1. Conclusions

This research aimed to use DMD to better understand the human brain during concussive impact events. Currently, the brain is primarily studied and observed using acceleration and forces but very little is understood about the brain in the frequency domain. As a proof of concept, this study was able to develop a successful DMD code and show some of its capabilities and applications. This study was not able to successfully identify a dominant mode of vibration, but it did show the capability of DMD to extract modal frequencies purely from numerical data without having to define or understand the underlying model. Through SVD and DMD this study identified that vibration in the brain can be described using 3 or less modes of vibration. For each loading case nearly all of the variance of the system is used up within the first 3 modes. The DMD code was also able to determine modal amplitudes, decay rates, and numerical mode shapes. The accuracy and quality of these values were hindered because of data collection and computational limitations but the DMD code itself was successful in its application.

This study also provided insight into the effects of impact angle, displacement direction, and different regions of the brain. The data provided showed that each variable had a significant effect on the modal frequencies and decay rates. Each impact angle resulted in significantly different modal frequencies. For specific modes and displacement angles there was some evidence of slight mirroring over the coronal plane but as an average across all the data, there were no similarities seen between impact angles. Additionally, different displacement directions showed very different modal frequencies. The total displacement fully describes the magnitude of displacement but does not give an indication of direction without the components in the three principle directions. There is no data to suggest which displacement is correct to consider, only

that modal frequencies are very dependent on what displacement is chosen. Modal frequencies also showed substantial differences depending on whether nodes were selected near the corpus callosum or brain stem. The frequencies were lower for nodes near the brain stem and this study believes this is due to the boundary conditions present and the influence of the spine pressing on the brain stem.

Overall, this study showed that this is an important and complex problem. In the engineering industry modal analysis is one of most commonly applied analyses for determining the quality and viability of a product. For that reason, this study believes it is also a very important consideration for TBI and other injury areas. There is an immense amount of space for engineers to better understand the brain in the frequency domain. The improvement in understanding could unlock insight into TBI and help us protect and maintain the health of athletes, soldiers, and citizens worldwide. However, this study has also shown that this is no easy task. DMD is a powerful and effective numerical technique but is highly dependent on the quality and quantity of data used. There is room for improvement in methodology and data collection that could improve results and provide better insight and understanding. This is only the first step, but this study shows the exciting and promising future of DMD and its ability to help us better understand TBI and the human brain.

5.2. Recommendations for Future Work

A majority of possible improvements revolve around improving data collection. The DMD code follows a rigid structure and there is not a much room for adjusting or changing the process. However, its capabilities are a function of the input data and its success is dependent on the quality of data. To improve data quality, this study presents 4 areas for improvement. First, improve computing capabilities. By increasing RAM to the necessary sizes, the simulation time

could be increased, and the full impact event could be observed. Thus, DMD would be better able to describe the vibrational characteristics of displacement. Additionally, an improvement to computing capabilities would include a method to insert mode shapes back into the original model. This would provide physical mode shapes to help better understand what parts of the brain are experiencing the most strain. Secondly, improvements could be made in the human head model. The model used in this study was developed in 2003. Since then, the abilities of computer modeling and FEA have greatly increased and thus there are more recently developed models that could provide improved results. Next, methods for determining the relative displacement could be improved. In other words, determining the displacement purely due to vibration and not rigid body motion. Removing the displacement of the skull helped reduce the effects of rigid body motion but it did not eliminate it. Again, this would help highlight the sinusoidal behavior of vibrational displacement and improve the effectiveness of DMD. Finally, the data could be improved by investigating the effects of sampling rates and possibly looking into noise filtering. This study does not present any specific recommendations but rather a general suggestion. Sampling rate and noise influence nearly every numerical technique, including DMD.

REFERENCES

1. Betts, J. (2017). *Anatomy & Physiology-Rice University OpenStax CNX pp 787-846*.
2. Monro-Kellie Doctrine. (n.d.). Retrieved from http://casemed.case.edu/clerkships/neurology/NeurLrngObjectives/Monroe Kellie.htm
3. Gu, L., Chafi, M. S., Ganpule, S., & Chandra, N. (2012). The influence of heterogeneous meninges on the brain mechanics under primary blast loading. *Composites Part B: Engineering*, *43*(8), 3160–3166. doi: 10.1016/j.compositesb.2012.04.014
4. Tse, K. M., Lim, S. P., Tan, V. B. C., & Lee, H. P. (2014). A review of head injury and finite element head models. American Journal of Engineering, Technology and Society, 1(5), 28-52
5. Bailey, R. (2019, July 2). Brain Anatomy: The Function and Layers of the Meninges. Retrieved from https://www.thoughtco.com/brain-anatomy-meninges-4018883
6. Rhoton, & L., A. (2002, October 1). Cerebrum. Retrieved from https://academic.oup.com/neurosurgery/article/51/suppl_4/S1-1/2727994
7. E. Gurdjian, V. Hodgson, L. Thomas, and L. Patrick, J. Neurosurg. 29, 70 (1968)
8. Brain lobes. (n.d.). Retrieved from https://www.mayoclinic.org/brain-lobes/img-20008887
9. Stuss, D. T., & Knight, R. T. (2013). *Principles of frontal lobe function*. New York: Oxford University Press.
10. Miller, B. L. (2018). *The Human frontal lobes: functions and disorders*. New York, NY: Guilford.
11. Karnath, H. O. (1997). Spatial orientation and the representation of space with parietal lobe lesions. *Philosophical Transactions of the Royal Society of London. Series B: Biological Sciences*, *352*(1360), 1411–1419. doi: 10.1098/rstb.1997.0127

12. Wagner, A. D., Shannon, B. J., Kahn, I., & Buckner, R. L. (2005). Parietal lobe contributions to episodic memory retrieval. *Trends in Cognitive Sciences*, *9*(9), 445–453. doi: 10.1016/j.tics.2005.07.001
13. Guyton, Arthur C.; Hall, John Edward (2005). *Textbook of medical physiology* (11th ed.). Philadelphia: W.B. Saunders. pp. 764–7.
14. Wright, Ben L. C.; Lai, James T. F.; Sinclair, Alexandra J. (26 January 2012). "Cerebrospinal fluid and lumbar puncture: a practical review". *Journal of Neurology*. 259 (8): 1530–1545.
15. Noback, Charles; Norman L. Strominger; Robert J. Demarest; David A. Ruggiero (2005). *The Human Nervous System*. Humana Press. p. 93.
16. Zasler, Nathan D. *Brain Injury Medicine Principles and Practice*. Demos, 2013.
17. “Traumatic Brain Injury in the United States: A Report to Congress.” *PsycEXTRA Dataset*, 1999.
18. Granacher, R. P. (2015). *Traumatic brain injury: methods for clinical & forensic neuropsychiatric assessment*. Boca Raton: CRC Press.
19. Drew, L. B., & Drew, W. E. (2004). The Contrecoup–Coup Phenomenon: A New Understanding of the Mechanism of Closed Head Injury. *Neurocritical Care*, *1*(3), 385–390. doi: 10.1385/ncc:1:3:385
20. Coup contrecoup injury. (2019, December 5). Retrieved from https://en.wikipedia.org/wiki/Coup_contrecoup_injury#/media/File:Contrecoup.svg
21. P. G. Massouros, P. V. Bayly, and G. M. Genin, Int. J. Solids Struct. 51, 305 (2014).
22. B. Giammarinaro, D. Espíndola, F. Coulouvrat, and G. Pinton, Phys. Rev. Applied 9, 014011 (2018).

23. T. M. Talavage, E. a. Nauman, E. L. Breedlove, U. Yoruk, A. E. Dye, K. E. Morigaki, H. Feuer, and L. J. Leverenz, J. Neurotrauma 31, 327 (2014).

24. J. J. Bazarian, T. Zhu, J. Zhong, D. Janigro, E. Rozen, A. Roberts, H. Javien, K. Merchant-Borna, B. Abar, and E. G. Blackman, PLoS One 9, e94734 (2014).

25. *Abbreviated injury scale*. University of Chicago: American Association for Automotive Medicine. 1985. p. 80.

26. Hodgson, V. R., & Thomas, L. M. (1972). Effect of Long-Duration Impact on Head. *SAE Technical Paper Series*. doi: 10.4271/720956

27. Mertz, H. J., Prasad, P., & Irwin, A. L. (1997). Injury Risk Curves for Children and Adults in Frontal and Rear Collisions. *SAE Technical Paper Series*. doi: 10.4271/973318

28. Beckwith, J. G., Greenwald, R. M., Chu, J. J., Crisco, J. J., Rowson, S., Duma, S. M., Collins, M. W. (2013). Head Impact Exposure Sustained by Football Players on Days of Diagnosed Concussion. *Medicine & Science in Sports & Exercise*, *45*(4), 737–746. doi: 10.1249/mss.0b013e3182792ed7

29. Mild Traumatic Brain Injury. (n.d.). *SpringerReference*. doi: 10.1007/springerreference_183073

30. Concussion in Professional Football: Reconstruction of Game Impacts and Injuries. (2004). *Neurosurgery*. doi: 10.1227/01.neu.0000440736.66757.2b

31. Funk, J. R., Duma, S. M., Manoogian, S. J., & Rowson, S. (2007). Biomechanical risk estimates for mild traumatic brain injury. *Annual proceedings. Association for the Advancement of Automotive Medicine*, *51*, 343–361.

32. Penetrating Head Trauma. (2019, November 9). Retrieved from https://emedicine.medscape.com/article/247664-overview

33. Demetriades, D. (2004). Mortality prediction of head abbreviated injury score and Glasgow Coma Scale: analysis of 7,764 head injuries1. *Journal of the American College of Surgeons*, *199*(2), 216–222. doi: 10.1016/j.jamcollsurg.2004.02.030

34. Demetriades, D., Kuncir, E., Velmahos, G. C., Rhee, P., Alo, K., & Chan, L. S. (2004). Outcome and Prognostic Factors in Head Injuries With an Admission Glasgow Coma Scale Score of 3. *Archives of Surgery*, *139*(10), 1066. doi: 10.1001/archsurg.139.10.1066

35. Santiago, L. A., Oh, B. C., Dash, P. K., Holcomb, J. B., & Wade, C. E. (2012). A clinical comparison of penetrating and blunt traumatic brain injuries. *Brain Injury*, *26*(2), 107–125. doi: 10.3109/02699052.2011.635363

36. Taber, K. H., Warden, D. L., & Hurley, R. A. (2006). Blast-Related Traumatic Brain Injury: What Is Known? *The Journal of Neuropsychiatry and Clinical Neurosciences*, *18*(2), 141–145. doi: 10.1176/jnp.2006.18.2.141

37. International Symposium on Clinical Neuroscience: Traumatic Brain Injury and Neurodegeneration Case Study Abstracts. (2015). *International Symposium on Clinical Neuroscience: Traumatic Brain Injury and Neurodegeneration Case Study Abstracts*. doi: 10.3389/978-2-88919-706-4

38. Knudsen, S. K., & Øen, E. O. (2003). Blast-induced neurotrauma in whales. *Neuroscience Research*, *46*(3), 377–386. doi: 10.1016/s0168-0102(03)00101-9

39. Kocsis, J. D., & Tessler, A. (2009). Pathology of blast-related brain injury. *The Journal of Rehabilitation Research and Development*, *46*(6), 667. doi: 10.1682/jrrd.2008.08.0100

40. Bauman, R. A., Ling, G. S., Tong, L., Januszkiewicz, A., Agoston, D., Delanerolle, N., … Parks, S. (2009). An introductory characterization of a combat-casualty-care relevant swine

model of closed head injury resulting from exposure to explosive blast. *Journal of Neurotrauma*, 090330061141047. doi: 10.1089/neu.2009-0898

41. Rezaei, A., Jazi, M. S., & Karami, G. (2013). Computational modeling of human head under blast in confined and open spaces: primary blast injury. *International Journal for Numerical Methods in Biomedical Engineering*, *30*(1), 69–82. doi: 10.1002/cnm.2590
42. Eslaminejad, A., Farid, M. H., Ziejewski, M., & Karami, G. (2018). Brain Tissue Constitutive Material Models and the Finite Element Analysis of Blast-Induced Traumatic Brain Injury. *Scientia Iranica*, *0*(0), 0–0. doi: 10.24200/sci.2018.20888
43. Rezaei, A., Jazi, M. S., Javid, S., Karami, G., & Ziejewski, M. (2014). Confined blasts, and the impact of shock wave reflections on a human head and the related traumatic brain injury. *International Journal of Experimental and Computational Biomechanics*, *2*(3), 205. doi: 10.1504/ijecb.2014.060398
44. Richter, M., Otte, D., Lehmann, U., Chinn, B., Schuller, E., Doyle, D., … Krettek, C. (2001). Head Injury Mechanisms in Helmet-Protected Motorcyclists: Prospective Multicenter Study. *The Journal of Trauma: Injury, Infection, and Critical Care*, *51*(5), 949–958. doi: 10.1097/00005373-200111000-00021
45. Kleiven, S. (2007). Predictors for Traumatic Brain Injuries Evaluated through Accident Reconstructions. *SAE Technical Paper Series*. doi: 10.4271/2007-22-0003
46. Holbourn, A. (1943). Mechanics Of Head Injuries. *The Lancet*, *242*(6267), 438–441. doi: 10.1016/s0140-6736(00)87453-x
47. Mcelhaney, J. (1982). Biomechanics. Mechanical Properties of Living Tissues by Y. C. Fung. *Medical Physics*, *9*(5), 788–789. doi: 10.1118/1.595186

48. Farid, M. H., Ramzanpour, M., Eslaminejad, A., Ziejewski, M., & Karami, G. (2018). Computational Simulation of Brain Inury By Golf Ball Impacts in Adult and Children. *brain*, *13*, 16.

49. Zhang, L., Yang, K. H., & King, A. I. (2001). Comparison of brain responses between frontal and lateral impacts by finite element modeling. *Journal of neurotrauma*, *18*(1), 21-30.

50. Zhang, J., Yoganandan, N., Pintar, F. A., & Gennarelli, T. A. (2006). Role of translational and rotational accelerations on brain strain in lateral head impact. *Biomed Sci Instrum*, *42*, 501-506.

51. Chu, Y. H., & Bottlang, M. (2002). Finite element analysis of traumatic brain injury. *Legacy Clinical Research and Technology Center, Portland, OR*.

52. Adams, J. H., Doyle, D., Ford, I., Gennarelli, T. A., Graham, D. I., & McLellan, D. R. (1989). Diffuse axonal injury in head injury: definition, diagnosis and grading. *Histopathology*, *15*(1), 49-59.

53. (n.d.). *Forbes*, Forbes Magazine, <https://www.forbes.com/video/4739576867001/#5d22338057b4> (Dec. 5, 2018).

54. Espn, D. R. V. (2018). "NFL television ratings down 9.7 percent during 2017 regular season." *ABC News*, ABC News Network, <https://abcnews.go.com/Sports/nfl-television-ratings-97-percent-2017-regular-season/story?id=52143709> (Dec. 5, 2018).

55. Underwood, E. (2013). "NFL Kicks Off Brain Injury Research Effort." *Science*, 339(6126), 1367–1367.

56. Heger, I. M., & Subhash, G. (2012). *U.S. Patent Application No. 13/357,175*.

57. Baugh, C. M., Stamm, J. M., Riley, D. O., Gavett, B. E., Shenton, M. E., Lin, A., ... & Stern, R. A. (2012). Chronic traumatic encephalopathy: neurodegeneration following repetitive concussive and subconcussive brain trauma. *Brain imaging and behavior*, *6*(2), 244-254.

58. Wittmann, C. W., Wszolek, M. F., Shulman, J. M., Salvaterra, P. M., Lewis, J., Hutton, M., & Feany, M. B. (2001). Tauopathy in Drosophila: neurodegeneration without neurofibrillary tangles. *Science*, *293*(5530), 711-714.

59. Stern, R. A., Riley, D. O., Daneshvar, D. H., Nowinski, C. J., Cantu, R. C., & McKee, A. C. (2011). Long-term consequences of repetitive brain trauma: chronic traumatic encephalopathy. *Pm&r*, *3*(10), S460-S467.

60. McKee, A. C., Gavett, B. E., Stern, R. A., Nowinski, C. J., Cantu, R. C., Kowall, N. W., ... & Morin, P. (2010). TDP-43 proteinopathy and motor neuron disease in chronic traumatic encephalopathy. *Journal of Neuropathology & Experimental Neurology*, *69*(9), 918-929.

61. Omalu, B. I., Hamilton, R. L., Kamboh, I. M., Dekosky, S. T., and Bailes, J. (2010). "Chronic traumatic encephalopathy (CTE) in a National Football League Player." *Journal of Forensic Nursing*, 6(1), 40–46.

62. Omalu, B. I., Hamilton, R. L., Kamboh, M. I., DeKosky, S. T., & Bailes, J. (2010). Chronic traumatic encephalopathy (CTE) in a National Football League Player: Case report and emerging medicolegal practice questions. *Journal of forensic nursing*, *6*(1), 40-46.

63. Omalu, B. I., Bailes, J., Hammers, J. L., & Fitzsimmons, R. P. (2010). Chronic traumatic encephalopathy, suicides and parasuicides in professional American athletes: the role of the forensic pathologist. *The American journal of forensic medicine and pathology*, *31*(2), 130-132.

64. Goldstein, L. E., Fisher, A. M., Tagge, C. A., Zhang, X. L., Velisek, L., Sullivan, J. A., ... & Goletiani, C. J. (2012). Chronic traumatic encephalopathy in blast-exposed military veterans and a blast neurotrauma mouse model. *Science translational medicine*, *4*(134), 134ra60-134ra60.

65. Miller, K., & Chinzei, K. (2002). Mechanical properties of brain tissue in tension. *Journal of biomechanics*, *35*(4), 483-490.

66. Chafi, M. S., Karami, G., & Ziejewski, M. (2010). Biomechanical assessment of brain dynamic responses due to blast pressure waves. *Annals of biomedical engineering*, *38*(2), 490-504.

67. Chafi, M. S., Ganpule, S., Gu, L., & Chandra, N. (2011). Dynamic response of brain subjected to blast loadings: influence of frequency ranges. *International Journal of Applied Mechanics*, *3*(04), 803-823.

68. Farid, M. H. (2019). *Mechanical characterization and constitutive modeling of rate-dependent viscoelastic brain tissue under high rate loadings* (Doctoral dissertation, North Dakota State University).

69. Schwarz, B. J., & Richardson, M. H. (1999). Experimental Modal Analysis. *Vibration*.

70. Schmid, P. J. (2010). Dynamic mode decomposition of numerical and experimental data. *Journal of Fluid Mechanics*, *656*, 5–28.

71. Berkooz, G., Holmes, P., & Lumley, J. L. (1993). The proper orthogonal decomposition in the analysis of turbulent flows. *Annual review of fluid mechanics*, *25*(1), 539-575.

72. Mann, J., & Kutz, J. N. (2016). Dynamic mode decomposition for financial trading strategies. *Quantitative Finance*, *16*(11), 1643–1655.

73. Schmid, P. J., Li, L., Juniper, M. P., & Pust, O. (2011). Applications of the dynamic mode decomposition. *Theoretical and Computational Fluid Dynamics*, *25*(1-4), 249-259.

74. Laksari, K., Kurt, M., Babaee, H., Kleiven, S., & Camarillo, D. (2018). Mechanistic insights into human brain impact dynamics through modal analysis. *Physical review letters*, *120*(13), 138101.

75. Horgan, T. J., & Gilchrist, M. D. (2003). The creation of three-dimensional finite element models for simulating head impact biomechanics. *International Journal of Crashworthiness*, *8*(4), 353-366.

76. Nahum, A. M., Smith, R., & Ward, C. C. (1977). *Intracranial pressure dynamics during head impact* (No. 770922). SAE Technical Paper.

77. Mendis, K. K., Stalnaker, R. L., & Advani, S. H. (1995). A constitutive relationship for large deformation finite element modeling of brain tissue.

APPENDIX A. SUPPLEMENTAL TABLES AND FIGURES

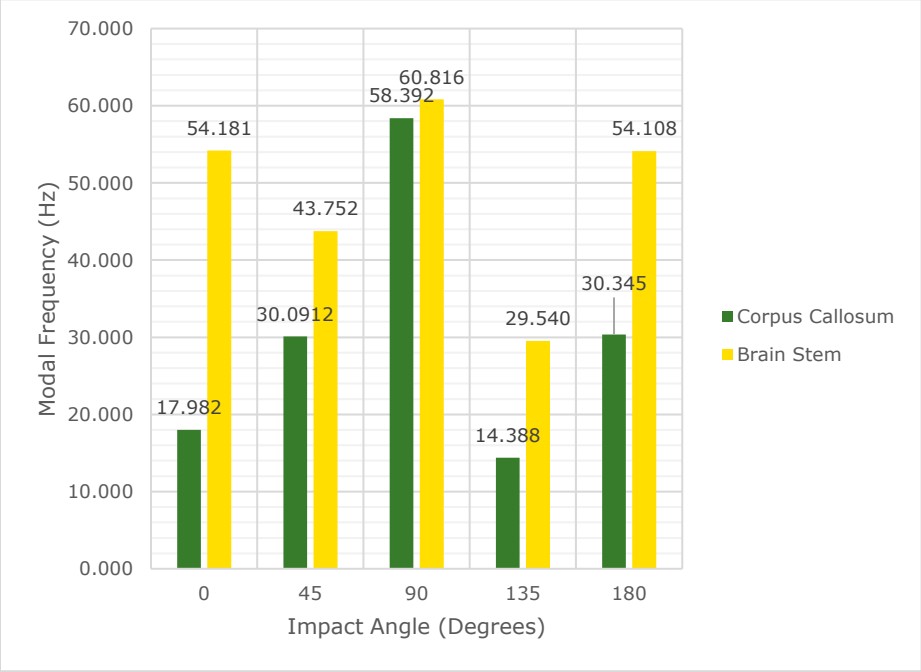

Figure A-1: Comparison of Mode 1 modal frequencies for each impact angle using displacement in the coronal direction of nodes near the corpus callosum and brain stem.

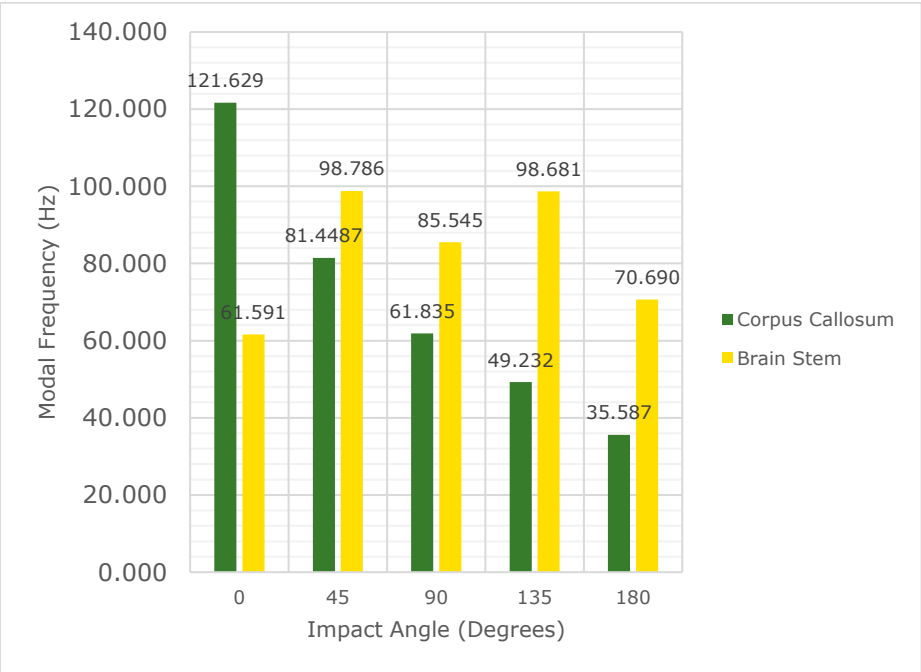

Figure A-2: Comparison of Mode 2 modal frequencies for each impact angle using displacement in the coronal direction of nodes near the corpus callosum and brain stem.

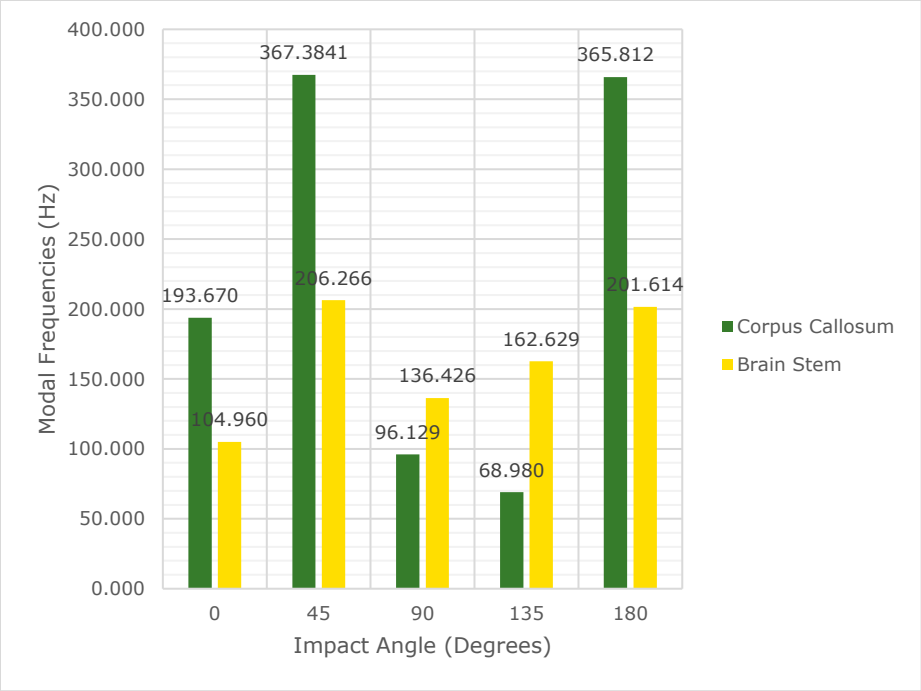

Figure A-3: Comparison of Mode 3 modal frequencies for each impact angle using displacement in the coronal direction of nodes near the corpus callosum and brain stem.

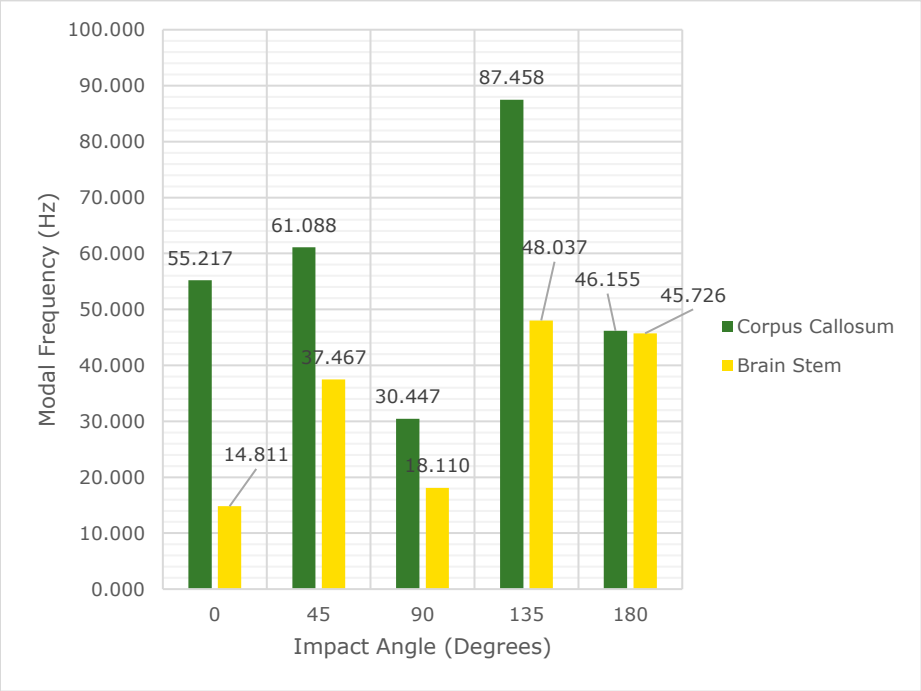

Figure A-4: Comparison of Mode 1 modal frequencies for each impact angle using displacement in the sagittal direction of nodes near the corpus callosum and brain stem.

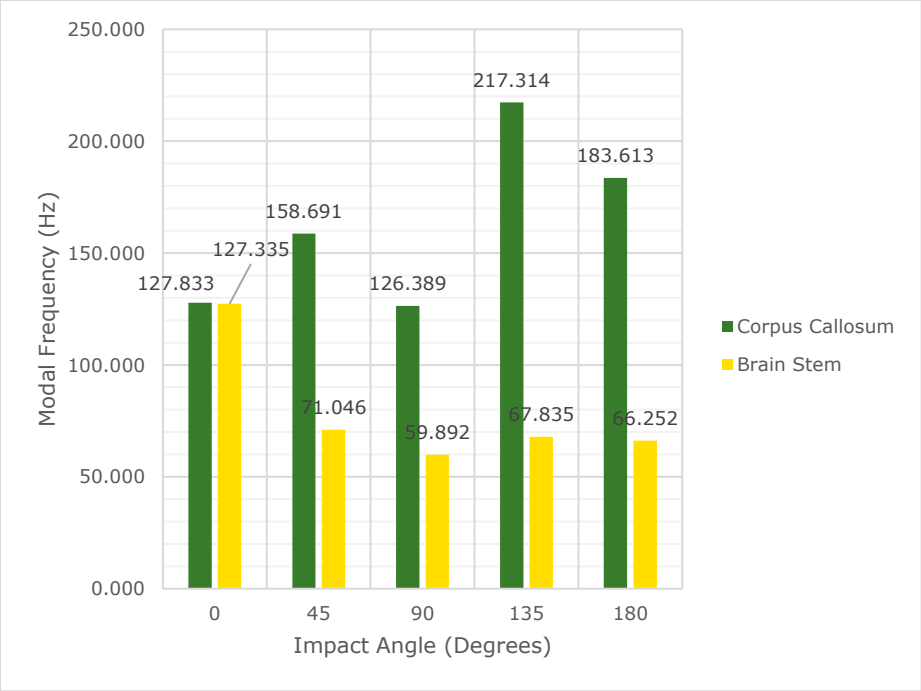

Figure A-5: Comparison of Mode 2 modal frequencies for each impact angle using displacement in the sagittal direction of nodes near the corpus callosum and brain stem.

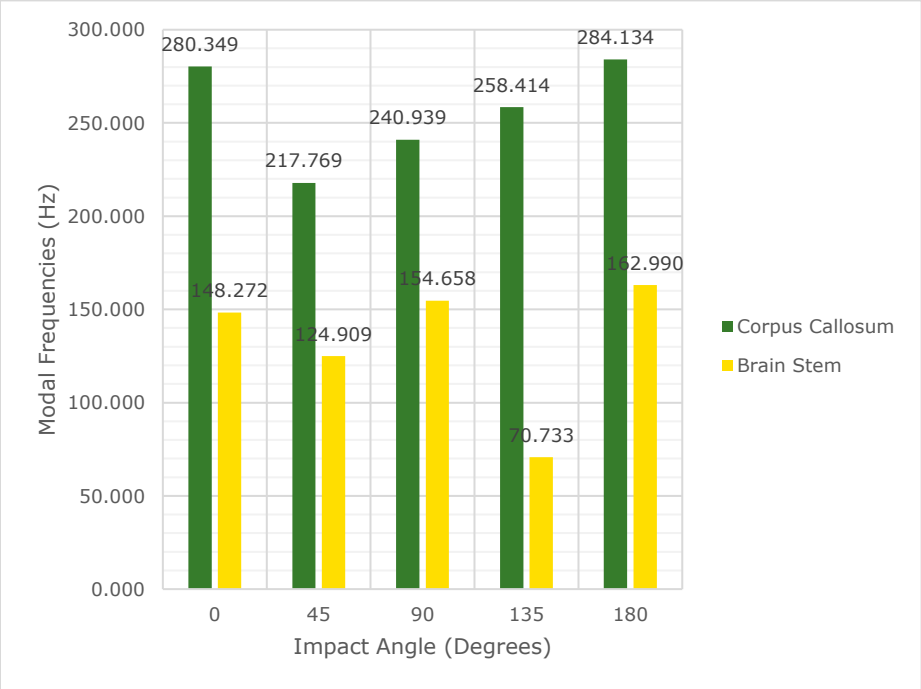

Figure A-6: Comparison of Mode 3 modal frequencies for each impact angle using displacement in the sagittal direction of nodes near the corpus callosum and brain stem.

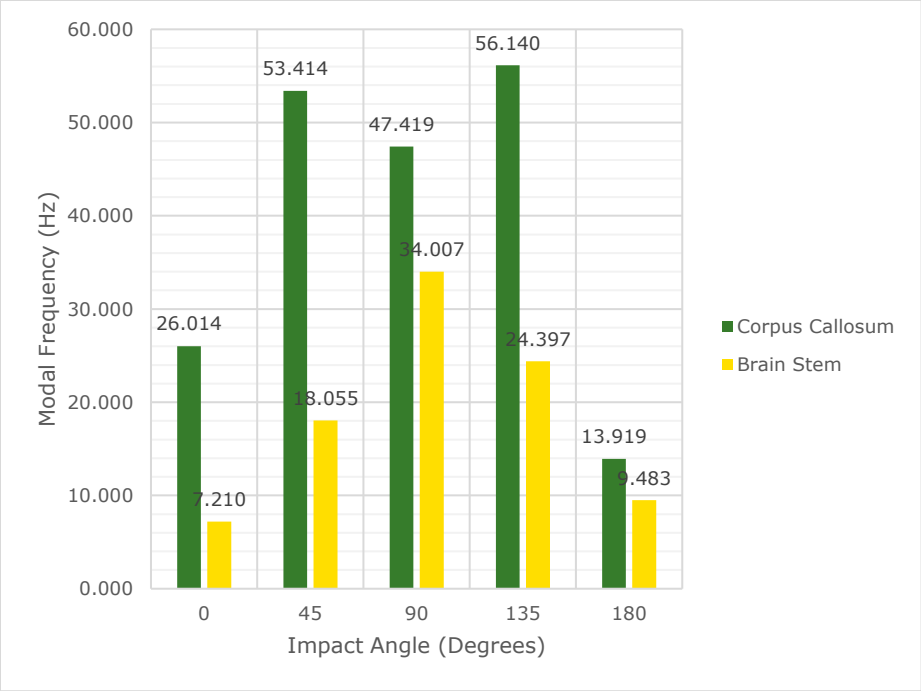

Figure A-7: Comparison of Mode 1 modal frequencies for each impact angle using displacement in the axial direction of nodes near the corpus callosum and brain stem.

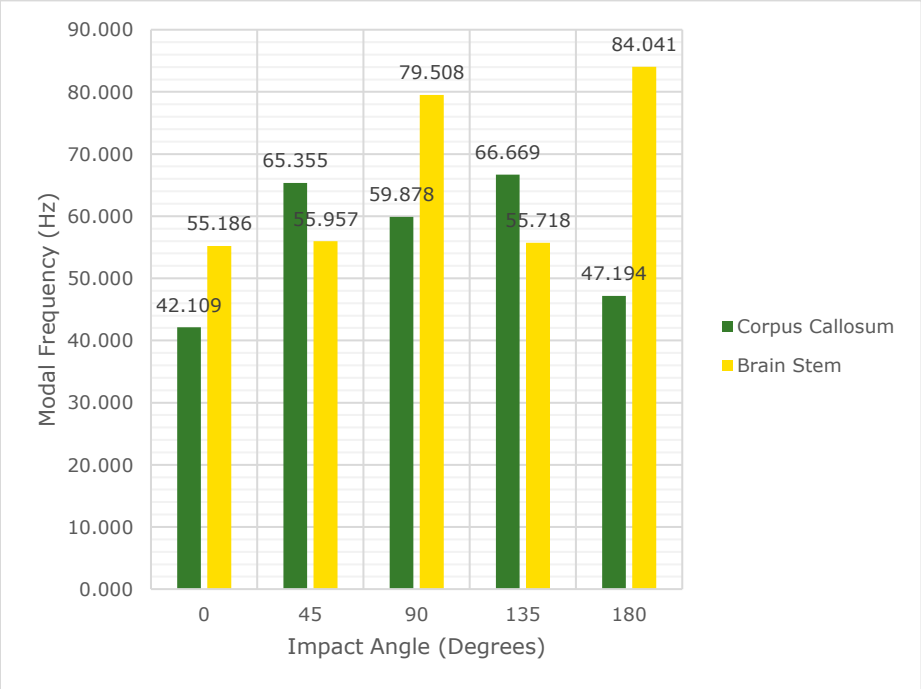

Figure A-8: Comparison of Mode 2 modal frequencies for each impact angle using displacement in the axial direction of nodes near the corpus callosum and brain stem.

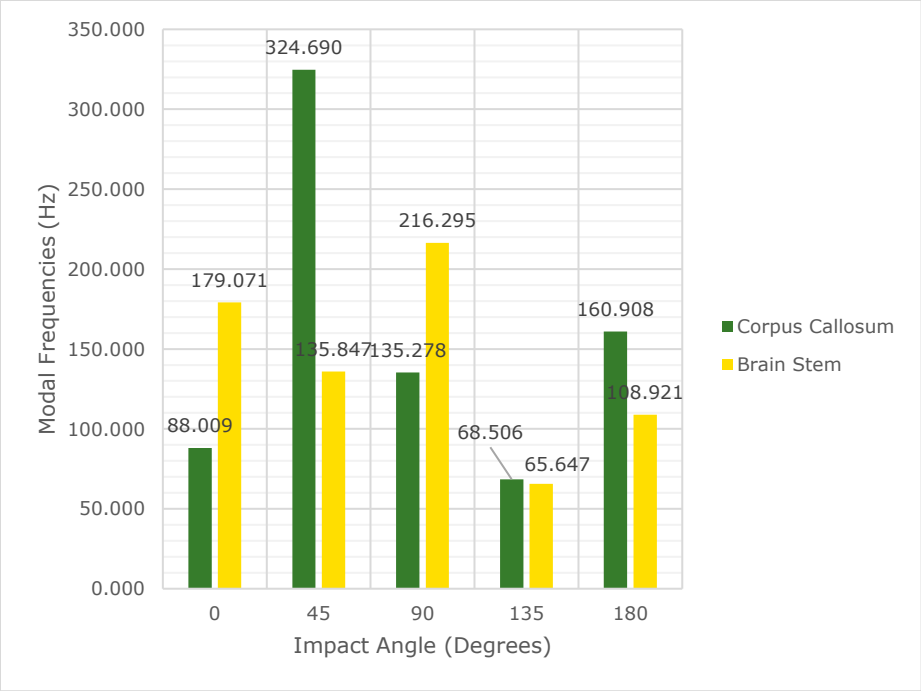

Figure A-9: Comparison of Mode 3 modal frequencies for each impact angle using displacement in the axial direction of nodes near the corpus callosum and brain stem.

Table A-1: Modal frequency, amplitude, and decay rates using coronal displacement for nodes near the corpus callosum and 0° impact angle.

Modal Frequency (Hz)	Normalized Modal Amplitude	Decay Rate (Hz)
17.982	0.765	145.742
121.629	0.999	1291.066
193.670	1.000	911.351

Table A-2: Modal frequency, amplitude, and decay rates using coronal displacement for nodes near the corpus callosum and 45° impact angle.

Modal Frequency (Hz)	Normalized Modal Amplitude	Decay Rate (Hz)
30.0912	0.8602	269.3574
81.4487	1.0000	1516.8221
367.3841	0.9880	849.9997

Table A-3: Modal frequency, amplitude, and decay rates using coronal displacement for nodes near the corpus callosum and 90° impact angle.

Modal Frequency (Hz)	Normalized Modal Amplitude	Decay Rate (Hz)
58.392	0.920	173.097
61.835	0.965	997.583
96.129	1.000	504.293

Table A-4: Modal frequency, amplitude, and decay rates using coronal displacement for nodes near the corpus callosum and 135° impact angle.

Modal Frequency (Hz)	Normalized Modal Amplitude	Decay Rate (Hz)
14.388	0.906	140.037
49.232	1.000	1543.304
68.980	0.981	773.187

Table A-5: Modal frequency, amplitude, and decay rates using coronal displacement for nodes near the corpus callosum and 180° impact angle.

Modal Frequency (Hz)	Normalized Modal Amplitude	Decay Rate (Hz)
30.345	0.920	129.850
35.587	1.000	1012.474
365.812	0.973	2737.230

Table A-6: Modal frequency, amplitude, and decay rates using sagittal displacement for nodes near the corpus callosum and 0° impact angle.

Modal Frequency (Hz)	Normalized Modal Amplitude	Decay Rate (Hz)
55.217	1.000	109.530
127.833	0.995	1278.949
280.349	0.960	3214.399

Table A-7: Modal frequency, amplitude, and decay rates using sagittal displacement for nodes near the corpus callosum and 45° impact angle.

Modal Frequency (Hz)	Normalized Modal Amplitude	Decay Rate (Hz)
61.088	1.000	67.097
158.691	0.996	779.565
217.769	0.872	4908.364

Table A-8: Modal frequency, amplitude, and decay rates using sagittal displacement for nodes near the corpus callosum and 90° impact angle.

Modal Frequency (Hz)	Normalized Modal Amplitude	Decay Rate (Hz)
30.447	1.000	179.928
126.389	0.996	1354.003
240.939	0.987	192.054

Table A-9: Modal frequency, amplitude, and decay rates using sagittal displacement for nodes near the corpus callosum and 135° impact angle.

Modal Frequency (Hz)	Normalized Modal Amplitude	Decay Rate (Hz)
87.458	1.000	500.127
217.314	0.994	0.000
258.414	0.940	2450.597

Table A-10: Modal frequency, amplitude, and decay rates using sagittal displacement for nodes near the corpus callosum and 180° impact angle.

Modal Frequency (Hz)	Normalized Modal Amplitude	Decay Rate (Hz)
46.155	1.000	0.000
183.613	0.983	744.021
284.134	0.884	3033.008

Table A-11: Modal frequency, amplitude, and decay rates using axial displacement for nodes near the corpus callosum and 0° impact angle.

Modal Frequency (Hz)	Normalized Modal Amplitude	Decay Rate (Hz)
26.014	1.000	0.000
42.109	0.892	1064.021
88.009	0.992	463.271

Table A-12: Modal frequency, amplitude, and decay rates using axial displacement for nodes near the corpus callosum and 45° impact angle.

Modal Frequency (Hz)	Normalized Modal Amplitude	Decay Rate (Hz)
53.414	0.961	323.693
65.355	1.000	783.084
324.690	0.971	2143.514

Table A-13: Modal frequency, amplitude, and decay rates using axial displacement for nodes near the corpus callosum and 90° impact angle.

Modal Frequency (Hz)	Normalized Modal Amplitude	Decay Rate (Hz)
47.419	1.000	804.715
59.878	0.981	139.979
135.278	0.986	2264.666

Table A-14: Modal frequency, amplitude, and decay rates using axial displacement for nodes near the corpus callosum and 135° impact angle.

Modal Frequency (Hz)	Normalized Modal Amplitude	Decay Rate (Hz)
56.140	0.976	1250.792
66.669	1.000	0.000
68.506	0.998	965.212

Table A-15: Modal frequency, amplitude, and decay rates using axial displacement for nodes near the corpus callosum and 180° impact angle.

Modal Frequency (Hz)	Normalized Modal Amplitude	Decay Rate (Hz)
13.919	1.000	700.097
47.194	1.000	1562.874
160.908	0.947	2449.779

Table A-16: Modal frequency, amplitude, and decay rates using total displacement for nodes near the brain stem and 0° impact angle.

Modal Frequency (Hz)	Normalized Modal Amplitude	Decay Rate (Hz)
58.867	1.000	0.000
64.641	0.978	454.714
72.076	0.974	1352.444

Table A-17: Modal frequency, amplitude, and decay rates using total displacement for nodes near the brain stem and 45° impact angle.

Modal Frequency (Hz)	Normalized Modal Amplitude	Decay Rate (Hz)
24.119	0.988	73.410
63.430	1.000	0.000
118.182	0.985	976.360

Table A-18: Modal frequency, amplitude, and decay rates using total displacement for nodes near the brain stem and 90° impact angle.

Modal Frequency (Hz)	Normalized Modal Amplitude	Decay Rate (Hz)
32.372	0.869	333.298
41.363	0.976	1084.949
154.826	1.000	0.000

Table A-19: Modal frequency, amplitude, and decay rates using total displacement for nodes near the brain stem and 135° impact angle.

Modal Frequency (Hz)	Normalized Modal Amplitude	Decay Rate (Hz)
41.239	0.902	398.592
54.440	0.986	937.019
75.734	1.000	0.000

Table A-20: Modal frequency, amplitude, and decay rates using total displacement for nodes near the brain stem and 180° impact angle.

Modal Frequency (Hz)	Normalized Modal Amplitude	Decay Rate (Hz)
66.765	0.993	85.471
117.047	0.988	356.147
151.385	1.000	794.293

Table A-21: Modal frequency, amplitude, and decay rates using coronal displacement for nodes near the brain stem and 0° impact angle.

Modal Frequency (Hz)	Normalized Modal Amplitude	Decay Rate (Hz)
54.181	1.000	344.270
61.591	0.953	192.273
104.960	0.975	1646.840

Table A-22: Modal frequency, amplitude, and decay rates using coronal displacement for nodes near the brain stem and 45° impact angle.

Modal Frequency (Hz)	Normalized Modal Amplitude	Decay Rate (Hz)
43.752	0.938	506.754
98.786	0.946	196.418
206.266	1.000	0.000

Table A-23: Modal frequency, amplitude, and decay rates using coronal displacement for nodes near the brain stem and 90° impact angle.

Modal Frequency (Hz)	Normalized Modal Amplitude	Decay Rate (Hz)
60.816	0.919	1168.677
85.545	0.861	326.059
136.426	1.000	0.000

Table A-24: Modal frequency, amplitude, and decay rates using coronal displacement for nodes near the brain stem and 135° impact angle.

Modal Frequency (Hz)	Normalized Modal Amplitude	Decay Rate (Hz)
29.540	0.917	349.836
98.681	0.978	1983.104
162.629	1.000	98.607

Table A-25: Modal frequency, amplitude, and decay rates using coronal displacement for nodes near the brain stem and 180° impact angle.

Modal Frequency (Hz)	Normalized Modal Amplitude	Decay Rate (Hz)
54.108	0.984	522.827
70.690	0.981	938.821
201.614	1.000	0.000

Table A-26: Modal frequency, amplitude, and decay rates using sagittal displacement for nodes near the brain stem and 0° impact angle.

Modal Frequency (Hz)	Normalized Modal Amplitude	Decay Rate (Hz)
14.811	0.998	360.885
127.335	0.956	1332.323
148.272	1.000	0.000

Table A-27: Modal frequency, amplitude, and decay rates using sagittal displacement for nodes near the brain stem and 45° impact angle.

Modal Frequency (Hz)	Normalized Modal Amplitude	Decay Rate (Hz)
37.467	0.975	347.998
71.046	0.978	1129.352
124.909	1.000	0.000

Table A-28: Modal frequency, amplitude, and decay rates using sagittal displacement for nodes near the brain stem and 90° impact angle.

Modal Frequency (Hz)	Normalized Modal Amplitude	Decay Rate (Hz)
18.110	0.791	951.042
59.892	0.894	348.278
154.658	1.000	0.000

Table A-29: Modal frequency, amplitude, and decay rates using sagittal displacement for nodes near the brain stem and 135° impact angle.

Modal Frequency (Hz)	Normalized Modal Amplitude	Decay Rate (Hz)
48.037	1.000	154.454
67.835	0.993	453.381
70.733	0.951	825.030

Table A-30: Modal frequency, amplitude, and decay rates using sagittal displacement for nodes near the brain stem and 180° impact angle.

Modal Frequency (Hz)	Normalized Modal Amplitude	Decay Rate (Hz)
45.726	0.996	1049.190
66.252	0.897	362.843
162.990	1.000	0.000

Table A-31: Modal frequency, amplitude, and decay rates using axial displacement for nodes near the brain stem and 0° impact angle.

Modal Frequency (Hz)	Normalized Modal Amplitude	Decay Rate (Hz)
7.210	1.000	0.000
55.186	0.797	375.794
179.071	0.942	1234.051

Table A-32: Modal frequency, amplitude, and decay rates using axial displacement for nodes near the brain stem and 45° impact angle.

Modal Frequency (Hz)	Normalized Modal Amplitude	Decay Rate (Hz)
18.055	1.000	21.271
55.957	0.902	230.956
135.847	0.943	1509.765

Table A-33: Modal frequency, amplitude, and decay rates using axial displacement for nodes near the brain stem and 90° impact angle.

Modal Frequency (Hz)	Normalized Modal Amplitude	Decay Rate (Hz)
34.007	0.998	1055.904
79.508	0.964	293.267
216.295	1.000	0.000

Table A-34: Modal frequency, amplitude, and decay rates using axial displacement for nodes near the brain stem and 135° impact angle.

Modal Frequency (Hz)	Normalized Modal Amplitude	Decay Rate (Hz)
24.397	1.000	1160.137
55.718	0.903	152.254
65.647	0.944	395.725

Table A-35: Modal frequency, amplitude, and decay rates using axial displacement for nodes near the brain stem and 180° impact angle.

Modal Frequency (Hz)	Normalized Modal Amplitude	Decay Rate (Hz)
9.483	0.917	393.497
84.041	0.975	1339.356
108.921	1.000	2177.830

APPENDIX B. DMD CODE

```
clc; clear all; close all;
A1=readtable('180deg_z_occ.csv');
A=table2array(A1);
dt=50*(10^-6);
[m,n]=size(A);
x=A(:,1);
A=A(:,2:n-1);
A=A';
plot(x,A(:,:))
xlabel('Time (us)');
ylabel('Displacement (cm)')
n1=n-2;
X1=A(:,1:end-1);
X2=A(:,2:end);
[U,S,V]=svd(X1,'econ');
figure
r=6;
U=U(:,1:r);
S=S(1:r,1:r);
V=V(:,1:r);
plot(diag(S)/sum(diag(S)))
xlabel('Mode Number');
ylabel('Variance');
St=U'*X2*V/S;
[W,eigs]=eig(St);
P=X2*V/S*W;
Pr=real(P);
x1=linspace(0,15,n1);
i=1;
lambda=diag(eigs);
w=log(lambda)/(dt);
for m=1:2:r
PM(i)=norm(Pr(:,m));
```

```
wM(i)=abs(real(w(m)));
wM2(i)=abs(imag(w(m)));
sigma(i)=std(Pr(:,m));
i=i+1;
end
PT=PM'/max(PM);
Matrix=[wM' PT sigma' wM2'];
Matrix(:,1);
r1=X2(1:r,1:r)-St*X1(1:r,1:r);
norm2=norm(r1);
w
```